Simulations of
Dwarf Galaxy Formation

Till Sawala

München 2011

Simulations of
Dwarf Galaxy Formation

Till Sawala

Dissertation
an der Fakultät für Physik
der Ludwig–Maximilians–Universität
München

vorgelegt von
Till Sawala
aus Nantes (F)

München, den 7.1.2011

There are no passengers on Spaceship Earth.
We are all crew.

Marshall McLuhan

Für meine Eltern

Outline

This thesis is organised in six chapters. A short summary of the motivation for studying dwarf galaxies is given at the beginning of Chapter 1, followed by a review of the cosmological framework, and the astrophysical processes relevant to galaxy formation. An analytical description of structure formation, and the current observational status on dwarf galaxies is also presented. The numerical methods used in this work are described in Chapter 2, with a particular emphasis on the generation of initial conditions.

The main body of work is presented in Chapters 3 to 6, which are largely self-contained, focusing on different aspects of dwarf galaxy formation. Chapter 3 presents results of numerical high-resolution simulations of dwarf-spheroidal type galaxies in isolation, while Chapter 4 focuses on the evolution of dwarf galaxies in different environments, and on the satellite galaxies of the Milky Way. In Chapter 5, the formation of isolated dwarf-irregular type galaxies is investigated in a sample of haloes extracted from the Millennium-II simulation, and the predictions of hydrodynamical simulations are compared to results from abundance matching arguments. Chapter 6 gives an outlook to ongoing work that extends this analysis, with a direct comparison between hydrodynamical simulations and semi-analytical models for dwarf galaxies. Chapters 3 and 5 are closely based on two published papers, on "Formation of Isolated Dwarf Galaxies with Feedback" (Sawala et al., 2010), and "What is the (Dark) Matter with Dwarf Galaxies?" (Sawala et al., 2010). A paper summarising the results of Chapter 4 is currently in preparation.

Contents

Summary

Dwarf galaxies are related to important cosmological questions, and central to our understanding of the physics of galaxy formation. In this thesis, I present the results of cosmological, hydrodynamical simulations of the formation and evolution of dwarf galaxies. I compare the simulation results with observations, and interpret them in the context of a ΛCDM cosmology.

In high resolution simulations of isolated dwarf galaxies, I show that a combination of supernova feedback and the cosmic UV background results in the formation of galaxies with properties similar to the Local Group dwarf spheroidals, and that both effects are strongly moderated by the depth of the gravitational potential. The simulations naturally reproduce the observed scaling relations between luminosity and mass-to-light ratio, and between total stellar mass and metallicities. The final objects have halo masses between 2.3×10^8 and 1.1×10^9 $M_\odot$, mean velocity dispersions between 6.5 and 9.7 kms^{-1}, stellar masses ranging from 5×10^5 to $1.2 \times 10^7 M_\odot$, median metallicities between $[\mathrm{Fe/H}] = -1.8$ and -1.1, and half-light radii of the order of 200 to 300 pc, all comparable with Local Group dwarf spheroidals. The simulations also indicate that the dwarf spheroidal galaxies observed today lie near a mass threshold around 10^9 $M_\odot$, in agreement with stellar kinematic data, where supernova feedback not only suffices to completely expel the interstellar medium and leave the residual gas-free, but where the combination of feedback, UV radiation and self-shielding establishes a dichotomy of age distributions similar to that observed in the Milky Way and M31 satellites.

A second line of work has been the analysis of the dwarf galaxy population resulting from the *Aquila* simulation. By simultaneously including the formation of a Milky Way type galaxy along with ~ 500 dwarf-sized haloes in the mass range of $\sim 10^8 - 10^{10} M_\odot$, this simulation allows a study of the effect of the environment on dwarf galaxy evolution. I study the relative importance, and interplay, of the different mechanisms for gas loss, and compare the properties of the satellites with those of isolated dwarf galaxies.

A third set of simulations focuses on the formation of dwarf galaxies in a representative sample of haloes extracted from the *Millennium-II* simulation. The six haloes in these simulations all have a $z = 0$ mass of $\sim 10^{10} M_\odot$ and show different mass assembly histories, which are reflected in different star formation histories. The galaxies reach final stellar masses in the range of $5 \times 10^7 - 10^8 M_\odot$, consistent with other published simulations of galaxy formation in similar mass haloes. The resulting objects have structures and stellar populations consistent with dwarf elliptical and dwarf irregular galaxies. However, in a ΛCDM universe, $10^{10} M_\odot$ haloes must typically contain galaxies with much lower stellar mass than these simulations predict, if they are to match observed galaxy abundances. The dwarf galaxies formed in my own and all other current hydrodynamical simulations are

more than an order of magnitude more luminous than expected for haloes of this mass. I discuss the significance and possible implications of this result for cosmological models, and for the assumptions about the physics of galaxy formation.

Finally, I present preliminary results of a direct comparison between hydrodynamical simulations and semi-analytical models for the formation of dwarf galaxies. Current semi-analytical models, which are tuned to match the statistical properties of galaxies, do not agree with the predictions of hydrodynamical simulations for individual objects. Conversely, when tuned to accurately reproduce the simulations, semi-analytical models can give a more qualitative interpretation of the simulation results, in terms of equations of galaxy formation. The combination of the two methods allows an extrapolation from individual cases to cosmological volumes, not currently attainable with direct simulations alone.

Zusammenfassung

Zwerggalaxien sind mit wichtigen kosmologischen Fragen verbunden, und entscheidend für unser Vertändnis der Physik der Galaxienentstehung. In der vorgelegten Arbeit präsentiere ich Ergebnisse kosmologischer, hydrodynamischer Simulationen der Entstehung und Entwicklung von Zwerggalaxien. Ich vergleiche die Ergebnisse der Simulationen mit Beobachtungen, und interpretiere sie im Kontext des ΛCDM-Modells.

In hochaufgelösten Simulationen einzelner Zwerggalaxien zeige ich, dass eine Kombination aus Supernova-Winden und der kosmischen UV-Strahlung zur Entstehung von Galaxien führt, die in vielerlei Hinsicht mit den Zwerggalaxien der Lokalen Gruppe übereinstimmen. Zudem zeige ich, dass beide Effekte stark vom Gravitationspotential der entstehenden Galaxie abhängen. Auf diese Weise lassen sich die beobachteten Korrelationen zwischen Helligkeit und dem Verhältnis aus Helligkeit und Gesamtmasse, sowie zwischen der stellaren Masse und der stellaren Metallizität reproduzieren und erklären. Die resultierenden Objekte besitzen Gesamtmassen zwischen $2,3 \times 10^8$ und $1,1 \times 10^9 M_\odot$, mittlere Geschwindigkeitsdispersionen zwischen 6,5 und 9,7 kms^{-1}, stellare Massen im Bereich von 5×10^5 bis $1,2 \times 10^7 M_\odot$, mittlere Metallizitäten zwischen [Fe/H] $= -1,8$ und $-1,1$, sowie Halblicht-Radien von ca $200-300$pc. Alle diese Werte sind vergleichbar mit denen beobachteter *Dwarf Spheroidal*-Galaxien der Lokalen Gruppe. Die Simulationen sagen ferner voraus, dass die Halos heutiger *Dwarf Spheroidal*-Galaxien in der Nähe eines Schwellenwertes der Gesamtmasse von etwa $\sim 10^9 M_\odot$ liegen, in Übereinstimmung mit beobachteten Geschwindigkeitsdispersionen. Unterhalb dieser charakteristischen Masse sind Supernova-Explosionen nicht nur ausreichend, das interstellare Gas nahezu vollständig zu entfernen; eine Kombination aus Supernova-Explosionen, UV-Strahlung und der Selbst-Abschirmung ruft auch eine Dichotomie in der Altersverteilung hervor, die den Beobachtungen der Satelliten-Galaxien der Milchstraße und M31 entspricht.

Ein zweiter Teil der Arbeit besteht aus der Analyse der Zwerggalaxien in der *Aquila*-Simulation. Indem diese gleichzeitig die Entstehung einer Milchstraße-artigen Galaxie, sowie etwa 500 Zwerg-Halos im Bereich von $\sim 10^8 - 10^{10} M_\odot$ beinhaltet, erlaubt sie es, die Entwicklung von Zwerggalaxien in Abhängigkeit von ihrer Umgebung zu betrachten. Ich untersuche die relative Bedeutung und das Zusammenspiel verschiedener Mechanismen des Gasverlustes, und vergleiche die Eigenschaften der Satelliten-Galaxien mit denen isolierter Zwerggalaxien.

Eine dritte Reihe von Simulationen befasst sich mit der Entstehung von Zwerggalaxien in einer repräsentativen Auswahl von Halos, die aus der *Millennium-II*-Simulation extrahiert wurden. Alle sechs Halos in diesen Simulationen erreichen eine Gesamtmasse von $\sim 10^{10} M_\odot$. Sie unterscheiden sich jedoch in ihrer zeitlichen Entwicklung, was sich in der Sternentstehungsgeschichte widerspiegelt. Die sechs

Galaxien erreichen Sternenmassen zwischen $5 \times 10^7 - 10^8 \mathrm{M}_\odot$, in Übereinstimmung mit anderen publizierten Simulationen in Halos gleicher Masse. Die entstandenen Objekte weisen Strukturen und Sternenpopulationen auf, die mit elliptischen und irregulären Zwerggalaxien übereinstimmen. Allerdings müssen Halos dieser Masse in einem ΛCDM-Universum Galaxien mit sehr viel geringerer Sternenmasse beherbergen, um die beobachtete Anzahl von Galaxien zu erklären. Die Zwerggalaxien in diesen Simulationen, sowie in allen anderen gegenwärtigen hydrodynamischen Modellen, übertreffen die ihrer Halo-Masse entsprechende Leuchtstärke um mehr als eine Größenordnung. Ich diskutiere die Bedeutung und mögliche Auswirkungen dieses Ergebnisses auf kosmologische Modelle, sowie auf die Annahmen über die Physik der Galaxienentstehung.

Der letzte Abschnitt stellt vorläufige Ergebnisse eines direkten Vergleichs hydrodynamischer Simulationen und semi-analytischer Modelle vor. Derzeitige semi-analytische Modelle, die darauf abgestimmt sind, statistische Größen der Galaxienverteilung zu beschreiben, stimmen nicht mit den Vorhersagen hydrodynamischer Simulationen für einzelne Objekte überein. Andererseits erlauben es semi-analytische Modelle, die in Übereinstimmung mit den Simulationen gebracht wurden, die Vorhersagen direkter Simulationen in Gleichungen der Galaxienentwicklung zu übersetzen, und so ein qualitatives Verständnis der relevanten Mechanismen zu gewinnen. Eine Kombination beider Methoden ermöglicht eine Extrapolation von einzelnen Objekten auf kosmologische Volumen, und damit Aussagen zu treffen, die heute mit direkten Simulationen nicht erreichbar sind.

1 Chapter 1
Introduction

1.1 Motivation

Dwarf galaxies are the most abundant galaxies in the universe. With stellar masses ranging from $\sim 10^2$ to $10^9 \mathrm{M}_\odot$, they span a wider range in magnitudes than all other classes of galaxies combined. Observations further reveal a rich variety of properties, indicating a corresponding diversity of formation scenarios. For these reasons alone, dwarf galaxies are very well worth of our attention. But dwarf galaxies are also connected to a number of important current questions in astrophysics and cosmology, which makes them even more interesting to study:

- Living in the lowest mass haloes, dwarf galaxies are important probes for the limits of cosmic structure formation. In the hierarchical framework, they trace the first bound objects to form in the universe, and the smallest structures observable today. The formation times and the abundance of dwarf galaxies distinguish cosmological models.

- Dwarf galaxies are believed to be the most dark-matter dominated objects in the universe. They are important both for quantifying the cosmic content of dark matter, and for a detailed understanding of its properties. They are the most promising target for direct detection of dark matter annihilation, with a signature that would strongly depend on their internal structure.

- Due to their shallow potential wells, dwarf galaxies are sensitive laboratories for studying the physical processes relevant to galaxy formation in general. These include re-ionization, cooling, star formation, supernova feedback and galaxy interactions.

- In the hierarchical framework, dwarf galaxies are linked to the building blocks of larger galaxies. An understanding of the formation and evolution of dwarf galaxies is key to understanding the formation of those galaxies which form partly through mergers.

In this chapter, I will review the cosmological and astrophysical background, and present an overview of the current observational picture of dwarf galaxies. Section 1.2 begins with a brief historic review of physical cosmology, followed by a description of the current picture of the homogeneous universe. This serves as a background for all later discussions. The formation of structure in the linear regime, and the hierarchical framework, which set the starting point for all the simulations, are presented in Section 1.3. Next, the astrophysical processes relevant for galaxy formation, and the role of dwarf galaxies as astrophysical laboratories, are described in Section 1.4. Section 1.5 concludes the introduction with a summary of the observational results of dwarf galaxies, and the current understanding of the formation and evolution of dwarf galaxies we derive from them. The numerical methods used in the simulations will be the topic of Chapter 2.

1.2 The Homogeneous Universe

A Brief History

On *large scales*, the universe is isotropic and homogeneous, meaning it looks the same in every direction, for every observer. It is perhaps surprising that what is arguably the most important axiom of cosmology has only been firmly tested observationally for a relatively short period of time. Hubble (1926) was the first to sample a significant volume of space, and deduce a uniform distribution of some 400 galaxies with measured absolute magnitudes. Hubble's result has been confirmed with increasingly larger samples, and modern surveys such as the CfA Galaxy Redshift Survey (Davis et al., 1982), the 2dF Galaxy Redshift Survey (Colless, 1999; Percival, 2001), and the Sloan Digital Sky Survey (SDSS) (e.g. Padmanabhan, 2007) map the large scale distribution of galaxies out to a distance of several billion light years. The nearly perfect isotropy and homogeneity of the early universe is also imprinted in the cosmic microwave background, first measured with precision by the COBE satellite Smoot (1992).

But the concept we now call the "Cosmological Principle" (e.g. Peebles, 1980) has been invoked much earlier, and for different reasons – some of which later turned out to be wrong. Early cosmological models were entirely phenomenological and inspired by philosophical principles, rather than physical laws. The Ptolemaic and the Copernican universes are both isotropic, but neither is homogeneous, placing the earth or the sun at their respective centres, orbited by the planets, and enclosed within a sphere of so-called fixed stars. The solar system first loses its special place in the model of Giordano Bruno, who proposed in 1584 that the sun was in fact merely one star amongst a myriad of others, which are not distributed on a sphere, but stretch out to infinity in all directions. The universe, according to Bruno, has no centre. It is both isotropic and homogeneous.

Still, the resulting equivalence of all observers, now somewhat ironically labelled the "Copernican Principle", was not by itself an observational result, nor did it make any predictions verifiable by observations at the time. It was, no more, no less, the only acceptable perspective for a cosmologist to take: after all, how would we be able to say anything about the universe if it looked different to every observer? Perhaps in retrospect, it is this bold assertion that we should be able to be cosmologists, that is, to be able to understand the cosmos, which made Bruno's heretic leap of faith so significant.

The era of *Physical Cosmology*, as we know it today, is a more recent development. By 1686, Newton demonstrated that an attractive force could explain the Keplerian motion of the planets, and hypothesised that all matter in the universe is subject to the same laws of motion and gravitational attraction. Soon after this, Newton, too, *discovered* the Copernican principle: He noticed that in order to be static, such a universe does not just have to be infinite, or else it would collapse to a point. In addition, it has to be *perfectly* homogeneous, or else it would be violently unstable to local gravitational collapse. Newton thus devoted some time to trying to confirm that the distribution of stars that could be observed was indeed homogeneous. His effort failed, and Herschel later showed that, in fact, the observable distribution of stars was not at all homogeneous, but arranged in a disk. What both Newton and Herschel did not know was that the volume they observed was truly tiny. I will return to the significance of homogeneity on *large scales* in the next sections, and derive a precise definition of *large* and *small* in this context.

1.2.1 The Expanding Universe

Once established, for homogeneity and isotropy to be preserved at all times, any large scale motions must also be homogeneous and isotropic. A static universe, having no large scale motions, trivially satisfies this constraint, but it is not required: More generally, motions of the form

$$\dot{r} = f(t)r \tag{1.1}$$

are allowed, where $f(t)$ is a function of time only, and positive (or negative) values of f correspond to uniform expansion (or contraction). Integrating Equation 1.1 with time lets us recast the relationship as $r(t) = a(t)x$, so that the time evolution is contained entirely in the time evolution of the *scale factor* $a(t)$, related to the function $f(t)$ via $f(t) = \dot{a}/a$. The new coordinate x is called the *comoving* coordinate, constant for any body that is not subject to additional, peculiar motions. In contrast, the *physical* or *proper* coordinate r changes with time, provided that $\dot{a} \neq 0$. That the universe is indeed not static, but expanding, was discovered from the observed recession of distant galaxies by Hubble (1929).

All information about the large scale behaviour of the universe is thus contained in the evolution of the scale factor and its time derivatives. It can be shown (e.g. Weinberg, 2008, p.2)that the generalised geometries satisfying Equation 1.1 take the form of surfaces with radius a embedded into 3+1 dimensional space-time. If we define a comoving coordinate system such that observers at rest with respect to the expanding or contracting space keep their coordinates fixed, the line element on these surfaces in polar coordinates (r, Ω) gives the Robertson-Walker metric:

$$ds^2 = dt^2 - a^2(t) \left(\frac{dr^2}{1 - kr^2} + r^2 d\Omega^2 \right) \tag{1.2}$$

The constant k is called the normalised curvature, with flat space corresponding to $k = 0$, while $k = +1$ and $k = -1$ denote the hyper-spherical (*closed*) and hyperboloid (*open*) cases. After substitution of Equation 1.2 into Einstein's field equations, the tensorial, general relativistic analogues of the Newtonian equations of motion, the non-vanishing $^0{}_0$ component and the trace yield the two Friedmann equations, which determine the time evolution of the scale factor (see Weinberg (2008) for a full derivation):

$$\left(\frac{\dot{a}}{a} \right)^2 = \frac{8\pi G}{3}\rho - \frac{kc^2}{a^2} + \frac{\Lambda c^2}{3} \tag{1.3}$$

$$\frac{\ddot{a}}{a} = -\frac{4\pi G}{3} \left(\rho + \frac{3p}{c^2} \right) + \frac{\Lambda c^2}{3} \tag{1.4}$$

Equation 1.3 relates the expansion rate of the universe to its matter density ρ, the value of the cosmological constant Λ, and the curvature k. Conventionally, the present scale factor a_0 is fixed to unity (note that the subscript zero always refers to present-day values). The present expansion rate defines the *Hubble* constant $H_o \equiv \dot{a_0}/a_0$, and the dimensionless constant h, which for historical reasons corresponds to a Hubble constant of $h \times 100$ kms^{-1}Mpc^{-1}. Equation 1.4 is called the acceleration equation, and also depends on the equation of state parameter w, relating the density ρ to the pressure p.

Conservation of energy implies that the universal mean densities of matter $\rho_m(t)$ and primordial radiation $\rho_\gamma(t)$ evolve as:

$$\rho_m(t) = \rho_{m0} \ a^{-3}(t) \tag{1.5}$$

$$\rho_\gamma(t) = \rho_{m0} \ a^{-4}(t) \tag{1.6}$$

where the additional factor of a^{-1} in the radiation density is due to the relation of the photon energy to its wavelength, which is stretched, or *redshifted*, in an expanding universe: $\epsilon_\gamma \propto \lambda^{-1} \propto a^{-1}$.

In order to compare different world models where these quantities take different values, it is useful to express the constituents of the universe in terms of density parameters, defined as $\Omega_X \equiv \rho_X/\rho_c$, where the critical density $\rho_c = 3H_0^2/(8\pi G)$ corresponds to the matter density required for $\Lambda = k = 0$.

In a universe with $\Lambda = 0$ and $\rho > 0$, it follows from Equation 1.4 that the expansion is always decelerating, and from Equation 1.3 that matter densities below and above the critical density are equivalent to negative and positive curvature, respectively. In the case of $k < 0$, the right hand side of Equation 1.3 is always positive, and the universe will expand forever with a finite expansion rate. In the case of $k > 0$, Equation 1.3 has a solution where $\dot{a}/a = 0$. At this point, the expansion factor reaches a maximum, and the universe will re-collapse. If $k = 0$, the right hand side of Equation 1.3 remains positive, but with $\rho \to 0$, $\dot{a}/a \to 0$. The universe continues to expand forever, but with an ever decreasing rate.

Curvature of space is observable, because it affects the relation of apparent diameter and distance of far-away objects. Measurements of the apparent angular scale of the CMB residuals, combined with baryon acoustic oscillations (Komatsu, 2010), yield $-0.0133 < \Omega_k < 0.0084$, i.e. consistent with a flat geometry, or $\Omega = 1$. The universal abundance of deuterium produced during nucleosynthesis, as well as results from the CMB, are consistent with a baryon fraction (both visible and invisible) of only $\Omega_m = 0.046$, and a negligible contribution of radiation today ($\Omega_\gamma \sim 5 \times 10^{-5}$). On the other hand, the structure in the CMB, the observed large scale structure at different redshifts (also see Section 1.3), and the dynamical mass estimates of virialized objects through kinematics and weak lensing, are all consistent with a further contribution of a clumpy component called *dark matter*, which accounts for $\Omega_{DM} = 0.23$. Thus, the total density Ω being close to unity, the universe must presently be dominated by the cosmological constant term $\Omega_\Lambda = 0.73$. According to Equation 1.4, this implies an accelerated expansion, i.e. $\ddot{a}/a > 0$. Measurements of the recession velocity of distant supernovae (e.g. Perlmutter & The Supernova Cosmology Project, 1999) indicate that the universe is indeed accelerating. The large scale evolution of the universe is consistent with a cosmological constant, or a vacuum energy density whose equation of state parameter is $w = -1$. The best estimate of the Hubble parameter from 7 year WMAP results is $H_0 = 71 \pm 2.5 \mathrm{kms}^{-1}\mathrm{Mpc}^{-1}$ (Komatsu, 2010). It is worth remembering however, that the quoted measurement uncertainties are not completely uncorrelated, and that only twenty years ago, values of H_0 between 50–100 ($h = 0.5 - 1$) were debated.

While the precise determination of the cosmological parameters remains a principal goal of observational cosmology, the precision of measuring the large scale structure has now reached a point where the effects of baryons and galaxy formation become significant (Van Daalen, 2011, in prep.). Studies of galaxy formation are also used to investigate whether the inferred cosmological background is consistent with the observable universe on much smaller scales.

But of course, we already know that on small scales, the universe is in fact highly inhomogeneous and anisotropic. At ~1 gcm^{-3}, the density of a star is about 10^{23} times greater than the mean density of the Milky Way, which is another million times higher than the mean density of the universe today ($\rho_c \sim 10^{-29}$ gcm^{-3}). Studies of galaxy formation are required to investigate whether the parameters inferred from the cosmic evolution are also consistent with the observable universe on much smaller scales. Evidently, the qualification that the universe is only homogeneous on large scales is important.

1.3 Structure Formation

As Newton realised, a perfectly homogeneous universe would remain so forever. The fact that we can observe structure today implies that some process in the early universe was responsible for generating inhomogeneities. This origin of structure is thought to be due to quantum fluctuations, which are amplified to macroscopic scales during inflation in the very early universe. Because inflation is a power-law process, and new structures are generated throughout the period of inflation at the same physical scale, the universe is, at the end of inflation, filled with perturbations on all scales, with amplitude $P(k) \propto k$. This so-called Harrison-Zel'dovich spectrum (Harrison, 1970; Zeldovich, 1972) is consistent with the CMB results (Tegmark, 1996).

For the subsequent evolution of structure (after the radiation-dominated era, which lasts for $\sim 70,000$ years), there are two fundamentally different concepts. In the so-called "bottom-up" scenario, small structures form first, and larger structures form later, including (but not exclusively) through the merger of smaller objects. In the "top-down" scenario, the largest structures form first, and later fragment. Bottom-up and top-down formation are also identified with "cold" and "hot" dark matter. As will be explained in Section 1.3.2, dwarf galaxies form very differently in these two scenarios. In addition, in intermediate so-called "warm" dark matter models (Section 1.3.4), there is a transition from bottom-up to top-down structure formation, and current observational constraints put the maximal transition scale right in the regime of dwarf galaxies.

For the description of the growth of structure in the matter-dominated era, the classical Newtonian equations of motion are used, but applied to the background

of an expanding universe, governed by the Friedmann Equations (Equations 1.3 and 1.4) of General Relativity. This approach is applicable to small velocities $v \ll c$, weak fields, and scales much smaller than the horizon. We also make use of another General Relativistic result in Birkhoff's theorem, which states that the evolution of a small region of space can be considered independent of a homogeneous background. A similar combination of classical equations for gravity, hydrodynamics and sub-grid physics, applied on comoving coordinates that expand with the uniform background, is also used in all numerical simulations presented in the following chapters.

In the next paragraphs, my discussion follows a path that is found in several textbooks, including Peebles (1980), Ryden (2002), Padmanabhan (2006) and Mo et al. (2010), as well as the lectures by A. Jaffe and H. Böhringer, and lecture notes available from A. Dekel, J. Primack. and H. Weinberg.

1.3.1 Linear Theory

On large scales, in the matter dominated epoch, matter in the universe can be considered as a non-relativistic collisionless fluid of density ρ, with the time evolution of a fluid element, at fixed coordinates $(\mathbf{r}, t)$ moving with velocity $\mathbf{u}(\mathbf{r}, t)$, described by the following set of hydrodynamic equations:

$$\left(\frac{\partial \rho}{\partial t} \right)_{\mathbf{r}} + \vec{\nabla}_{\mathbf{r}} \cdot (\rho \mathbf{u}) = 0 \tag{1.7}$$

$$\left(\frac{\partial \mathbf{u}}{\partial t} \right)_{\mathbf{r}} + (\mathbf{u} \cdot \vec{\nabla}_{\mathbf{r}}) \mathbf{u} = -\frac{1}{\rho} \vec{\nabla}_{\mathbf{r}} p - \vec{\nabla}_{\mathbf{r}} \Phi \tag{1.8}$$

$$\nabla_{\mathbf{r}}^2 \Phi = 4\pi G \rho \tag{1.9}$$

Equations 1.7 and 1.8 are the continuity and the Euler equations, that express the conservation of mass and the three components of momentum. Equation 1.9 is the Poisson equation for the gravitational field Φ. For a complete description of the six degrees of freedom of $\mathbf{r}$ and $\mathbf{u}$, in the most general case, an additional constraint is required, which can be provided in the form of an equation of state.

In an expanding universe, it useful to make a transformation to comoving coordinates $\mathbf{x} = \mathbf{r}/a(t)$, whose values remain constant for fluid elements at rest relative to the expanding background. In order to cast Equations 1.7 to 1.9 into a form suitable for a perturbative ansatz, we will further introduce two more quantities; the *peculiar velocity* $\mathbf{v}(t) = (\dot{ax}) - \dot{a}x = a\dot{x}$, and the *density contrast* $\delta(\mathbf{x}, t)$. The peculiar velocity is related to the physical velocity via $\mathbf{v} = \mathbf{u} - (\dot{a}/a)\mathbf{r}$, subtracting from the motion of the fluid element the motion due to the expanding background. The density contrast $\delta(\mathbf{x}, t)$ is expressed in terms of the local density $\rho(\mathbf{x}, t)$ and

the background density $\bar{\rho}(t)$ as $\rho(\mathbf{x}, t) = \bar{\rho}(1 + \delta(\mathbf{x}, t))$. These transformations ensure that small perturbations relative to the comoving mean velocity and to the mean density correspond to small values of $\mathbf{v}$ and δ, so that higher order terms can be neglected.

By the chain rule, the differential operators in Equations 1.7 to 1.9 transform as:

$$\nabla_{\mathbf{x}} f = a \nabla_{\mathbf{r}} f; \qquad \frac{\partial f}{\partial t}\bigg|_{\mathbf{x}} = \frac{\partial f}{\partial t}\bigg|_{\mathbf{r}} + (\dot{a}/a)\mathbf{x} \cdot \nabla_{\mathbf{x}} f \qquad (1.10)$$

After substitution, and dropping the subscript x, Equations 1.7 to 1.9 can now be expressed in comoving form, and in terms of the peculiar velocity and density contrast:

$$\frac{\partial \delta}{\partial t} + \frac{1}{a}\vec{\nabla} \cdot ((1 + \delta)\mathbf{v}) = 0 \qquad (1.11)$$

$$\frac{\partial \mathbf{v}}{\partial t} + \frac{\dot{a}}{a}\mathbf{v} + \frac{1}{a}(\mathbf{v} \cdot \vec{\nabla})\mathbf{v} = -\frac{1}{a}\vec{\nabla}\phi - \frac{1}{a\rho}\vec{\nabla}p \qquad (1.12)$$

$$\nabla^2 \phi = 4\pi G a^2 \delta \bar{\rho} \qquad (1.13)$$

where the identity $\ddot{a} = -\frac{4\pi}{3}G\bar{\rho}a$ has been used from the acceleration equation (1.4), and the gravitational potential Φ has been replaced by

$$\phi = \Phi(x, t) - \frac{2\pi}{3}G\bar{\rho}a^2 x^2 \qquad (1.14)$$

which gives rise to an attractive force for overdense regions, where $\delta > 0$, and a repulsive force for underdense regions, where $\delta < 0$.

From the Euler equation (1.12), one notes that in the absence of external forces, when the right hand side is zero, any peculiar velocities $\mathbf{v}$ decay with the expansion of the universe. For the same reason, vortices decay, which is one of the basic assumptions of kinetic perturbation theory, discussed in Section 1.3.3.

Linear Growth

For small inhomogeneities, $\delta, \mathbf{v} \ll 1$, and second order terms such as $\delta\mathbf{v}$ and $\mathbf{v} \cdot \vec{\nabla}\mathbf{v}$ can be ignored. The continuity and Euler equations (1.11 and 1.12) can be approximated to linear order as:

$$\frac{\partial \delta}{\partial t} + \frac{\vec{\nabla} \cdot \mathbf{v}}{a} = 0 \qquad (1.15)$$

$$\frac{\partial \mathbf{v}}{\partial t} + \frac{\dot{a}}{a}\mathbf{v} = -\frac{1}{a}\vec{\nabla}\phi - cs^2\vec{\nabla}\delta \qquad (1.16)$$

where the sound speed $c_s^2 = \frac{\partial p}{\partial \rho}$ has been substituted using $\vec{\nabla} p = \frac{\partial p}{\partial \rho} \vec{\nabla} \rho$. By taking the time derivative of Equation 1.15 and the spatial derivative of Equation 1.16, one obtains the following general equation for the evolution of a density perturbation δ:

$$\ddot{\delta} + 2\frac{\dot{a}}{a}\dot{\delta} = 4\pi G \bar{\rho}\delta + \frac{c_s^2}{a^2}\nabla^2\delta \tag{1.17}$$

Equations 1.15 and 1.17 can be solved for different limiting cases appropriate for different cosmological epochs, depending on the dominating contributions to the density ρ, the respective equation of state, and the time evolution of the scale factor $a(t)$.

In the local limit where $\dot{a}$ is negligible, the second term on the left-hand side of Equation 1.17 vanishes. Solutions take the form of sound waves $\delta(t,x) = \delta_0 e^{i(kx - \omega t)}$, with the dispersion relation $\omega^2 = c_s^2 k^2 - 4\pi G\bar{\rho}$.

The Jeans wavelength $\lambda_J \equiv \frac{2\pi}{k_J} = c_s\sqrt{\frac{4\pi}{G\bar{\rho}}}$ determines a characteristic length scale: perturbations on scales $\lambda < \lambda_J$ are small enough so that sound waves travelling with c_s can cross in less than one dynamical time $t_{dyn} \sim (G\rho)^{-1/2}$. In this case, ω is real, corresponding to pressure waves that oscillate, but do not grow. Perturbations with $\lambda > \lambda_J$ are unstable to gravitational collapse, because pressure waves cannot build up fast enough. They correspond to imaginary values of ω, which leads to solutions for δ that grow exponentially with time. In the limiting case $\lambda \gg \lambda_J$, the internal pressure can be ignored, and $\omega \sim \frac{1}{t_{dyn}}$.

In an expanding background ($\dot{a} \neq 0$) dominated by matter, the Friedmann equations give $\Omega_m(\frac{\dot{a}}{a})^2 = \frac{8\pi G\bar{\rho}}{3}$. Substituting on the right-hand side, Equation 1.17 simplifies to:

$$\ddot{\delta} + 2\frac{\dot{a}}{a}\dot{\delta} = \frac{3}{2}\Omega_m\left(\frac{\dot{a}}{a}\right)^2\delta \tag{1.18}$$

where the pressure term has been dropped. In the matter dominated era, $a \propto t^{2/3}$ and $\frac{\dot{a}}{a} = 2/3\ t^{-1}$ for the case that $\Omega_m = 1$, which can be used to cast the equation into a form where the time dependence is contained in δ only:

$$\ddot{\delta} + \frac{4}{3t}\dot{\delta} = \frac{2}{3t^2}\delta \tag{1.19}$$

Here, the most general solutions take a power-law form. The growing mode evolves as $\delta(t) \propto t^{2/3} \propto a$, thus the density perturbations grow linearly with the scale factor.

1.3.2 Collapse

In the linear approximation, the self-gravity of perturbations is ignored when terms of order δ^2 are dropped. In reality, there will be a point when self-gravity dominates, and perturbations start to collapse to form gravitationally bound systems. In this case, when $\delta \sim \bar{\rho}$, the linear approximation is no longer valid.

Following Padmanabhan (2006), let us consider a spherical overdense region of radius $r(t)$, where the density $\rho(t) = M \frac{3}{4\pi r(t)^3}$ exceeds the background density $\bar{\rho}$. Assuming, by Birkhoff's theorem, that mass outside of the sphere has no effect, equating the kinetic and potential energy of a thin shell at the radius $r(t)$ gives:

$$\frac{d^2 r}{dt^2} = -\frac{GM}{r^2} \tag{1.20}$$

which has solutions of the form (see Padmanabhan (2006), p. 235):

$$r(t) = A(1 - \cos\theta); \quad t = B(\theta - \sin\theta); \quad A^3 = GMB^2 \tag{1.21}$$

Substituting for the background density $\bar{\rho}(t) = \rho_0 a(t)^{-3} = H_0^2 \frac{3}{8\pi G} a(t)^{-3}$ (for a matter dominated universe with $\Omega = 1$) in the relation of mass and density, we obtain the following relation for the density contrast of the sphere:

$$\frac{\rho}{\bar{\rho}} = \frac{2GM}{H_0^2} \left(\frac{a(t)}{r(t)} \right)^3 = \frac{9}{2} \frac{(\theta \sin\theta)^2}{(1 - \cos\theta)^3} \tag{1.22}$$

where the second equality is obtained after substituting the solution for $r(t)$ from Equation 1.21, and using the identity $H_0 t_0 = 2/3$ in the matter-dominated era.

The maximal expansion radius r_{max} is reached when $\theta = \pi$. This is called the turn-around radius, and it corresponds to the point where the self-gravitational collapse dominates over the expansion of space. Denoting by the subscript i the initial state of the perturbations, and using the relation $t/t_i = (1 + z_i)/(1 + z)$ throughout the matter-dominated era, one can show that with an initial perturbation δ_i, the turn-around redshift z_{max} is given by:

$$(1 + z_{max}) = \frac{\delta_i (1 + z_i)}{\pi^{2/3} (3/4)^{2/3}} \sim 0.57 (1 + z_i) \delta_i \tag{1.23}$$

Note that it follows from Equation 1.21 that as $\theta \to 2\pi$, $r(t) \to 0$ at a time $t_{coll} \equiv 2 \times t_{max}$. However, the assumptions for spherical collapse eventually break down for a real system, where dynamical relaxation causes it to reach virial equilibrium and a finite size and density after approximately twice the turnaround time. Assuming that at turn-around, all the energy is potential energy, and applying the scalar virial theorem, one finds that the virial radius r_{vir} is half of r_{max}, while the density ρ_{vir} is $8\rho_{max} = 8\rho(t_{max}) = 44.8\bar{\rho}(t_{max}) \sim 179\bar{\rho}(t_{coll})$.

Objects that collapse under self-gravity remain frozen at r_{vir} and ρ_{vir}, but due to the expanding nature of the universe, their density contrast still increases with time.

From Equation 1.23, it can be seen that smaller perturbations collapse first, which directly leads to the hierarchical formation scenario. For dwarf galaxies, with virial radii of a few kpc, the predicted turn-around redshift is around $z \sim 20$. In this bottom-up scenario, larger haloes form later, both through independent collapse of larger perturbations, but also through mergers of existing smaller objects.

The independence of collapse at different scales δ_i lends itself to spectral analysis, which considers the time evolution of an initial Gaussian random field. The result of this analysis, called Press-Schechter theory, can be expressed in terms of a time-dependent halo multiplicity function (see Chapter 5), or equivalently, as the fraction of collapsed objects as a function of mass and time. It can also be used to derive the contribution of haloes of each mass to the universal mass density Ω over time. For rare objects such as galaxy clusters, the observed abundance provides a tight constraint on the linear density contrast σ_L of the corresponding mass. A common way of describing the power spectrum is the parameter σ_8, which corresponds to a present-day scale of $8h^{-1}$ Mpc, or about $10^{14} M_\odot$.

The largest bound objects in the universe today are "super clusters" of galaxies, with masses of up to $\sim 10^{15} M_\odot$, and diameters up to several 10s of Mpc, in agreement with the bottom-up scenario. The prediction that even larger structures are presently collapsing can be observed in redshift space as "Great Walls", caused by objects moving towards their common gravitational centre. At even larger scales, beyond ~ 100Mpc, the universe is still homogeneous today.

1.3.3 Kinematic Perturbation Theory

An alternative analytic approach to structure formation is based on a kinematic ansatz, which assumes that fluid elements (or particles) with initial Lagrangian coordinates $\mathbf{q}$ move to their final comoving, Eulerian coordinates $\mathbf{x}(\mathbf{q}, t)$ under the action of a displacement field $\psi(\mathbf{q}, t)$:

$$\mathbf{x}(\mathbf{q}, t) = \mathbf{q} + \psi(\mathbf{q}, t) \tag{1.24}$$

1.3.3.1 The Zel'dovich Approximation

Under the *Zel'dovich approximation* (Zel'Dovich, 1970), the displacement field is proportional to the initial displacement multiplied by the *growth factor D*, and particles continue to move with constant velocities in the direction of the initial

displacement:

$$\mathbf{x}(t) = \mathbf{q} + D(t)\psi_i(\mathbf{q}); \qquad \dot{\mathbf{x}}(t) = \dot{D}\psi_i; \qquad \ddot{\mathbf{x}}(t) = \ddot{D}\psi_i \qquad (1.25)$$

With the linearization $\ddot{\mathbf{x}} \propto \dot{\mathbf{x}}$, the displacement field is related via the Euler equation (1.12) to the initial gravitational potential: $\psi_i(\mathbf{q}) = -\nabla\phi_i$. The deformation of an initial fluid element in Eulerian coordinates under the action of the displacement field ψ and the expansion $a(t)$ gives rise to the deformation tensor D_{ik}, which can be viewed as a 3×3 Jacobian matrix if Equation 1.25 is interpreted as a coordinate transformation from $\mathbf{q}$ to $\mathbf{x}$:

$$D_{ik} \equiv \frac{\partial \mathbf{x}_i}{\partial \mathbf{q}_k} \qquad (1.26)$$

In the Zel'dovich approximation, all motions are linear, which guarantees that D_{ik} is symmetric, and that it can be diagonalised to principal axes $i = (1, 2, 3)$, with eigenvalues $\lambda_i = \frac{\partial\phi^2}{\partial^2 q_i}$. Mass conservation within a perturbed region with initial volume d^3q and density $\rho(t_i) \sim \bar{\rho}$ requires that $\rho(\mathbf{x}, t)J\, d^3q = \rho(\mathbf{x}, t)\, d^3x = \rho(t_i)\, d^3q$, where $J = |D|$ is the Jacobian (trace) of the transformation. Substituting from Equation 1.26, it follows that

$$\rho(\mathbf{x}, t) = \bar{\rho}\frac{1}{(1 - D(t)\lambda_1)(1 - D(t)\lambda_2)(1 - D(t)\lambda_3)} \qquad (1.27)$$

Thus, the density diverges at time t if $D(t)\lambda_i \to 1$ for any eigenvalue of the deformation tensor, leading to the formation of caustics. Because of the linear nature, each dimension collapses independently. Triaxial perturbations will first collapse in one dimension (corresponding to the largest eigenvalue λ_1, given by the smallest principal axis, where the gradient of the potential is maximal), leading to two-dimensional, so-called *pancake* structures. If the two largest eigenvalues are similar, the perturbation collapses to a one-dimensional *filament*, and if all three eigenvalues are similar, to a point-like *halo*. For a distribution of eigenvalues originating from Gaussian random fields, it can been shown (Bouchet, 1996, and references therein) that the first two cases are dominant. Note that the ansatz breaks down when collapsing shells cross the origin in accordance with the linear motions, so there is no true sequential collapse from sheets to filaments to haloes. The filamentary structure observed in the *cosmic web* can be predicted from the Zel'dovich approximation, when combined with additional assumptions about the spatial distribution of the initial perturbations.

1.3.3.2 Higher Order Perturbations

Equation 1.27 can be expressed in terms of the density contrast δ, and expanded:

$$\delta = \frac{\rho}{\bar{\rho}} - 1 = -D(\lambda_1 + \lambda_2 + \lambda_3) + D^2(\lambda_1\lambda_2 + ...) + D^3(\lambda_1\lambda_2\lambda_3) + ... \quad (1.28)$$

To linear order, and using the relations of Equation 1.25, Equation 1.28 can be written as:

$$\delta = -D(\lambda_1 + \lambda_2 + \lambda_3) = -D\nabla \cdot \psi = -D\nabla \cdot \frac{\dot{\mathbf{x}}}{\dot{D}} = -\frac{D}{\dot{D}}\nabla\mathbf{v} \quad (1.29)$$

By substituting from the linear-order Euler equation (1.15), one finds that the time dependence of the *linear* growth factor D obeys the same relation as Equation 1.17:

$$\ddot{D} + 2\frac{\dot{a}}{a}\dot{D} = 4\pi G\bar{\rho}D \quad (1.30)$$

Factorising the largest eigenvalue λ_1 from the higher order terms, one can see that the errors in going from Equation 1.28 to 1.29 are small, as long as $\lambda_1 \gg \lambda_2, \lambda_3$ (i.e. the pancake regime), or while $D\lambda_1 \ll 1$. In particular, for the formation of haloes ($\lambda_1 \sim \lambda_2 \sim \lambda_3$), the approximation is valid only in the linear regime. Relaxing the linear assumption of the Zel'dovich approximation leads to a general class of higher order Lagrangian perturbation theories (Moutarde et al., 1991; Bouchet et al., 1995).

The kinematic ansatz is also important for evolving the primordial velocity and density fields within the linear regime, in order to create initial conditions for numerical simulations. As discussed in Section 2.1, the customary method is to apply the Zel'dovich approximation, which is also used for the simulations in Chapters 3 and 4. For higher precision, a second-order Lagrangian scheme (Jenkins, 2010) is used for the initial conditions in Chapter 5.

1.3.4 Warm Dark Matter

In cold dark matter models, there is no lower limit of structures in the matter-dominated era. By contrast, in *warm* or *hot* dark matter models with density parameter Ω_X, the finite particle mass m_X sets a minimum scale below which fluctuations are smoothed out by the free streaming motion of the particles. By equating the crossing time of a particle (e.g. a light neutrino with g_X degrees of freedom) moving with the thermal velocity corresponding to its mass at matter-radiation equality, and the comoving horizon scale at the time, Bond & Szalay

(1983) derive the following order-of-magnitude estimate for the scale on which fluctuations are damped out:

$$R_S \sim 0.2(\Omega_X h^2)^{\frac{1}{3}} \left(\frac{1.5}{g_X}\right)^{\frac{1}{3}} \left(\frac{m_X}{keV}\right)^{-\frac{4}{3}} \text{Mpc} \tag{1.31}$$

From a derivation along similar lines to the linear perturbation theory described in Section 1.3.3, Bode et al. (2001) derive a more accurate characteristic mass scale for this so-called Landau-Damping, which corresponds to the comoving half-wavelength at which the linear perturbation amplitude is suppressed by a factor of two:

$$R_S \sim 0.31 \left(\frac{\Omega_X}{0.3}\right)^{.15} \left(\frac{h}{0.65}\right)^{1.3} \left(\frac{m_X}{keV}\right)^{-1.15} h^{-1}\text{Mpc} \tag{1.32}$$

This corresponds to a characteristic mass scale below which structures could only be formed via fragmentation, or top-down mechanisms:

$$M_S \sim 10^{10} \left(\frac{\Omega_X}{0.3}\right)^{1.45} \left(\frac{h}{0.65}\right)^{3.9} \left(\frac{m_X}{keV}\right)^{-3.45} h^{-1}\text{M}_\odot \tag{1.33}$$

It should be noted that cold dark matter, and particularly ΛCDM, is very successful at describing structure formation, and the observed abundance of galaxies match the predictions of Press-Schechter theory over many orders of magnitude. So-called *hot* dark matter models ($m_X \lesssim 1$ eV) are ruled out; the inefficiency of structure formation in such models, combined with the amount of structure seen today, would require more structure at high redshift than is observed. Current limits from structures in the Lyman-α forest constrain $m_X > 1keV$, which would correspond to masses of the order of $10^{10}\text{M}_\odot$. This makes dwarf galaxies very interesting probes for studying different dark matter models. It should also be noted that, in reality, there is no discrete threshold between the two regimes, as Equation 1.33 might suggest. Numerical simulations of warm dark matter by Zavala et al. (2009) (which are realised by an appropriate cut-off in the initial power spectrum, but cannot yet take into account the kinetic effect of thermal velocities), have explored the change in the halo multiplicity function for different cosmologies. They show that the number of $10^{10}\text{M}_\odot$ haloes at $z = 0$ would decrease by about a factor of 3 for a particle mass of $m_X = 1 \, keV$. In light of the excess of dwarf galaxies shown in Chapter 5, this is a very interesting result.

1.4 Galaxy Formation

Even though the evolution of the universe appears to be dominated by dark matter and dark energy, both cannot be directly observed. How the observable components, i.e. gas, stars and galaxies, trace the total matter distribution over time, is determined by the physics of galaxy formation. The extent to which we can understand both the large scale evolution of the universe, as well as the formation of structure, therefore depends on our understanding of galaxy formation.

According to the current paradigm, supported by simulations, galaxies form when gas cools inside dark matter haloes (c.f. Section 1.3.2), through a combination of dissipational and dissipationless processes (White & Rees, 1978). Mergers and interactions, which influence the subsequent evolution of galaxies, also depend on the formation and relative motions of their respective haloes. Consequently, galaxies and the stars and gas inside them are visible tracers of the matter distribution, but there is no one-to-one correspondence of galaxies and dark matter haloes. The *bias* (Silk, 1985) that describes the deviation from proportionality depends on time, environment and mass, and generally on all processes that influence galaxy formation. The difference is particularly important in the dwarf galaxy regime, where the $M_\star$-M_{DM} relation is very steep, resulting in far fewer low-luminosity galaxies observed compared with the number of dark matter haloes predicted from cosmological models. In order to connect the dark to the visible universe, it is important to correctly account for all relevant astrophysical processes (see Chapter 3), but the prediction of the faint end of the luminosity function remains a challenge, for simulations, and for cosmological models (see Chapters 5 and 6).

1.4.1 Physical Mechanisms

The *dissipational* processes involved in galaxy formation are generally more complicated than the dissipationless physics of gravity (in the weak field limit). On the other hand, a balance of positive and negative electric charges on large scales leads to a cancellation of electric forces, effectively limiting their range. Thus, the more complicated equations of hydrodynamics generally only have to be solved locally, or for neighbouring fluid elements (also see Section 2.2.2).

The principal mechanisms determining the formation of galaxies in dark matter haloes are the heating and cooling of intergalactic and interstellar gas, star formation, and chemical as well as energetic feedback. An overview of the processes relevant to galaxy formation is given by Tormen (1996). The following list describes the main mechanisms that govern the thermal evolution of the gas, and summarises their implementation in the simulations.

- Gas which falls into a halo undergoes compression, and if no heat is lost, the work done during the process is converted into internal energy. Conversely, if the gas in a galaxy expands, the work required reduces its internal energy.

- Viscosity transforms the kinetic energy of ordered motions, such as infalling gas clouds or supernova ejecta, into random motions of particles, thereby creating heat and entropy. A very effective form of viscous heating occurs in shocks, where the bulk speed exceeds the local sound speed of the medium, as would be expected for supernova ejecta in the ISM. Because the resolution of shocks and the resulting heat production is difficult to model in numerically, thermal energy is injected directly in our simulation.

- UV, soft X-ray or cosmic ray radiation can all ionise, as well as heat the gas. The direct heating mechanism corresponds to the transfer of kinetic energy from the photon onto the gas particle. In addition, ionisation changes the cooling rate of the gas (see below). In the context of galaxy formation, the cosmic UV background, present since the epoch of re-ionization at $z \sim 6$, is the most important source of ionising radiation. In the intergalactic medium, the mean free path of UV photons is so large that a cosmic mean field can be assumed. Gas in galaxies, however, can reach high enough column densities to become self-shielding (see Section 3.4.3). In addition, local sources such as massive stars, individual AGN and supernovae may also play a role.

- Radiative cooling includes the inelastic scattering due to collisions between electrons, atoms and molecules, and the free-free scattering known as Bremsstrahlung in fully ionized gas. The cooling efficiency depends on the temperature, and the chemical composition, as this determines the available energy levels for bound-free and bound-bound transitions. At intermediate temperatures, most relevant to galaxy formation, the interstellar gas is assumed to be in collisional excitation equilibrium, and the cooling rate is proportional to ρ^2. At very low temperatures, where cooling is possible only via long-lived molecular excitations, the density dependence approaches proportionality to ρ. In the simulations, all these processes are included in the *cooling function* $\Lambda(T, z)$, as shown in Figure 3.1.

- Inverse Compton scattering of electrons with lower energy photons leads to a transfer of energy to the background radiation field, which has a cooling effect on the gas. For galaxy formation, Compton cooling off the cosmic microwave background plays a role at high redshift, when the photon density of the CMB is high, but drops as $(1 + z)^{-4}$ (see Equation 1.5) for lower redshifts. The Compton effect also determines the initial gas temperature,

which is assumed to be equal to the temperature of the background radiation at high redshift.

It should be noted that unlike electric charges, currents that give rise to magnetic fields don't generally cancel out, leading to macroscopic objects such as planets, stars and even galaxies with net magnetic fields. Consequently, simulations such as those presented here, which do not include magneto-hydrodynamics, implicitly assume that the effects of magnetic fields are not crucial for galaxy formation, or that they can be absorbed in other parameters without being calculated explicitly.

In a way, dwarf galaxies represent an extreme case for many of the physical processes that govern galaxy formation. As I will demonstrate in Chapter 3 and 4, their shallow potential wells make them susceptible to both internal and external effects. In the first category, feedback from supernova winds are most important for dwarf galaxies. Externally induced factors include photoionization and heating by the cosmic UV background, as well as effects that depend strongly on the environment, such as tidal interactions and ram-pressure stripping. Their sensitivity to all these mechanisms makes dwarf galaxies challenging to model, but at the same time, extremely good laboratories for astrophysical processes, as well as their numerical implementations.

In the "hierarchical" scenario of structure and galaxy formation, large haloes and galaxies form partly due to the mergers of smaller objects (Searle & Zinn, 1978; Davis et al., 1985). While the picture that the dwarf galaxies we see today are the surviving building blocks of systems like the Milky Way is certainly oversimplified, no model of galaxy formation can be complete without an understanding of dwarf galaxy formation first.

1.5 Dwarf Galaxies

1.5.1 Classification

Very broadly, galaxies are divided into two classes: *Early type* galaxies are red, contain mostly old stars, a low gas fraction and little or no recent star formation. Their morphologies are elliptical, supported mostly by random stellar motions. *Late type* galaxies have bluer colours, indicative of active star formation. They have a higher gas content and generally possess a rotationally supported disk of varying thickness. They often include distinct morphological features such as bars and spiral arms, although they can also contain a pressure-supported bulge at the centre. It is worth noting, however, that the terms "early type" and "late type" imply a transition from the former to the latter along the so-called "Hubble Sequence", which is no longer believed to be true (in fact, as discussed

in Section 1.5.5 and in more detail in Chapter 4, environmental mechanisms can have the reverse effect). Perhaps, it is best to describe the observables directly, and avoid suggestive but potentially misleading terminologies.

By comparison, the distinction between *ordinary* and *dwarf* galaxies may appear rather benign, but it has been the cause for quite some controversy as well. Kormendy (1985) states that "dwarf spheroidals and ordinary ellipticals were formed in very different ways". According to Kormendy, the structural parameters of normal ellipticals and dwarf ellipticals define disjoint sequences on the fundamental plane, characterised by a break in central surface brightness of about four orders of magnitude. Apparently in contradiction, Misgeld et al. (2008) conclude that "dwarf ellipticals are not a separate class of objects, but rather the low mass counterparts of massive early type galaxies". Geha et al. (2002) and others find continuous scaling relations of luminosity-metallicity and metallicity-velocity dispersion. With more complete observations, Kormendy et al. (2009) have considerably narrowed the original "gap" in the fundamental plane, suggesting that what once appeared to be a forbidden region of parameter space is really only a sparsely populated one. They still find two distinct families of galaxies, following different relations of magnitude and surface brightness, that approach each other at $M_V \sim -18$. Combining data from Local Group dwarf spheroidals, Perseus and Antlia dwarf spheroidals and dwarf ellipticals, D05 dwarf ellipticals, GG03 dwarf ellipticals, as well as ordinary ellipticals, over the range of $M_V = -8$ to -24, de Rijcke et al. (2009) show that the slope of the relation between absolute magnitude and effective radius changes at around $M_V = -18$. Fainter galaxies follow a very weak relation of $\log(R_e) \propto -0.07 M_V$, while for brighter galaxies, the relation is more than three times as steep, with $\log(R_e) \propto -0.25 M_V$. Such a transition points to a threshold where different physics are important for dwarf galaxies; for example, where outflows become important.

Late type dwarf galaxies include dwarf irregulars and blue compact dwarf galaxies, and there appears no clear discontinuity between the most massive late type dwarfs, and ordinary late type galaxies (Tolstoy et al., 2009). Objects such as the Magellanic Clouds are at the high mass end of gas-rich, star forming dwarf galaxies. The LMC is close to the spiral galaxies like M33, while the SMC resembles the larger dwarf irregulars in the Local Group, such as NGC 6822 and IC1613.

At the low mass end, dwarf spheroidal galaxies also overlap with globular clusters in terms of stellar mass. Both also typically contain an old stellar population, and while most dwarf spheroidals show some (and in many cases, considerable) complexity of star formation, evidence of more than one stellar population is also found in some of the most massive globular clusters, most notably ω Cen. It has been suggested that these may be the surviving nuclei of infalling dwarf galaxies (e.g. Hilker & Richtler, 2000; Fellhauer et al., 2006).
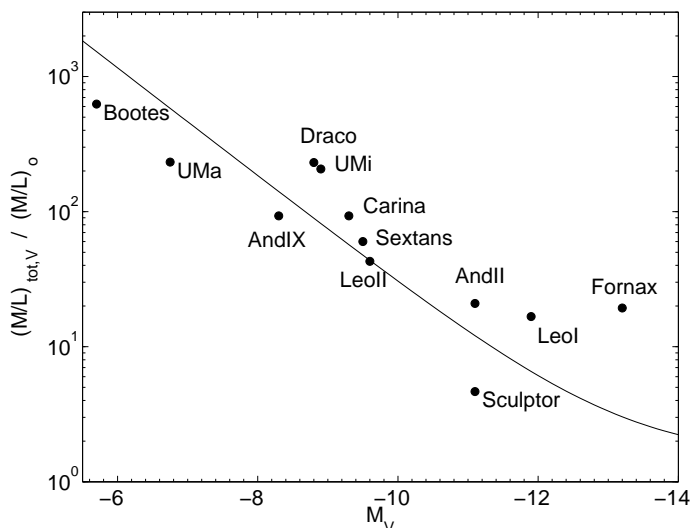
Figure 1.1: A "Mateo plot" (after Mateo (1998)), adopted from Gilmore et al. (2007) with updated data, showing the mass-to-light ratio of 12 Local Group dwarf spheroidal galaxies as a function of their luminosity. The solid line corresponds to a constant dark matter mass across the luminosity range. The range of luminosities is almost 8 magnitudes.

1.5.2 Dark Matter

Despite some similarities in their stellar populations, dwarf galaxies are clearly distinct morphologically and kinematically from globular clusters. This is attributed to the fact that all galaxies are embedded in dark matter haloes. It also separates "primordial" dwarf galaxies from so-called tidal dwarfs, which form in the tidal tails of interacting larger galaxies (e.g. Wetzstein et al., 2007). Dark matter in dwarf galaxies was first suggested by Faber & Lin (1983), and measurements of stellar velocity dispersions (e.g. Koch et al., 2007; Walker et al., 2007; Mateo et al., 2008; Walker et al., 2009) indicate that they possess the highest mass-to-light ratios of any known galactic systems. The ratio of gravitational mass to luminosity within the effective radius appears to reach a minimum at $\sigma \sim 180 \mathrm{kms}^{-1}$, with smaller galaxies increasing in mass-to-light ratio inversely proportional to their mass (Zaritsky et al., 2006). This is consistent with the result of abundance matching (see Chapter 5), and suggests that star formation is less efficient in smaller haloes. At the very faint end, an application of the virial theorem to systems with $L \sim 10^2 \mathrm{L}_\odot$, $\sigma = 6 \pm 2 \mathrm{kms}^{-1}$ suggests total mass to light ratios of 10^{3-6}. Such estimates are highly uncertain, however, as they rely on as-

sumptions about the anisotropy of orbits, the fraction of binary stars, the absence of tidal effects, and the shape of the dark matter potential, none of which can be measured reliably in such small systems (Walker et al., 2007). Nevertheless, given that ΛCDM predicts an abundance of much smaller haloes, the fact that no galaxies are observed with $\sigma \sim 0$ points to the idea that star formation reaches a limit at finite halo masses, which requires an astrophysical explanation. Figure 1.1 shows the so-called "Mateo plot" of 12 Local Group dwarf spheroidals, comparing their luminosities to their kinematically inferred mass-to-light ratios. The solid line corresponds to a *constant* dark matter mass for all objects, a proposal that was also taken up by Strigari et al. (2008). While the dwarf galaxies in this plot show a weak correlation of mass with luminosity (in agreement with our simulations), the nearly constant mass indicates that they live near a threshold, where star formation efficiency drops very rapidly. This is the subject of Chapter 3.

It should also be noted that alternatives to dark matter exist, that may explain the present day stellar kinematics (Angus et al., 2008), although not necessarily the formation of dwarf galaxies, as described in Section 1.3.4. The detailed study of the formation of dwarf galaxies is therefore important to understand precisely the role of dark matter in galaxy formation, and whether the results of the simulations in ΛCDM are fully consistent with observations.

1.5.3 Observations

Traditionally, the observations of dwarf galaxies have followed two different lines of study. The "local approach" involves detailed observations of nearby dwarf galaxies; their structure, stellar populations and star formation histories, gas content, metallicity, stellar and gas kinematics and inferred dark matter content. The "cosmological approach" is based on deep galaxy counts and large surveys, which result in luminosity functions for different types of dwarf galaxies, and only very broad information such as colours and sizes for individual objects. More recently, this distinction has been blurred: dwarf spheroidal galaxies have now been observed in some detail in Clusters such as Virgo and Fornax with instruments such as the HST, while most Local Group dwarf spheroidals were actually discovered in large area surveys such as SDSS. Nevertheless, there still exists a gap in the understanding of nearby and further away dwarf galaxies, and ultra-faint galaxies are currently impossible to detect outside the Milky Ways virial radius. This makes it difficult to separate a real difference between local and distant dwarf galaxies from the observational bias that different objects can be observed to different distances. Comprehensive reviews of Local Group dwarf galaxies are given by Mateo (1998), and Tolstoy et al. (2009).

1.5.4 Formation Scenarios

Defining as dwarf galaxies all galaxies fainter than $M_V = -18$, or stellar masses below $\sim 10^9 M_\odot$, the realm of dwarf galaxies spans at least seven orders of magnitude in stellar mass, more than all other galaxies combined. While most of the stellar mass in the universe today resides in galaxies with stellar masses of $\sim 5 \times 10^{10} M_\odot$ (Kauffmann, 2003), it is clear that understanding dwarf galaxy formation is an important part of understanding galaxy formation as a whole. With such a range in masses, a large variation in morphology, gas content, star formation rate and star formation history is perhaps not surprising. It can be used to define several sub-categories: dwarf elliptical (dE), dwarf spheroidal (dSph) and ultra-faint (UF) dwarf galaxies; dwarf irregulars (dI); blue compact (BCD) and ultra compact (UCD) dwarf galaxies, as well as various so-called "transition type" objects.

It is not yet known, however, if different types of dwarf galaxies are truly distinct from birth, or whether one can be transformed into another, either by means of internal effects, or by environment. The relative importance of internal effects, such as supernova feedback, or external effects, such as ram-pressure stripping and tidal stripping, will be investigated in Chapter 4. It is also still a question of debate whether "transition type" dwarf galaxies indicate a transition from dwarf-irregular to dwarf-elliptical, or whether they are simply in the region of parameter space between the two classes. While dwarf elliptical and dwarf irregular galaxies appear to be primordial objects, which contain at least a fraction of very old stars; blue compact dwarf galaxies may be younger objects, suggesting an entirely different formation mechanism.

1.5.5 Evidence for Environmental Effects

Many observable properties of galaxies correlate with environment. Early type galaxies tend to be more strongly clustered (Davis & Geller, 1976), and within clusters, the fraction of early type galaxies increases with density. In galaxy clusters, the morphology-density relation also extends to dwarf galaxies; dwarf ellipticals are typically found closer to the cluster centre, while dwarf irregular galaxies are found further out.

For the Local Group environment, the situation is somewhat less clear. Figure 1.2, adopted from Grebel et al. (2003), shows the HI mass in dwarf galaxies of the Local Group, as a function of distance to M31 or the Milky Way. There is a trend for more distant galaxies to have higher gas content, although there are several exceptions. A similar trend, for a larger volume, is reported by Geha et al. (2006), as shown in the left panel of Figure 1.3. The gas fraction of dwarf galaxies of similar mass is plotted as a function of distance to their nearest luminous
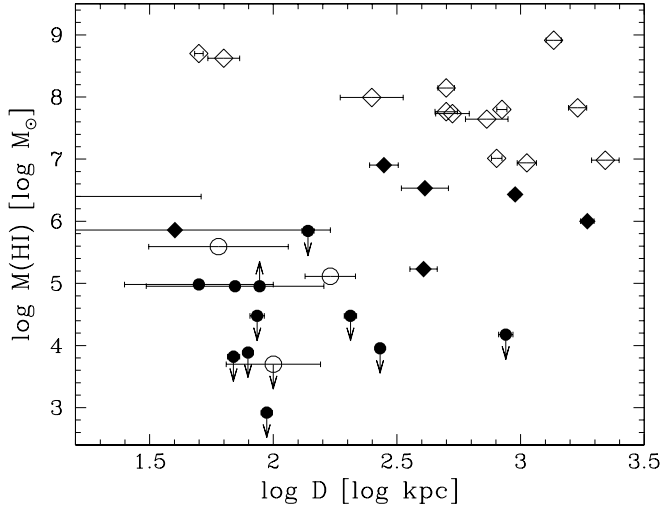
Figure 1.2: HI mass as a function of distance to the nearest massive galaxy, taken from Grebel et al. (2003). Dwarf irregular galaxies are shown as open diamonds, dwarf elliptical and dwarf spheroidal galaxies are shown as open and filled circles, respectively. Filled diamonds stand for so-called transition type galaxies, indistinguishable from dwarf spheroidals except for their gas content. Arrows indicate upper and lower limits.
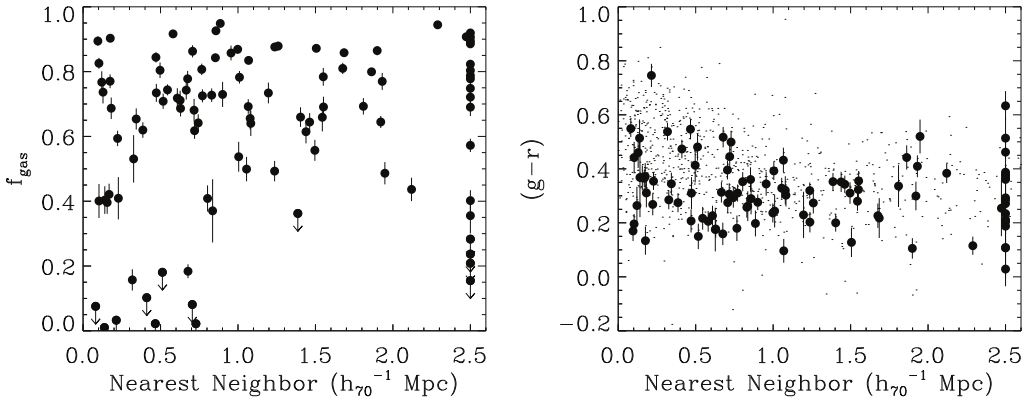
Figure 1.3: Gas fraction (left) and $g - r$ colour (right) of low mass SDSS galaxies with stellar masses in the range of $2 \times 10^7 - 3 \times 10^8 M_\odot$, plotted against distance to the nearest luminous neighbour. The figure is adopted from Geha et al. (2006).
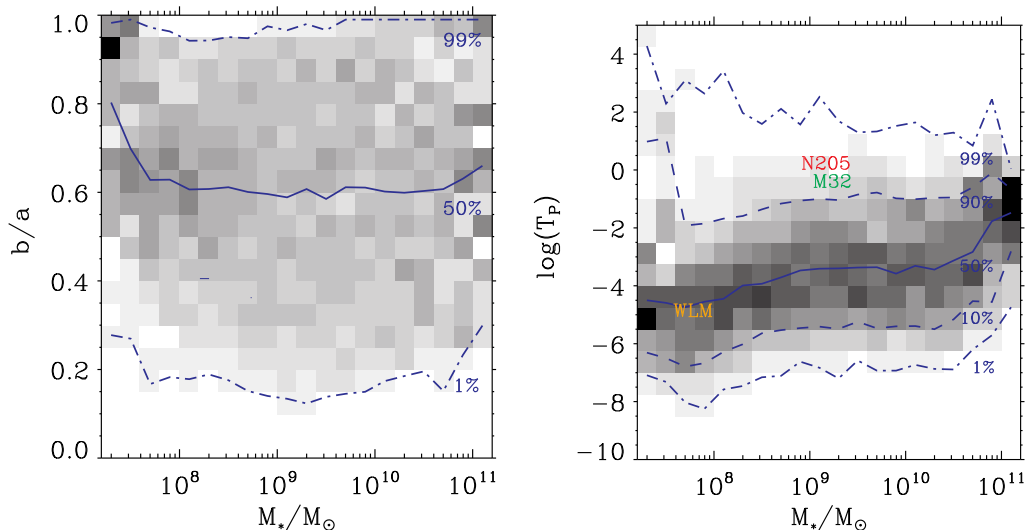
Figure 1.4: Probability distributions of apparent axis ratio (left panel) and tidal parameter (right panel), in bins of stellar mass for galaxies from a local SDSS sample adopted from Sánchez-Janssen et al. (2010). The percentages next to the blue contour lines denote the fraction of all galaxies below the corresponding axis ratio or tidal parameter within each mass bin. The right panel includes three examples of satellites in interaction with M31. It is evident that strongly perturbed systems like M32 are rather rare, and most dwarf galaxies have $T_p < 1$. The mean tidal parameter also decreases with decreasing stellar mass.

neighbour. Gas-poor galaxies are found predominantly as companions to other galaxies. The right panel shows the $g - r$ colour for the same set of galaxies, which can be a proxy for age; redder colours (higher $g - r$) indicate older stellar populations. The absence of a noticeable trend with distance may indicate that the environment has at most a weak effect on star formation.

The left panel of Figure 1.4, adopted from Sánchez-Janssen et al. (2010), shows the distribution of projected axis ratios, a measurement of the flattening of galaxies as a function of stellar mass, in a volume-limited sample across different environments. At stellar masses below $10^8 M_\odot$, galaxies appear to be significantly flattened. The right panel of Figure 1.4 shows the distribution of the tidal parameter for the same sample of galaxies, defined as the maximum ratio of external to internal forces acting on a galaxy. Sánchez-Janssen et al. conclude that low-mass galaxies tend to be less strongly affected by tidal forces, and that the morphological trend of increasing thickness found in fainter galaxies, is related

to the increasing importance of feedback mechanisms, rather than environmental effects.

In Chapter 3, I show that internal effects would be sufficient to explain the properties of dwarf spheroidals in the current astrophysical and cosmological model. In Chapter 4, I show that in a simulation where the environment is included, internal effects and the total mass of an object would still be the most important drivers of dwarf galaxy formation, but that there are also differences between the satellites and isolated dwarf galaxies, particularly regarding their gas content, and particularly in an intermediate mass regime.

A definitive proof or falsification of this scenario, would be the discovery of truly isolated dwarf spheroidals, or the exclusion thereof. In the Local Group, four dwarf spheroidals have been discovered that appear to be isolated from both the Milky Way and M31, and explored spectroscopically (e.g. Gallart et al., 2001; Lewis et al., 2007; Fraternali et al., 2009). Two of these, Antila and Phoenix, have HI gas in their vicinity, while Cetus and Tucana appear no different from other dwarf spheroidals (Monelli et al., 2010). However, it is not known with certainty whether these four objects have always been isolated in the past.

1.5.6 Dwarf Galaxies as Building Blocks?

From a theoretical perspective, the end point of dwarf galaxy evolution may be just as important as the starting point: As noted Section 1.3, in the hierarchical picture, some small objects merge to form larger objects. Dwarf galaxies with old stellar populations were once thought of as the surviving "building blocks", that had merged to create objects like the Milky Way. While tidal streams provide clear evidence of ongoing mergers of dwarf galaxies onto larger galaxies, it is also clear now that the dwarf galaxies we observe today have evolved considerably since the formation of the Milky Way. When no stars of lower metallicities were found in dwarf galaxies compared to the halo stars, this was interpreted as evidence that the Milky Way had in fact formed first, pre-enriching the intergalactic medium from which the dwarf galaxies were formed. This top-down formation would have been hard to reconcile with the order of collapse of structures in ΛCDM. Very recently, however, extremely metal-poor stars were discovered in several dwarf spheroidals (e.g. Tafelmeyer et al., 2010), in line with interpreting dwarf galaxies as primordial objects. Still, we should perhaps not think of present dwarf galaxies directly as the building blocks of bigger galaxies, but that the building blocks of the Milky Way, and the dwarf galaxies we see today, have common ancestors.

2 | Chapter 2
Methods

Numerical Simulations

In this chapter, I will describe the methods used in the simulations of galaxy formation. The fact that a theory, based on the simple assumptions presented in Sections 1.3.1 to 1.3.3 of the previous chapter, can be used to make accurate predictions for the distribution of structures in the universe, suggests that, on the whole, it captures the most important effects. Still, these analytic models have a number of shortcomings: we have assumed isotropic, spherical collapse and the absence of shear, which can arise due to asphericity of the halo and its anisotropic environment. The universal application of Birkhoff's theorem also amounts to the "Jeans swindle": haloes do not evolve in a uniform background. In reality, the background itself is collapsing and breaking up into haloes at the same time, leading to tidal effects. Furthermore, it was always assumed that matter is collisionless. After matter-radiation equality, this is justified on large scales, but it is no longer valid on scales relevant to galaxy formation. While some of these effects such as ellipsoidal collapse can be incorporated in more complicated analytic methods (e.g. Sahni & Coles, 1995), an alternative, and in some sense, much simpler way to describe the highly non-linear evolution is a direct, numerical solution to the equations of motion.

Section 2.1 describes the generation of initial conditions, which can be seen as the transition point from an analytical treatment of the linear regime, to a numerical solution when the linear assumptions no longer apply. Section 2.2 describes the basic numerical methods for solving the N-Body problem with gravity and hydrodynamics used in the computational code GADGET-3 of Springel et al. (2001), which is used for all simulations presented in Chapters 3 to 5. Details of the particular models used are also found in the relevant methods sections of these chapters. The *semi-analytical* method, which combines a direct computation of the growth of structure, and an analytical description of galaxy formation, is briefly discussed in Chapter 6.

2.1 Initial Conditions

Even though perturbation theories eventually break down, they are extremely useful for constructing initial conditions for numerical simulations. They can bridge the gap between the very uniform early universe until a time when the perturbations are still linear.

In cosmological simulations, periodic boundary conditions are usually adopted. This implies that the mean density of the simulation volume is equal to the mean density of the universe. It allows the representation of the initial Gaussian density field as a discrete summation of plane waves, with the minimum frequency determined by the box size, and the maximum (Nyquist) frequency corresponding to the interparticle spacing. The box size must also be chosen large enough, so that objects are not subject to their own tidal forces.

For a given density field ρ represented by a finite number of point particles at locations $\mathbf{x}$ in a volume V, perturbations $\delta(\mathbf{x})$ can be generated from a power spectrum of initial perturbations $\delta_{\mathbf{k}}$ by the discrete Fourier transform:

$$\delta(\mathbf{x}) = \frac{1}{V} \sum \delta_{\mathbf{k}} e^{i\mathbf{k}\cdot\mathbf{x}} \tag{2.1}$$

The particle-mesh algorithm of GADGET-3, described in Section 2.2.1, can be used to create the real-space representation. The perturbations are applied to a uniform particle distribution, that can be either a regular cubic grid, used in the initial conditions for Chapter 3, or so-called "glass" (White, 1994), used in Chapters 4 and 5. They also find application in zoom simulations, which are the basis of all the numerical results presented in Chapters 3 to 5. Here, small scale power, not present in the original simulation, can be added, when the particle resolution is refined in a cubical sub-region of the original volume. In addition, the large scale power no longer representable in the small high resolution region is applied using the displacement field of the original box.

As described in Section 1.3.3, the initial displacements are evolved forward using a Lagrangian perturbation approach. The simulations in Chapters 3 and 4 are obtained using the Zel'dovich approximation, while those in Chapter 5 are constructed using second-order Lagrangian perturbation theory.

The haloes of individual dwarf galaxies in Chapter 5 reach final masses of $\sim 10^{10} M_{\odot}$, which corresponds to $\sim 0.00001\%$ of the total mass in the parent Millennium-II simulation. Clearly, zoom simulations were required, which sample only a very small sub-volume of the original simulation, albeit at a much higher resolution, and most of the volume is sampled with much coarser resolution. The mass refinement method has been used in several previous simulations, (e.g. by Katz & White, 1993; Evrard et al., 1994; Moore et al., 1998).

There are many thousands of similar mass objects in the total simulation volume. However, in order to construct initial conditions, two requirements have to be met:

- The Lagrangian volume corresponding to the region of interest must have been compact and connected already at high redshift, so that the high resolution volume can be limited, while at the same time, no massive "boundary" particles cross the high resolution region.

- The particles within the Lagrangian region at early time must remain inside, so that high resolution particles do not escape to the low resolution region, which would slow down the simulation.

The selection of suitable candidates for resimulations of dwarf galaxies from the Millennium-II simulation is illustrated in Figure 2.1. Initially, 20,000 groups were considered in the mass range of 0.9 to 1.0 $\times 10^{10} h^{-1} \mathrm{M}_\odot$, corresponding to ~ 1400 particles, which were identified using the group information. These particles were traced back to the initial condition files, and only those groups where all particles were contained within a volume of 0.5^3 kpc^3 were kept. Of the remaining 128 groups, the Lagrangian volume was extended to twice the maximum extension of the FoF-group at $z = 0$, and all particles ($\sim 1600 - 2500$) within this larger volume were traced back to the initial condition, and subject to the same constraint. In total, 27 groups, or $\sim 0.14\%$, satisfied the selection criteria. A possible selection bias was investigated, by comparison of the mass accretion histories to the ensemble of similar mass haloes, as described in Chapter 5, and also by comparison of the predictions of semi-analytical models, as described in Chapter 6. Because the group information was not available in the initial conditions (and a Friends-of-Friends algorithm would not have worked), the search for compact groups had to work on the particle level, and carried out in a parallelised fashion. The method of assigning particle IDs according to their position on a space-filling Peano-Hilbert curve, described in Springel (2005), which allows for a direct computation of the initial location, would substantially reduce the computational cost of this process. It has not been used in the Millennium-II simulation, but is recommended for future cosmological simulations where zoom simulations are a possible follow-up.

The refinement is performed at $z = 127$, the initial time of the Millennium-II simulation. The initial conditions are then evolved, using second order Lagrangian perturbation theory, up to $z = 40$, when the numerical simulations begin. Of the 27 suitable candidates, the representative sample of six objects was selected based on their merger histories (described in Section 5.3), and also a comparison to predictions by a semi-analytical model (discussed in Chapter 6). The final result, and the excellent agreement between the zoom simulation and the parent simulation, are illustrated in Figure 2.2.
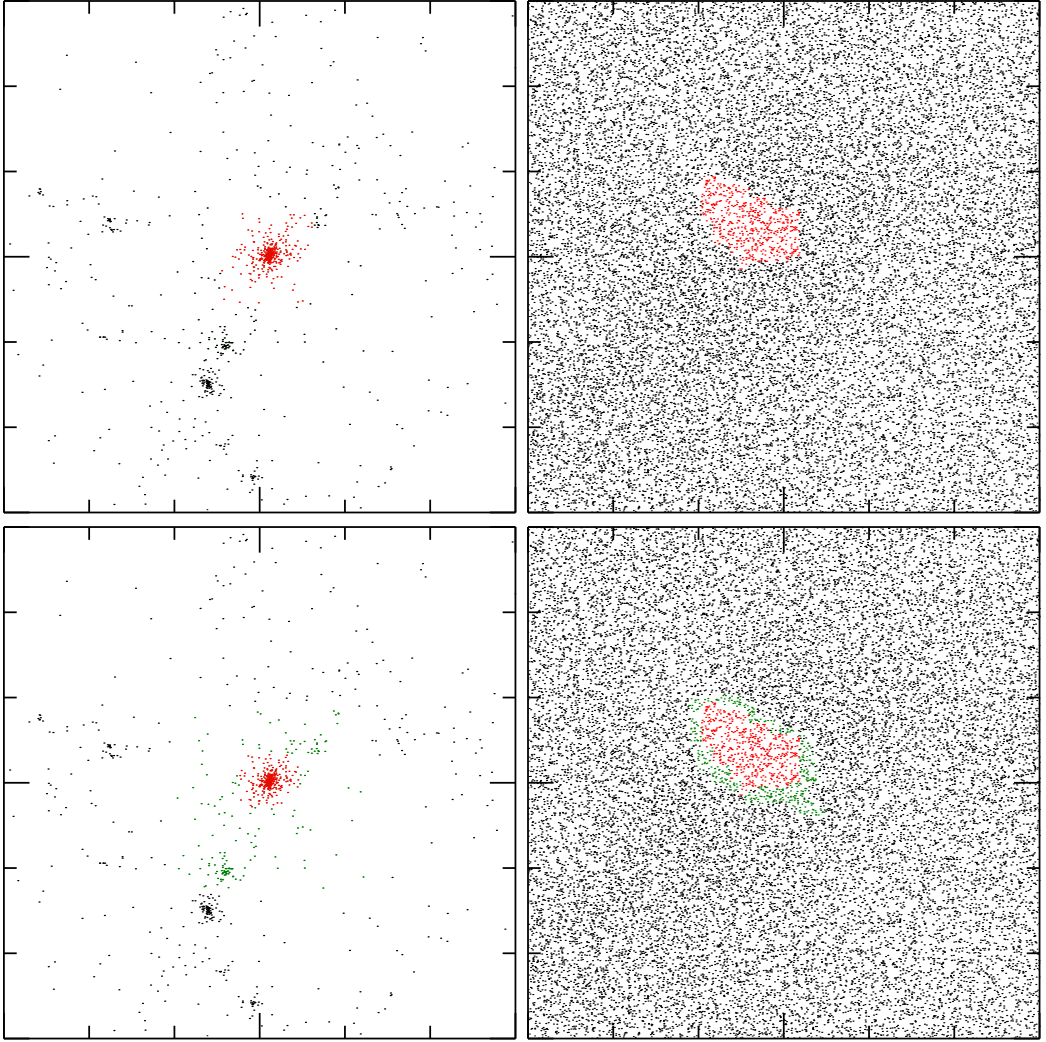
Figure 2.1: Schematic illustration of the selection of candidates for resimulation, using the example of Halo 4 of Chapter 5. Top row, left to right: (1) The particles in a suitable mass halo (in red) are identified at $z = 0$ in the parent simulation, using the Friends-of-Friends catalogue. (2) The particles are traced back to the initial conditions at $z = 127$. Bottom row, left to right: (3) If the group particles are found to be in a compact and connected region, the search radius is expanded to $2 \times r_{max}$ at $z = 0$ (in green). (4) The halo is accepted as a candidate if all particles within the extended radius also form a compact Lagrangian volume in the initial conditions.
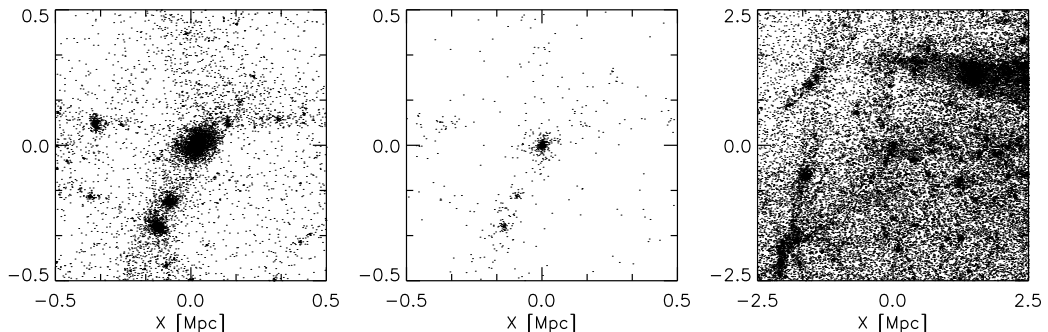
Figure 2.2: Comparison of Halo 4 from Chapter 5 at $z = 0$, in a pure dark matter resimulation, and in the parent Millennium-II simulation. The left panel shows the position of 0.5% of the particles in a box of sidelength 1 Mpc in the resimulation, while the central panel shows the position of all particles within the same region in the MS-II, identical to Figure 2.1. The panel on the right shows all particles in a box of 5 Mpc in the MS-II, with Halo 4 in the centre. All three panels are centred on the same absolute coordinates for the parent box of sidelength 137 Mpc. The FoF mass of the halo agrees to within less than 1%. A comparison of the left and the central panel reveals the additional substructure resolved in the resimulation.

The zoom initial conditions for Chapter 3 are further rescaled at constant density, up to a factor of two in length. This is permissible, since at these low mass scales, perturbations reach the horizon while the universe is still dominated by radiation, and therefore do not grow further until matter-radiation equality. This results in a flattening of the Harrison-Zel'dovich power spectrum at a scale of $k \sim 0.03 \ h$ Mpc^{-1}, the size of the horizon at matter-radiation equality, and a transition to $P(k) \propto k^{-3}$. As a result, collapse on very small scales is essentially co-temporal.

2.1.1 Addition of Gas

All simulations presented here are hydrodynamical simulations, based on cosmological dark matter only simulations. Gas particles are introduced to the initial conditions by splitting each high-resolution dark matter particle at a mass ratio of Ω_{DM} to Ω_b. The gas particles inherit the specific momentum of the dark matter particles, and are displaced by half of the local mean interparticle separation, with the positions adjusted to conserve the centre of mass. This assumes that at the beginning of the simulation, there is no bias between the dark matter and the gas particles. The initial temperature of gas particles is set according to the CMB temperature, which evolves as $T \propto 1/(1 + z)$.

2.2 Numerical Integration

All simulations presented in Chapters 3 through 5 have been performed using the N-Body–SPH code GADGET-3 of Volker Springel (Springel et al., 2001; Springel, 2005). The N-Body method describes a class of numerical integration schemes, in which physical components such as gas, dark matter and stars are represented by a finite number of particles, whose trajectories are evolved in time. The two principal force components that determine the dynamics of cosmological simulations are the gravitational and the hydrodynamical interactions, described briefly in the following two sections.

2.2.1 Gravity

In GADGET-3, gravitational interactions are solved using a combination of a direct summation of forces between particles by way of a tree code, as well as a mesh-based approach for long range forces. Conceptually, this combination is similar to the particle-particle–particle-mesh (P^3M) algorithm (Hockney et al., 1973; Eastwood et al., 1980), with the PP part replaced by a tree code (TreePM).

In general, the acceleration of particle i, located at position $\mathbf{r}_i$, due to all other particles of mass m_k and position $\mathbf{r}_k$ is given by:

$$\ddot{\mathbf{r}}_i = G \sum_{k \neq i} \frac{m_k(\mathbf{r}_k - \mathbf{r}_i)}{|\mathbf{r}_k - \mathbf{r}_i|^3} \qquad (2.2)$$

The direct summation of forces is conceptually the simplest, and the most accurate method. At each timestep, the forces exerted on each particle by every other particle are computed directly. Because the computational complexity of the direct force computations scales as $O(N^2)$ with the number of particles, this cannot be used for large N. Instead, a hierarchical tree algorithm (Barnes & Hut, 1986) is used, which subdivides the simulation volume in a recursive fashion, until the smallest nodes (called tree-leafs) contain only one particle. Interactions on each particle due to a set of particles at larger distances are then grouped into single interactions of progressively larger sets of particles at their centre of mass, using the pre-calculated node structure. The accuracy of the individual force calculations depends on the opening parameter (which defines the relation of maximal group-size to distance), and on the order of a possible multipole expansion using sub-nodes about the centre of mass of each group. The choice of these parameters reflects a compromise between the accuracy in each interaction, and the computational cost per particle, which has to be weighed against the benefit of a higher mass and time-resolution. In practise, the tree algorithm reduces the required number of force calculations from $O(N^2)$ to $O(NlogN)$ for each full timestep.

In addition, long-range interactions are computed using a Fourier particle mesh (PM) method. The simulation volume is subdivided into a grid of Cartesian mesh cells, and at each timestep, a smoothed mass distribution is used to define the density in each cell. The mesh is then Fourier-transformed to compute the gravitational potential after a convolution of the source function with the Green's function of the periodic boundaries, and truncating at small scales corresponding to the short-range term computed separately with the tree algorithm. After an inverse transform, the gravitational field is then computed as a finite difference of the potential on the mesh in real space, and the (interpolated) forces are applied to the particles at their positions, using the same kernel that was used in the mass distribution estimate.

In cosmological simulations of galaxy formation, the simulated volume can be much greater (e.g. of side length (100 Mpc/h) than the region of interest (e.g. 2 Mpc/h). The particle representation (also see Section 2.1) is therefore also ordered hierarchically, in order to combine a high resolution for astrophysical processes in the region of interest, whilst still capturing the external field effects of the large scale structure at much greater distances. A similar hierarchy applies to the PM-part in GADGET-3, where a second, finer mesh is used to cover a pre-defined high-resolution region.

2.2.2 Hydrodynamics

Gas does not only interact gravitationally, but also hydrodynamically depending on quantities such as pressure and viscosity. For example, taking into account only gravitational acceleration and pressure, the momentum equation for particle i can be written as:

$$\frac{d\mathbf{v}_i}{dt} = \ddot{\mathbf{r}}_i|_G - \frac{\nabla P_i}{\rho_i} \qquad (2.3)$$

where on the right-hand side, the first term is the acceleration due to gravity as given by Equation 2.2, and the second term is the pressure gradient at the location of the particle, divided by the mass density. This formalism requires that the pressure is a differentiable function at every point $\mathbf{r_i}$, and that the density is at least defined and non-zero. However, in the N-particle approach, continuous quantities such as pressure and density are not naturally defined. In order to apply the continuous hydrodynamic equations, they have to be put in a form that can be applied to a set of discrete points. One possible technique, used in GADGET, is known as Smoothed Particle Hydrodynamics (SPH); an interpolation (smoothing) over neighbouring particles (Monaghan, 1992). I will only sketch the basic ideas, following Monaghan (1992) and Monaghan (2001).

For a general function or field $A(\mathbf{r})$, the integral interpolant $A_I(\mathbf{r})$ at a point $\mathbf{r}$ in space is given by the integral over all space:

$$A_I(\mathbf{r}) = \int A(\mathbf{r}')W(\mathbf{r} - \mathbf{r}', h)\,\mathrm{d}V \tag{2.4}$$

This formalism allows a definition of fields such as $\rho(\mathbf{r})$ or the pressure $P(\mathbf{r})$ at every point $\mathbf{r}$. The kernel function W describes the contribution of the quantities at points $\mathbf{r}'$ relative to their distance $\mathbf{r} - \mathbf{r}'$, and dependent on the smoothing length h. Normalisation requires that:

$$\int W(\mathbf{r} - \mathbf{r}', h)\,\mathrm{d}V = 1$$

In the limit of an infinitesimal smoothing length, $\lim_{h \to 0} W(\mathbf{r} - \mathbf{r}', h) = \delta(\mathbf{r} - \mathbf{r}')$, which is non-zero only for $\mathbf{r} = \mathbf{r}'$, so that $A_I(\mathbf{r})$ is identical to $A(\mathbf{r})$, but only defined at $\mathbf{r}$. In general, h is chosen so that a finite number of particles (e.g. 32) is included within a sphere of radius h; large enough to ensure a stable definition of quantities, and as small as possible to achieve a high spatial resolution. In the case of a finite number of particles, the integral in Equation 2.4 is replaced by a summation:

$$A_I(\mathbf{r}) = \sum_i m_i \frac{A(\mathbf{r_i})}{\rho_i} W(\mathbf{r} - \mathbf{r_i}, h) \tag{2.5}$$

where the contribution of particle i at position $\mathbf{r}_i$ to the quantity at position $\mathbf{r}$ has been weighted according to its contribution to the local density, m_i/ρ_i.

In this way, any field A defined at discrete locations can be transformed into a differentiable field A_I, as long as the kernel W is differentiable at every point. For a physical interpretation of *smoothing*, a Gaussian kernel is the most natural choice, but spline kernels with a fixed limit are typically used in numerical applications. In GADGET, the kernel takes the following form, after Monaghan & Lattanzio (1985):

$$W(r, h) = \frac{8}{\pi h^3} \begin{cases} 1 - 6v^2 + 6v^3, & 0 \le v \le \frac{1}{2}; \\ 2\left(1 - v\right)^3, & \frac{1}{2} \le v \le 1; \\ 0, & v > 1 \end{cases}$$

where $v \equiv r/(2h)$, h being the smoothing length, and r the distance between $\mathbf{r}$ and $\mathbf{r_i}$. In particular, in the case that $r > 2h$, i.e. for particles separated by more than twice the smoothing length, the contribution of W to Equation 2.5 is zero. This greatly reduces the computational cost, and is justified by the fact that only neighbouring particles exchange hydrodynamic forces. However, it also makes the smoothing length an important parameter in determining the accuracy and the speed of the calculations.

In situations with high density contrasts, the best compromise can be achieved when the smoothing length is not static, but changes with the local density. This approach is known as *adaptive* Smoothed Particle Hydrodynamics, and is used in GADGET.

Provided that Equation 2.5 is differentiable, and noting that $A(\mathbf{r_i})$ is simply a scalar at every location $\mathbf{r_i}$, one can write:

$$\nabla A_I(\mathbf{r}) = \sum_i m_i \frac{A(\mathbf{r_i})}{\rho_i} \nabla W(\mathbf{r} - \mathbf{r_i}, h) \tag{2.6}$$

Using the identity $\nabla(u/v) = (v\nabla u - u\nabla v) \cdot v^{-2}$, the pressure term in Equation 2.3 can be expressed as:

$$\frac{\nabla P_i}{\rho_i} = \nabla \left(\frac{P_i}{\rho_i} \right) + \frac{P_i}{\rho_i^2} \nabla \rho_i$$

Now, substituting in Equation 2.3 with the interpolated form of the derivatives from Equation 2.6, the Euler equation for the motion of the particle i is obtained in the appropriate form:

$$\frac{d\mathbf{v}_i}{dt} = -\sum_j m_j \left(\frac{P_j}{\rho_j^2} + \frac{P_i}{\rho_i^2} \right) \nabla W(\mathbf{r}_i - \mathbf{r}_j) + \ddot{\mathbf{r}}_i|_G \tag{2.7}$$

Here, the sum is over all particles $j \neq i$, which in practise reduces to the particles in the neighbourhood of i for which the kernel is non-zero, and as before, $\ddot{\mathbf{r}}_i|_G$ labels the acceleration due to gravity.

Similar substitutions are applied to the continuity equation, the thermal energy equation, and equations for viscosity and thermal conduction. As explained in Section 3.2.3, the multiphase-model of Scannapieco et al. (2006) explicitly decouples the hot and cold components of the ISM by considering as neighbours in the kernel only those particles with similar thermodynamic properties.

2.2.3 Resolution

The particle mass and mean separation determine the resolution of the simulation. To prevent spurious two-body interactions by particles, which have no physical meaning, the gravitational potential is *softened*, by replacing the divergent $1/r^2$ dependence with $1/(r^2 + \epsilon^2)$, where ϵ is the gravitational softening scale (Aarseth, 1963).

The choice of ϵ is somewhat arbitrary. Power et al. (2003) equate the maximum acceleration of a particle of mass m by close encounters with another particle in a softened potential, $a \sim Gm/\epsilon^2$, to the minimum mean field acceleration due to the potential of a halo of mass $M_{200} = mN_{200}$, at its virial radius r_{200}. This sets a lower limit of $\epsilon_{acc} = r_{200}/\sqrt{N_{200}}$ to ensure that accelerations due to the discreteness of the particle distribution always remain small.

Within each simulation, we use the same softening for all particles in the high resolution region, and separate values for the more massive dark matter particles tracing the large scale evolution. In addition, in the simulations presented in Chapters 3 and 5, we use two softening regimes, first fixing the softening scale in comoving coordinates, and later in physical coordinates, after the objects of interest have collapsed and decoupled from the universal expansion. We also tested the effect of different softening scales, to ensure that our choice is in a regime where the results are not sensitive to the softening parameter.

In Figure 2.3, the mass profile of three resimulated haloes (described in Chapter 5) is shown. In the upper panel, the thick line corresponds to an NFW-fit (Navarro et al., 1996) to each halo, which takes the form

$$\rho(r) = \rho(r_s)\frac{4r_s^3}{r(r + r_s)^2} \tag{2.8}$$

where r_s is a characteristic scale radius of each halo, with the limiting case $\rho \rightarrow r^{-1}$ as $r \rightarrow 0$. The dotted line denotes the softening scale that is used in the simulation. In the lower panel, the ratio of the NFW fit to the actual profile is also shown. It can be seen that the NFW profile is a good match to each halo down to the softening scale. Also noticeable is the flattening of each profile in the central region, attributable to the softening. Note that the centre is not the centre of mass of the halo, but the region of highest density, found using the method of shrinking spheres.

In hydrodynamics, the size of the smoothing kernel also sets a limit on the spatial resolution. By decoupling neighbouring particles with very different entropic functions, the multi-phase model of Scannapieco et al. (2005, 2006) effectively sacrifices some spatial resolution compared to a model where all gas particles contribute to the kernel. If very few particles are present, this can potentially cause problems. In the simulations presented in Chapter 3, where galaxies completely lose their gas, this cannot be avoided, but only affects the last stage of the gas ejection, when star formation has already ceased. On the other hand, the dwarf galaxies presented in Chapter 4 are sampled with much fewer particles, which may put them in a regime where the gas removal is affected by resolution.
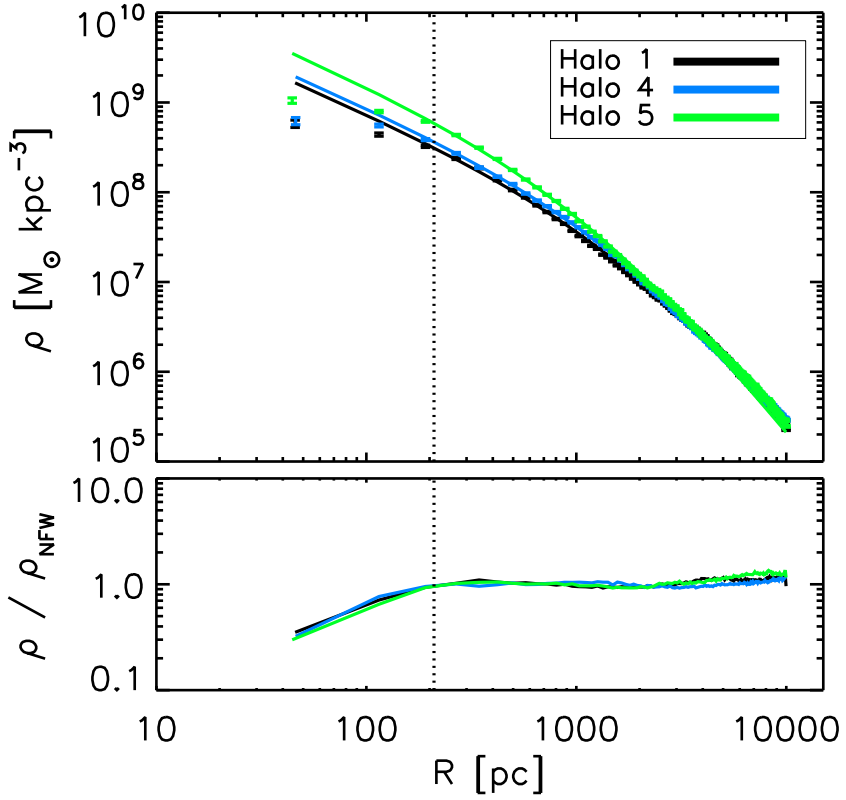
Figure 2.3: Density profile of three resimulated haloes in pure dark matter simulations (see Chapter5), fitted with NFW-profiles. The dotted line denotes the gravitational softening length ϵ. The bottom panel indicates the ratio of the density to the NFW profile. While the NFW profile provides a good match down to the softening scale, the softening of the potential establishes an effective "core" in the centre.

3

Chapter 3

The Formation of Dwarf Spheroidal Galaxies in Isolation

We present results of high resolution hydrodynamical simulations of the formation and evolution of dwarf galaxies. Our simulations start from cosmological initial conditions at high redshift. They include metal-dependent cooling, star formation, feedback from type II and type Ia supernovae and UV background radiation, with physical recipes identical to those applied in a previous study of Milky Way type galaxies. We find that a combination of feedback and the cosmic UV background results in the formation of galaxies with properties similar to the Local Group dwarf spheroidals, and that their effect is strongly moderated by the depth of the gravitational potential. Taking this into account, our models naturally reproduce the observed luminosities and metallicities. The final objects have halo masses between 2.3×10^8 and 1.1×10^9 $M_\odot$, mean velocity dispersions between 6.5 and 9.7 kms^{-1}, stellar masses ranging from 5×10^5 to 1.2×10^7 $M_\odot$, median metallicities between [Fe/H] $= -1.8$ and -1.1, and half-light radii of the order of 200 to 300 pc, all comparable with Local Group dwarf spheroidals. Our simulations also indicate that the dwarf spheroidal galaxies observed today lie near a halo mass threshold around 10^9 $M_\odot$, in agreement with stellar kinematic data, where supernova feedback not only suffices to completely expel the interstellar medium and leave the residual gas-free, but where the combination of feedback, UV radiation and self-shielding establishes a dichotomy of age distributions similar to that observed in the Milky Way and M31 satellites.

3.1 Introduction

Dwarf spheroidal galaxies are amongst the smallest and faintest known galactic systems, and at first sight, should be easy to understand. Their name indicates a simple morphology, they possess low rotation, little or no interstellar gas and no active star formation. Their stellar masses range from less than 10^4 to a few times $10^7 M_\odot$, which even at the more luminous end, makes them comparable to the brightest globular clusters. However, whilst all observed dwarf spheroidal galaxies contain at least a fraction of very old stars (Grebel, 1997), this is where the similarities with globular clusters end. Spectroscopic surveys of individual stars in several dwarf spheroidal galaxies of the Local Group (e.g. Battaglia et al., 2006) have revealed surprisingly complex star formation histories, sometimes over several Gyrs, and at least in one case in multiple bursts (Koch et al., 2006a, 2008; Orban et al., 2008)

About two dozen dwarf spheroidal galaxies have so far been discovered as satellites of the Milky Way, while estimates using luminosity functions corrected for completeness and bias predict the total number of faint satellites to be an order of magnitude higher (Tollerud et al., 2008). The known dwarf spheroidal galaxies in the Local Group reside in a variety of environments. There are a few near both M31 and the Milky Way, with distances of ~ 30 kpc and clearly within their hosts' dark matter haloes, as well as some remote objects like Cetus (Lewis et al., 2007) and Tucana (Castellani et al., 1996; Fraternali et al., 2009), which can be considered to have evolved in isolation.

It has been proposed for a long time (e.g. Faber & Lin, 1983) and is now widely believed that the luminous component of dwarf spheroidal galaxies is not all there is to them. Their dynamics appear to be largely dark matter dominated, and measurements of stellar velocity dispersions (e.g. Koch et al., 2007; Walker et al., 2007; Mateo et al., 2008; Walker et al., 2009) indicate that they possess the highest mass-to-light ratios of any known galactic systems. Recent studies further suggest that despite the spread in luminosities, the total mass within the central 300 pc of each galaxy lies within a small range of around $10^7 M_\odot$ (Strigari et al., 2008).

It is also worth pointing out that in galaxy formation, small size can breed complexity. Shallow potential wells make these systems susceptible to both internal and external effects, such as violent supernova feedback, photoionization and heating from the cosmic UV background, tidal interactions and ram-pressure stripping. All of these processes have the potential to shape the evolution of dwarf galaxies, and to leave their mark on the star formation history and the chemical abundances, as well as on the morphology and dynamics of the final objects. They may explain some of the peculiar properties of dwarf spheroidals, including their very high mass-to-light ratios, and may also be responsible for the observed scaling

laws (e.g. Woo et al., 2008). In this sense, the evolution of dwarf spheroidal galaxies can be considered an extreme case, but at the same time, an extremely good laboratory for astrophysical and cosmological processes (Marlowe et al., 1995). While the sensitivity to many parameters represents a considerable challenge for simulations, the large number of dwarf galaxies in the Local Group, together with the availability of high quality observational data also provides an unusually high number of constraints. Revaz et al. (2009 in prep.) exploit this fact by studying a large number of idealised models with non-cosmological initial conditions, which they can tune to reproduce the observed relations.

The number of dwarf galaxies observed in the Local Group continues to grow as new, 'ultra-faint' satellite galaxies are discovered (e.g. Martin et al., 2006; Chapman et al., 2007). Nevertheless, it is still much smaller than the total number of dark matter subhaloes found in high-resolution simulations of spiral galaxy haloes in the standard ΛCDM cosmology (e.g. Klypin et al., 1999; Moore et al., 1999; Diemand et al., 2007; Springel et al., 2008). This has become known as the 'missing satellites problem'. However, this is only an apparent discrepancy. It is removed when one accounts for the fact that not all subhaloes contain stars. Two possible mechanisms that can produce a number of visible satellite galaxies similar to that observed are the following. Perhaps many haloes were able to form a few stars initially, but the baryonic components of all haloes below some critical mass were subsequently destroyed by supernova feedback (e.g. Dekel & Silk, 1986; Ferrara & Tolstoy, 2000). Alternatively (or perhaps additionally) photoionization may have prevented star formation in the smallest haloes (e.g. Efstathiou, 1992; Somerville, 2002; Simon & Geha, 2007). As dwarf spheroidals are the faintest known galaxies, a detailed understanding of their evolution should eventually reveal the influences of these two effects.

Examples of earlier numerical studies of the formation of dwarf galaxies include simulations by Read et al. (2006), Mashchenko et al. (2008), Stinson et al. (2007, 2009) and Valcke et al. (2008). The latter two have investigated the collapse of gas clouds in dark matter haloes of constant mass. Both find evidence of prolonged and self-regulated star formation. However, while they do observe significant supernova-driven outflows, at a halo mass of $10^9 \mathrm{M}_\odot$, Stinson et al. find better agreement with dwarf irregular galaxies. Read et al. performed simulations of the formation of the first baryonic building blocks in a cosmological volume at high redshift. They confirm the importance of supernova feedback and UV heating (assumed to begin at $z = 13$) for removing the gas from the smallest haloes. However, they do not follow the evolution of the surviving objects to the present day, terminating their simulations at $z = 10$. Mashchenko et al. have also performed cosmological simulations, albeit of noticeably more massive haloes, which they follow up to $z = 5$. They do not include UV radiation, and would

require an additional mechanism to remove the gas from the galaxy, in order to form a system comparable to observed dwarf spheroidals. However, they find stellar properties in good agreement with the Fornax dwarf spheroidal, including globular clusters. They also predict that supernova feedback induces the formation of extended dark matter cores via gravitational resonance heating.

In this work, we model the formation and evolution of dwarf galaxies in fully cosmological, smoothed particle hydrodynamical (SPH) simulations. We simulate a cosmological volume with periodic boundary conditions, in which the haloes grow from small density perturbations imposed at high redshift. Our initial conditions are chosen to reproduce galaxies of halo masses similar to the ones inferred for the Local Group dwarf spheroidals. Because we follow the evolution to $z = 0$, and because we include the environment in a consistent way, our mass-resolution is somewhat lower compared with simulations of isolated haloes, or simulations which end at high redshift. However, the cosmological nature of our simulation allows us to simultaneously follow the growth of the dark matter halo, and the evolution of the dissipative component. The full time evolution also reveals the effect of the UV background, and lets us directly compare present-day properties to the observations. Our numerical model includes cooling, star formation, chemical enrichment and feedback, and we allow for exchange of material with the intergalactic medium. We also include cosmological effects such as reionization. We use the same code, and with a few notable exceptions owing to the different physical effects that play a role in the two regimes, we use the same physics model and basic parameters as those employed by Scannapieco et al. (2008) in their study of the formation of Milky Way type disk galaxies, some 10^4 times larger in terms of stellar mass than the dwarf galaxies we consider here. We do not study local environmental effects, which may play a role for the closest companion satellite galaxies to the Milky Way. The main questions that we will address are how it is possible that systems of such low luminosity and seemingly similar total masses undergo such complex and diverse star formation histories, why dwarf spheroidal galaxies have such high mass-to-light ratios, why they appear to follow certain scaling laws, and if their formation and evolution in a cosmological constant dominated Cold Dark Matter (ΛCDM) universe can be explained by a consistent physical model. In Section 3.2, we present the computational methods which we have used and our choice of initial conditions. Section 3.3 follows with a presentation of the results of our simulations in broad terms, while we pay closer attention to the relevance of individual physical processes, particularly supernova feedback and UV radiation, in Section 3.4. In Section 3.5, we focus on the observed scaling laws, and present the dependence of our results on model parameters. We conclude with a summary where we discuss the achievements and shortcomings of the simulations in Section 3.6, and look forward to our future work.

3.2 Methods

The simulations presented here have been performed using the Tree-PM code GADGET-3 (Springel, 2005; Springel et al., 2008), which includes gravity and smoothed particle hydrodynamics. As an extension, metal-dependent cooling, star formation, chemical enrichment and energy injection from type II and type Ia supernovae have been implemented in the multiphase gas model of Scannapieco et al. (2005, 2006). This model has previously been used to study the effect of feedback on galaxy evolution in general terms (Scannapieco et al., 2006) and the formation of disk galaxies in particular (Scannapieco et al., 2008, 2009). In addition, some of our simulations contain an approximative treatment of self-shielding and low temperature cooling, which were not included in the previous model. In this section, we explain the most important characteristics of our model.

3.2.1 Cooling

Above the hydrogen ionisation temperature of 10^4 K, our gas cooling model is based on metal-dependent cooling functions of Sutherland & Dopita (1993). When we include cooling below 10^4 K, we use the extension of Maio et al. (2007). The adopted cooling function $\lambda(T)$, normalised to $n_H = 1$ cm^{-3}, is shown in Figure 3.1 for eight different metallicities. In our models, the gas density is typically below $n_H = 3 \times 10^3$ cm^{-3}. Consequentially, cooling is due mainly to collisional excitations, making the cooling function per unit volume proportional to ρ^2. We do not consider the effect of rotational excitations, and the resulting linear density dependence in the high density limit (Dalgarno & McCray, 1972). Below $10^4 K$, the cooling rate is a strong function of metallicity, which Maio et al. (2007) have calibrated to different iron abundances. Compton cooling, which is not shown in Figure 3.1, is included following the model of Katz et al. (1996). It is computed analytically, and is a function of the free electron density as well as the gas temperature difference with respect to the CMB temperature at the time.

In section 3.4.4, we investigate the significance of low temperature cooling in our simulations. In general, the difference is small, except for objects with virial temperatures significantly below 10^4 K.

3.2.2 Star Formation

Star formation is implemented so that gas particles can spawn, or be converted into, star particles, subject to certain conditions. We require the gas particle to be in a region of convergent flow. In addition, we impose a physical density threshold ρ_c on the local gas density. The existence of a threshold for star formation is motivated by observations (e.g. Kennicutt, 1989, 1998). Calculations
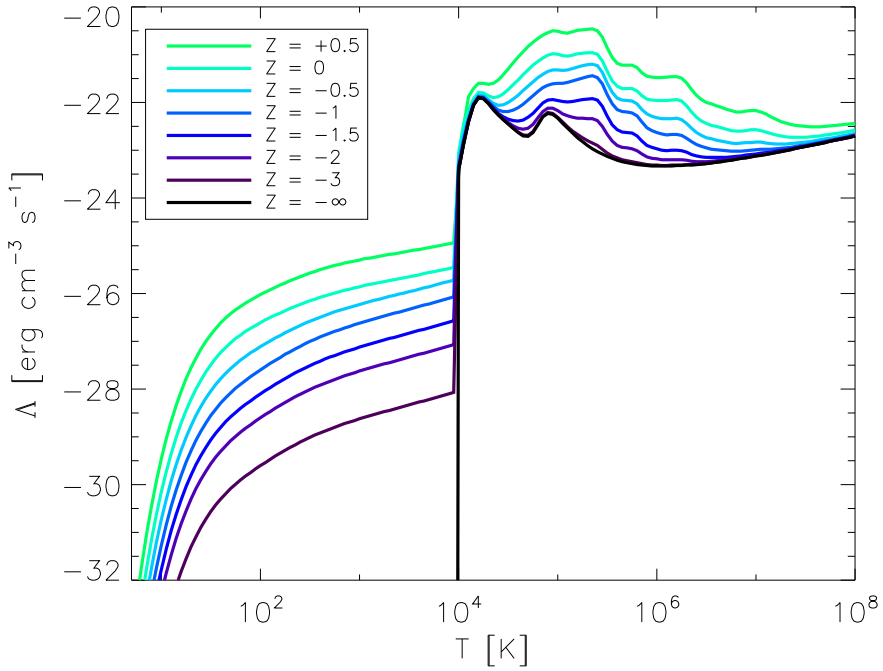
Figure 3.1: Normalised cooling functions, adopted from Sutherland & Dopita (1993) for temperatures above 10^4 K, and Maio et al. (2007) for lower temperatures. The metal-dependency is expressed in solar units, assuming $Z_\odot = 0.02$. Inverse Compton cooling is computed analytically, following Katz et al., and not included in this figure.

by Quirk (1972) as well as numerical simulations, e.g. by Katz et al. (1996); Springel & Hernquist (2003); Bush et al. (2008) and others have shown that the observed Kennicutt-Schmidt relation can be reproduced by imposing a volume density threshold, even though slightly different values are derived. Recently, Koyama & Ostriker (2009) demonstrated with high-resolution simulations of the turbulent interstellar medium that the star formation rate depends only weakly on the choice of ρ_c, and we adopt the value of $\rho_c = 7 \times 10^{-26} \text{gcm}^{-3}$, that was used in Scannapieco et al. (2006). We also impose a threshold of $\rho_g / \overline{\rho_g} \geq 57.7$ on the local gas overdensity (where $\overline{\rho_g}$ is the global mean density). This corresponds to a mean enclosed overdensity which is the minimum overdensity of a spherical, r^{-2} perturbation for gravitational collapse, and ensures that even at high redshift, star formation takes place only in virialised regions (Katz et al., 1996).

Subject to these constraints, the local star formation efficiency is regulated by a single efficiency parameter $c_\star$, so that the star formation rate is given by

$$\frac{d\rho_\star}{dt} = c_\star \frac{\rho_g}{t_{\mathrm{dyn}}}$$

where t_{dyn} is the local gas dynamical time. The creation of an individual stellar particle of mass $m_\star$ from a gas particle of mass m_g during the time interval Δt is stochastic, with the probability given by

$$p_\star = \frac{m_g}{m_\star} \left(1 - exp \left(-c_\star \frac{\Delta t}{t_{\mathrm{dyn}}} \right) \right).$$

In most of our simulations, we adopt a choice of $c_\star = 0.05$. We study the effect of different values in Section 3.5.3. Each star particle thus produced contains a single stellar population, whose metallicity is inherited from the parent gas particle. For simplicity, we assume a Salpeter initial mass function (Salpeter, 1955). We calculate the luminosities at any given time using the stellar evolution model of Bruzual & Charlot (2003).

3.2.3 Multiphase Interstellar Medium and Feedback

For each star particle, we determine the rate as well as the yields of supernovae type II and type Ia. Chemical yields are calculated separately for both types, following Woosley & Weaver (1995) and Thielemann (1993) respectively. Supernovae type II are assumed to be instantaneous, while for supernovae type Ia, we assume a uniform delay time distribution with given minimum and maximum delay times, as discussed in Section 3.5.4. We assume a constant energy production of 10^{51} ergs per supernova, which is released into the interstellar medium (ISM) as purely thermal energy.

The multiphase characteristic of the ISM, in which components of a wide range in temperature and density coexist, is lost in simple SPH models, where the smoothing kernel is a function of position only. This leads to an overestimation of the density in diffuse clouds neighbouring high density regions, and results in an underestimation of their cooling times, artificially increasing the star formation rate. It also means that feedback from supernovae is released primarily to the gas in star forming regions, where the densities are normally so high that the energy is lost immediately via radiative cooling. As a result, outflows and self-regulation of star formation are severely suppressed, and metals remain confined (Katz, 1992; Marri & White, 2003).

Most simulators fix the second problem by switching off cooling in the reheated particles for some time (e.g. Thacker & Couchman, 2000; Governato et al., 2007),

or by giving them a kick of arbitrarily specified amplitudes (e.g. Navarro & White, 1994; Dalla Vecchia & Schaye, 2008). The multiphase scheme for the interstellar medium of Scannapieco et al. (2006), addresses the problems at a fundamental level. It allows an overlap of diffuse and dense gaseous components by considering as neighbours in the smoothing kernel only gas particles with similar thermodynamic properties. Specifically, particles i and j are mutually excluded as neighbours if the ratio of their entropic functions $A(s)_{ij}$ exceeds a certain threshold and their pairwise-averaged velocity divergence multiplied by their mutual separation falls below the local sound speed, which avoids the decoupling of shock-waves.

However, this approach introduces some additional freedom in determining how the energy and metals released by supernovae are shared between the gas particles of the multiphase medium, which in our simulations each receive half of the total energy. In the dwarf galaxies we have simulated, most of the ejecta given to gas particles in the hot and diffuse phase eventually escape from the system, leaving mostly those that go to the cold phase to be included in subsequent generations of stars. Thus, increasing the fraction of metals given to the cold phase increases the final metallicity for a given stellar mass, whereas a high fraction of metals given to the hot phase creates strongly metal-enhanced winds. To some extent, we can use the observed metallicity-luminosity relation of dwarf spheroidals, shown in Figure 3.11, in order to calibrate this parameter. Because it effects all elements in the same way, the remaining degeneracy with the supernova Ia lifetimes can be partially broken by also considering the [Ca/Fe] ratios. We find relatively good agreement if 25% of the metals and energy are injected to the cold phase, and we use this value for all the simulations presented in this work.

3.2.4 UV Background

Quasar spectra indicate that the universe has been fully ionised from about redshift $z = 6$ (Fan et al., 2002). This has prompted us to include UV background radiation in our models, and we discuss its influence in Section 3.4.2. The question of whether dwarf galaxies survive the cosmic reionization epoch has been an intense area of study (e.g. Kitayama et al., 2000; Susa & Umemura, 2004; Hoeft et al., 2006, 2008). In hydrodynamical simulations, Hoeft et al. (2008) find that UV heating reduces the baryonic fraction in galaxies below a characteristic total mass, $6 \times 10^9 M_\odot$. However, Grebel & Gallagher (2004) found no clear signature of a widespread impact from reionization in their analysis of age distributions of nearby dwarf galaxies. In those simulations where the UV background is included, we have modified the cooling function for partially ionised gas by a heating term. Apart from tests where we have decreased the UV intensity, the intensity evolution of the UV background follows that of Haardt & Madau (1996).

3.2.5 Initial Conditions

All simulations are performed in the context of a ΛCDM cosmology, with $\Omega_\Lambda = 0.7$ and $\Omega_{\mathrm{m}} = 0.3$. We use a set of initial conditions based on pure dark matter simulations of isolated haloes by Hayashi et al. (2004). The halo on which our simulations are based (labelled D1 by Hayashi et al.) was selected from their set of dwarf haloes in order to yield an object whose high redshift progenitors fill a compact region in space, enabling us to limit the high resolution region to a small fraction of the total volume, whose (unscaled) side length is 35.25 h^{-1} Mpc. The resimulations start at redshift $z_i = 74$ with density fluctuations corresponding to a present value of $\sigma_8 = 0.9$ in the unscaled initial conditions. To the dark matter, gas particles were added at a rate of $\Omega_{\mathrm{b}} = 0.04$ and $\Omega_{\mathrm{DM}} = 0.26$. As described in Chapter 2.1, we have scaled the initial conditions at constant density, to give final halo masses between 2.33×10^8 and 1.18×10^9 $h^{-1}\mathrm{M}_\odot$, but identical formation redshift and (scaled) assembly histories for all our objects. This causes an effective change of the normalisation of the power spectrum between the simulations, but as Colín et al. (2004) have shown, due to the early formation of dwarf haloes and the flatness of the linear fluctuation amplitude in this mass regime, the influence on the evolution of individual haloes is expected to be insignificant compared to the scatter between objects. The linear scale factor f_s of each simulation is also listed in the second column of Table 3.1.

As described in Section 3.2.6, we have also performed simulations of varying particle numbers (up to 2.83×10^6 for dark matter and 1.21×10^6 for gas). The gravitational softenings for each particle type were fixed to 1/10th of the respective mean interparticle separation in comoving coordinates in the initial conditions and limited, in physical coordinates, to $\sim$ 1/5th of the mean separation within the collapsed haloes. This allowed a spatial resolution typically below 100 pc (depending on the scale and the number of particles). Haloes were identified using a Friends-of-Friends (FoF) method with a linking length of 0.2. In each case, over a hundred small haloes with 32 particles or more were formed in the simulated volume, and depending on the choice of parameters of the baryonic physics model, several of them formed stars. However, in each case we limit our analysis to the most massive one, for which the effective resolution is highest. We have made tests to confirm the scale-free behaviour of the pure dark matter simulations. We find that in all cases, the dark matter profiles are well-fitted by a Navarro, Frenk and White (NFW) model, down to the resolution limit. Note that all our simulations have the same assembly history, apart from resolution effects. This means that we cannot say anything about the scatter in properties expected among similar mass haloes. On the other hand, differences between our various simulations must therefore be due entirely to differences in the assumed physics or the numerical parameters. Cosmic variance plays no role.

3.2.6 Effects of Resolution

The hydrodynamical model, and the recipes for feedback and star formation may also be influenced by resolution effects. Scannapieco et al. (2006) have tested the model for numerical convergence. Since we extend their model to a new mass range, we have performed additional tests. Simulations 1-28, summarised in Table 3.1, are run with a constant number of 8.7×10^5 dark matter particles, 1.7×10^5 of which are in the high resolution Lagrangian volume that also contains 1.7×10^5 gas particles. The corresponding particle masses range from $6.6 \times 10^3 M_\odot$ and $1.2 \times 10^3 M_\odot$ in simulation 1, to $3.3 \times 10^4 M_\odot$ and $5.8 \times 10^3 M_\odot$ in simulation 9, for dark matter and gas particles, respectively. The number of stellar particles varies, depending on star formation rate, and the stellar particle masses range between $5.4 \times 10^2 M_\odot$ in simulation 1 and $2.7 \times 10^3 M_\odot$ in simulation 9. Wherever we have changed the other parameters of the model, we have kept the resolution fixed.

We have also performed two simulations, 29 and 30, with a mass resolution increased by a factor of eight compared to simulations 2 and 9, respectively, while all other parameters were kept constant. The results are shown in the bottom rows of Table 3.1. While the respective total masses of the systems are constant to within a few percent, a statement of the fact that the gravitational part of the force calculations is largely resolution-independent, and that the coupling of the dark matter to the baryons in our simulations is small, the total stellar mass produced in both cases decreases by $\sim 40\%$. With increased resolution, star formation begins slightly earlier and at lower halo masses, resulting in quicker heating and outflows of the gas.

However, this difference is small compared to the influence of physical parameters, such as total mass. The simulations at different resolutions also show similar properties with respect to the response to the UV background, the self-shielding threshold and the metal-enrichment. The results remain consistent with global scaling relations, as illustrated in Figures 3.11 and 3.13, where we have included the high resolution results of simulations 29 and 30, together with the results of simulations 1-9.

3.3 Formation and Evolution

We find that the evolution of the dwarf galaxies that we simulate is strongly affected both by supernova feedback and by the UV background radiation. It is the combination of these two effects that shapes the evolution of the galaxy. We begin this section by showing the evolution of a typical dwarf galaxy up to the present time, including all the different effects that play a role, but focusing on the global picture. We then try to disentangle the effects of feedback and UV radiation, and look in more detail at how they each influence the evolution in Section 3.4.

3.3.1 Time Evolution

Figure 3.2 illustrates different stages in the evolution of a proto-galaxy (labelled simulation 16 in Table 3.1) together with its environment. The top row shows the position of dark matter, gas and star particles. The scale of the panels is kept constant in physical coordinates with a side length of 20 kpc, hence the volume displayed shrinks in terms of comoving coordinates and the view zooms in on the central galaxy as the redshift decreases from left to right. In the first two columns, the filamentary structure of the environment is still recognisable, together with a number of smaller haloes that have accumulated gas, but not yet begun star formation. The bottom row shows the distribution of gas particles on the density-temperature plane, both within and outside of the most massive halo.

As the halo forms, gas begins to fall in, contracts and gets heated. At a temperature of 10^4 K, radiative cooling becomes so efficient that the gas can contract essentially isothermally, until the central density reaches the threshold for star formation, as described in Section 3.2.2. At $z = 12.3$, which corresponds to the leftmost column of Figure 3.2, the first stars have already formed in the central object, and supernovae of type II have started heating the gas, already pushing some of it out. This is visible also in the bottom row of Figure 3.2, where the gas particles that start appearing to the right of 10^4 K, which indicates that they have been heated by supernovae, are no longer bound to the halo.

The total masses of the three components; dark matter, gas and stars identified as belonging to the halo by a Friends-of-Friends algorithm, are shown as a function of time in Figure 3.3. Star formation in the galaxy continues for about one Gyr, as more gas gets accreted and cools, whilst supernovae of both type II and type Ia continue to expel the interstellar medium. Ejection and heating balance accretion and cooling at $z = 9$, and the star formation rate peaks at $z = 8$. By redshift $z = 6$, the star formation rate has already decreased by a factor of two from its peak value of $3 \times 10^{-1} M_\odot$ yr^{-1} due to feedback.
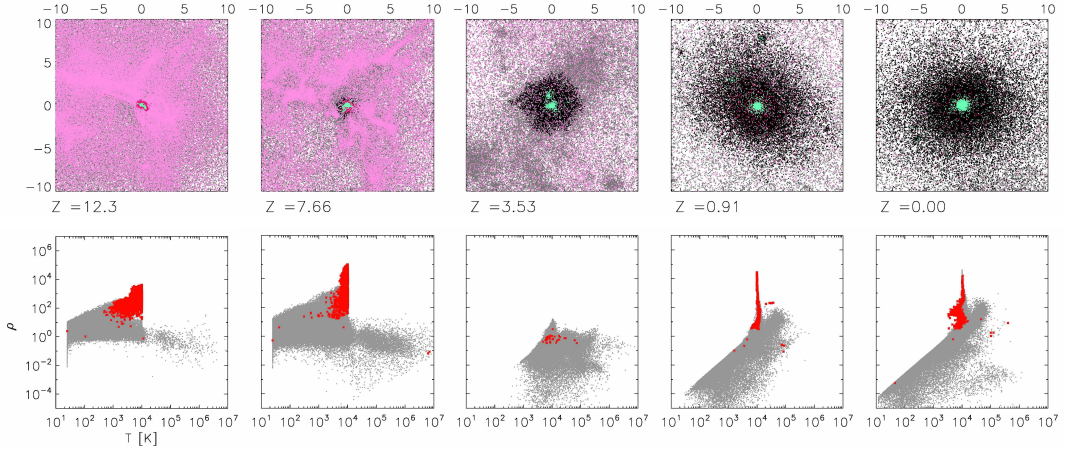
Figure 3.2: Top row: Spatial distribution of particles of different types at different redshifts of simulation 16 in Table 3.1. Dark matter particles are shown in black (or grey), gas particles in red (or purple), depending on whether they are bound to the object in the centre, or whether they are part of other haloes or the intergalactic medium. Star particles are shown in green. Bottom row: Temperature and density of gas particles. Red dots indicate gas that is bound to the central halo, while grey dots are for particles in all other parts of the simulated volume. Both supernova feedback and UV radiation are included in this simulation, which has a final halo mass of $\sim 7 \times 10^8 M_\odot$. It can be seen that the central halo is almost gas-free at redshift $z = 3.5$, due to the combined effect of feedback and the UV background. Feedback heats the gas and blows some of it out during the early stages of the evolution. After redshift $z = 6$, UV radiation heats the remaining gas above the haloes virial temperature, quickly removing it from the halo, and it also heats the intergalactic medium. Some gas falls back to the main halo at later times, but does not lead to significant amounts of star formation. Smaller haloes without star formation, and hence not subject to feedback, also lose their gas due to the UV radiation.

Figure 3.3: Evolution of the bound dark matter mass (solid black), gas mass (dotted blue) and stellar mass (dashed red) as function of redshift for simulation 16, the same simulation that is shown in Figure 3.2 in several snapshots. The simulation includes cooling, star formation, supernova feedback and a cosmic UV background, but no self-shielding. It reaches a virial mass of $\sim 7 \times 10^8 \, \mathrm{M_\odot}$, and a stellar mass of $\sim 4 \times 10^6 \mathrm{M_\odot}$ at $z = 0$. Other properties are summarised in Table 3.1.

At $z = 6$, the UV background suddenly switches on. In this particular model, it is sufficient to heat the remaining gas above the virial temperature of the halo in a very short time, resulting in its expulsion, and a sharp end to star formation. Some gas falls back at a later stage, but does not reach sufficient density for significant star formation.

It can also be seen in Figure 3.3 that the dark matter halo in this simulation continues to grow over time through accretion and minor mergers. It is worth noting that throughout the period of star formation, from the onset around redshift $z = 16$ to the end shortly after redshift $z = 6$, the halo mass is several times smaller than the final value, which might be observed today. This behaviour is common to all of our simulations, independent of the baryonic physics. It contributes to the high efficiency of the winds in our models. It also suggests that the impact that supernova feedback might have had during the history of a particular dwarf galaxy not only depends on its 'mass' as it is presently observed, but also on the co-evolution of its star formation and the assembly of its halo at earlier times. This fact is taken into account explicitly in semi-analytical models like that of Ferrara & Tolstoy (2000), but it is overlooked in non-cosmological simulations that assume collapse in a static potential.

In our simulations, the halo continues to grow unperturbed up to $z = 0$. This is not necessarily true for haloes of satellite galaxies, which may have experienced truncation upon infall (Nagai & Kravtsov, 2005). However, at least according to our models, it is likely that star formation would have finished before a typical infall redshift of $z \sim 1$ or below (Li & Helmi, 2008). While we therefore do not expect environmental effects to significantly alter the stellar population, they may further skew the correspondence between observed halo masses today, and gravitational potential in place at the epoch of star formation. We also have to assume that the late infall of gas, leaving in some cases a small amount of gas at $z = 0$, which would be in disagreement with observations, is prevented in the Local Group environment.

3.4 The Role of Physical Processes

As we have seen, feedback from supernovae is sufficient to expel gas from the shallow potential wells of forming dwarf-galaxies, and it is responsible for regulating star formation at least up to redshift $z = 6$. In order to investigate the relative importance of feedback and UV heating, and to disentangle their respective contributions over time, we have performed test simulations where only one of the two processes is included.

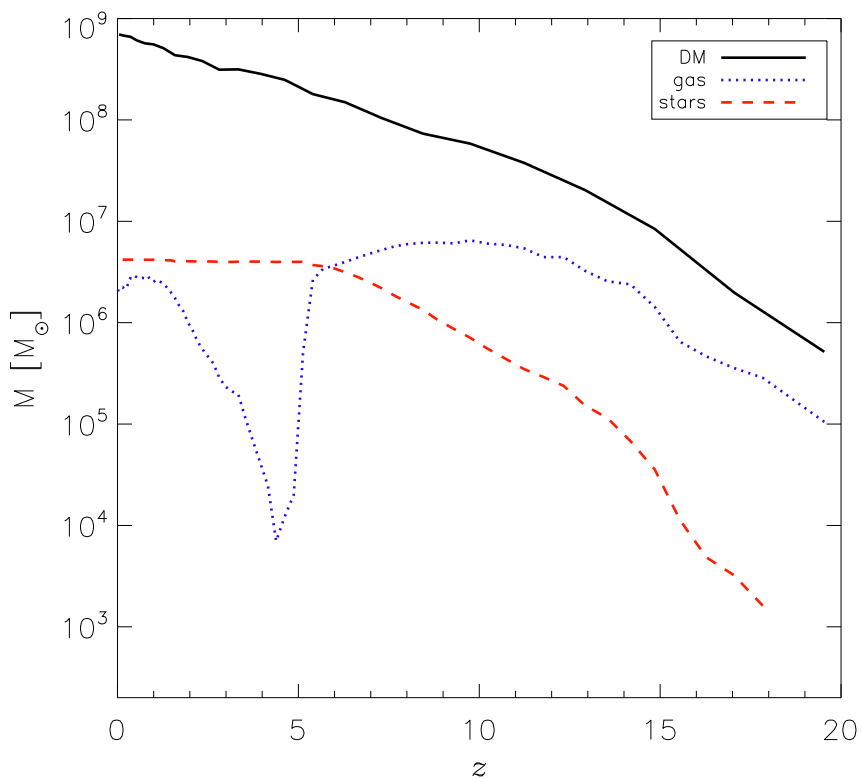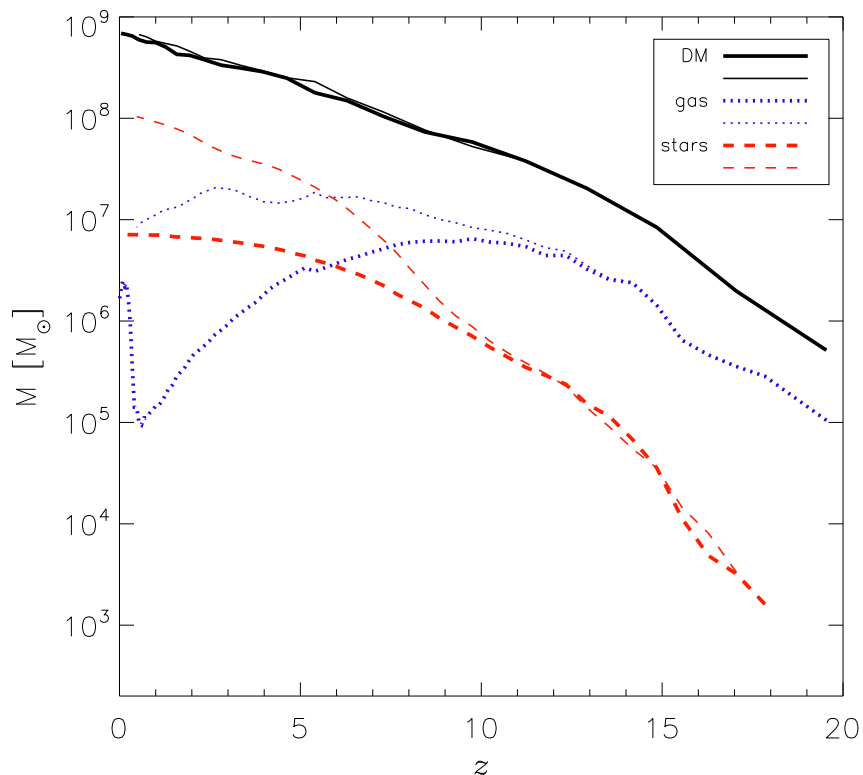Figure 3.4: Evolution of the dark matter mass (solid black), gas mass (dotted blue) and stellar mass (dashed red) as functions of redshift, for simulations 25 and 11. Initial conditions and the final dark-matter mass of $\sim 7 \times 10^8 \mathrm{M_\odot}$ are identical to those of simulation 16, shown in Figure 3.3, but the evolution is different. The thick lines show the evolution of simulation 25, where feedback is the only source of heating, whereas the thin lines are for simulation 11, that includes UV radiation from redshift $z = 6$ but no feedback. In the first case, feedback alone is sufficient to remove most of the gas, but more slowly compared to Figure 3.3. In the case of simulation 11, in the absence of feedback, the decline in the gas mass is solely due to consumption and conversion to stars. Furthermore, without feedback, the UV background present from $z = 6$ has almost no effect on the gas mass or the star formation rate. The resulting stellar masses are vastly different: $7 \times 10^6 \mathrm{M_\odot}$ without UV for simulation 25, and $\sim 10^8 \mathrm{M_\odot}$ for simulation 11 without feedback.

Figure 3.4 illustrates two such 'incomplete' scenarios. We show the evolution of dark matter, gas and stellar mass, for simulation 25, where feedback is the *only* source of thermal energy, and for simulation 11, where UV radiation is included, but stellar feedback is ignored. They can be compared with our reference simulation 16 in Figure 3.3, where the combined effect of supernova feedback and UV background radiation are shown. All three simulations have identical initial conditions and numerical resolution. While the growth of the dark matter mass appears unaffected by the baryonic physics, the dashed and dotted lines, which indicate the stellar and gas mass, respectively, show large differences. The outflow induced by feedback in simulation 25 causes the thick dotted line representing the gas mass in Figure 3.4 to peak at about $z = 9$ and decline thereafter, similar to Figure 3.3. The star formation rate (not shown) also declines and the thick dashed line, representing the total stellar mass, increases ever more slowly, reaching $7 \times 10^6 \mathrm{M}_\odot$ at redshift $z = 0$. In contrast, the thin dotted line in Figure 3.4, which represents the gas mass without feedback, shows no decline at high redshift. The total baryon fraction of the halo stays constant at around 1/6th, indicating that the late decline of the gas mass is due solely to consumption by star formation. It is worth reiterating that this simulation includes the full UV background (see Section 3.4.2), without self-shielding (see Section 3.4.3). However, contrary to the results of Figure 3.3, we find that when thermal feedback is ignored, the UV radiation has no effect either. The gas density is so high that the gas can cool fast enough to balance any heating due to the cosmic UV background.

3.4.1 The Importance of Feedback

In summary, we find that feedback alone can blow out all the remaining gas before redshift $z = 0$ even in the absence of photoelectric heating, albeit at a much slower rate, resulting in a larger number of intermediate age stars. Even in this case, only between 3% and 6% of the total amount of gas ever bound to the halo gets turned into stars, depending on the mass of the object. Most of the gas still escapes to the intergalactic medium, enriching it with metals.

In simulations without thermal feedback (simulations 10 and 11 in Table 3.1, thin lines in Figure 3.4), the picture is drastically different. Not only is the star formation more efficient during the early stages, the interstellar gas also becomes so dense that all effects of the UV background radiation discussed in Section 3.4.2 are eliminated due to very efficient cooling. The result is a system of large stellar mass (up to $10^8 \mathrm{M}_\odot$ in the case of simulation 11, compared to $4 \times 10^6 \mathrm{M}_\odot$ for the same initial conditions run with feedback), low mass-to-light ratio, high metallicity, an abundance of young stars, and a high gas content. All these properties are incompatible with observations of Local Group dwarf spheroidals.

We conclude that feedback is necessary to shut down star formation in those haloes massive and dense enough to cool and begin forming stars. Under the assumption, supported by observations (e.g. Lewis et al., 2007; Fraternali et al., 2009), that at least some of the local Group dwarf spheroidals have evolved in isolation, these results suggest that supernova feedback is the key factor in determining their stellar evolution.

3.4.2 The Influence of the UV Background

To further elucidate the influence of the UV radiation, in Figure 3.5, we show the evolution of a system that includes feedback but no UV radiation (simulation 25 in Table 3.1), a simulation otherwise identical to our reference simulation 16 described in Section 3.3.1, which is shown in Figures 3.2 and 3.3. The most obvious difference to note when comparing the two sets of figures is in the low density regions of the intergalactic medium not part of our main halo, where heating by the UV background is most effective.

We find that all haloes that are not massive enough to accrete sufficient gas to form stars before $z = 6$ subsequently lose their gas when the effects of photoelectric heating are included. One consequence of this is that while the main halo grows through accretion of smaller haloes, these minor mergers are essentially gas-free and do not trigger renewed star formation. It also supports the idea that reionization establishes a lower mass threshold for dwarf galaxy haloes, and so provides part of the solution to the 'missing satellites problem'. However, we do not observe star formation in these haloes, even when UV radiation is ignored, most likely due to inefficient cooling as a result of insufficient resolution.

For those objects we consider as the progenitors of dwarf galaxies listed in Table 3.1, i.e. those massive enough to acquire dense, star-forming gas at high redshift, we have already shown that the UV background alone is not sufficient to shut off star formation at $z = 6$. Feedback is required in order to make the gas diffuse and to reduce its radiative cooling efficiency. However, when this requirement is met, the UV background radiation has a strong influence on the star formation timescale. While the difference in total stellar mass in a given dark matter halo varies from 30 % for the largest system to a factor of three for the smallest system we have studied, this alone may not be enough to be discriminatory when comparing mass-to-light ratios with observations.

However, a substantial difference is also found in the age and metallicity distributions. When star formation continues beyond reionization, many intermediate age stars with high metallicities are formed, and, as can be seen in Table 3.1, this causes the median metallicity to saturate around $[Fe/H] = -1.1$ when the UV background is ignored. Moreover, while properties such as the total stellar mass and metallicity also depend on the initial mass and (less strongly) on other
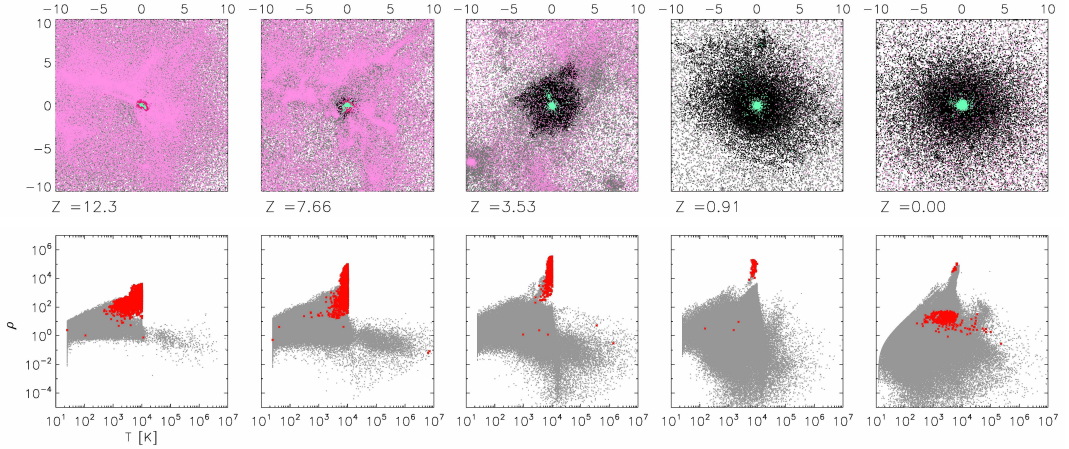
Figure 3.5: Top row: Spatial distribution of particles of different types at different redshifts of simulation 25. Dark matter particles are shown in black (or grey), gas particles in red (or purple), depending on whether they are bound to the object in the centre, or whether they are part of other haloes or the intergalactic medium. Star particles are shown in green. Bottom row: Temperature and density of gas particles. Red dots indicate gas that is bound to the central halo, while grey dots are for particles in all other parts of the simulated volume. Simulation 25, also shown in Figure 3.4 (thick lines), has initial conditions identical to the one shown in Figure 3.2, but contains no UV radiation. It reaches a final halo mass of $\sim 7 \times 10^8$. While the system still looses almost all its gas, this happens more slowly compared to the case with UV radiation, and the stellar mass continues to grow beyond redshift $z = 6$. The most noticeable difference, however, is in the smaller haloes (10^6 M$_\odot$ or less), which did not form stars early on, and which would now be able to retain their gas.
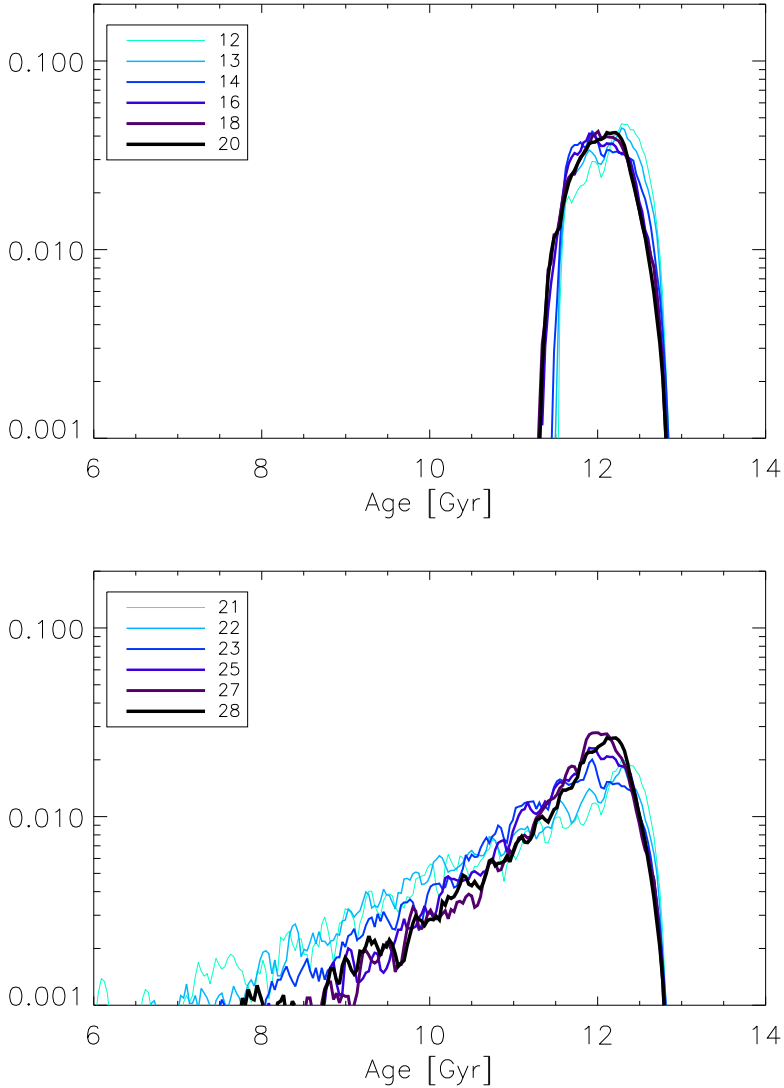
Figure 3.6: Distribution of stellar ages in Gyr. Simulations of the same halo mass are shown in the same colour in the two panels, darker colours and thicker lines indicate higher mass. A UV background (but no self shielding) is included for simulations 12-20, in the top panel, while the UV background is ignored in simulations 21-28, on the bottom. The final halo masses range from $2.3 \times 10^8 M_\odot$ (simulations 12 and 21, lightest blue) to $1.2 \times 10^9 M_\odot$ (simulations 20 and 28, black). Other properties of the simulations are summarised in Table 3.1.

parameters of the model (see Section 3.5), the age distribution of the stars does not.

In all cases with UV radiation, the termination of star formation at $z = 6$ results in a narrow age distribution, as can be seen in Figure 3.6, while in all cases without the UV background, there is a pronounced intermediate-age tail. This is significant, because there appear to be examples of both types of galaxies in the Local Group (Grebel & Gallagher, 2004). We have tested the dependence on the overall UV intensity, and found qualitatively similar results when we decreased it by up to a factor of 10 from the Haardt & Madau (1996) level.

Furthermore, while there may be local variations in the UV background, particularly at higher redshift and from sources other than quasars (e.g. Ciardi et al., 2003), the mean free path of UV photons in the intergalactic medium is on the order of tens of Mpc (Bolton et al., 2004). This seems to rule out the possibility that the observed variation in star formation histories within the Local Group dwarf spheroidals can be attributed solely to small-scale variations of the UV background radiation level originating from quasars at large distances.

3.4.3 The Effect of Self-Shielding

We have also performed simulations where we approximate the effects of self-shielding of the dense interstellar medium against the UV background. While we do not include radiative transfer in these simulations, we use a threshold on the density of neutral hydrogen (HI) gas of $n_{HI} = 1.4 \times 10^{-2} \text{cm}^{-3}$, following the results of Tajiri & Umemura (1998). Including this effect leads to an interesting dichotomy. At the more massive end, as shown in the bottom row of Figure 3.7, the evolution in the central object proceeds almost as in the case with no UV background, while at the low mass end, as shown in the top row of the same figure, the evolution is similar to the case with UV heating but no shielding.

Figure 3.8 shows the star formation rates over time for a total of six simulations of two different halo masses. Simulations 2 and 7 which include shielding, as discussed above, are compared to two sets of equal mass-mass counterparts: Simulations 13 and 18 which have a UV background but no shielding, and simulations 22 and 27, which do not include UV radiation. The evolution of each triplet of a given mass proceeds identically up to redshift $z = 6$. Subsequently, the presence of the UV background quenches star formation in both simulations without shielding, while the two simulations without UV radiation both see a gradual decline in their star formation rate, solely due to feedback. However, when shielding is included, it has no effect in the low-mass case, where the star-formation rate shows a sharp decrease, similar to the unshielded case. In contrast, in the high-mass case, the star formation rate with shielding closely follows that of the corresponding simulation without UV radiation.
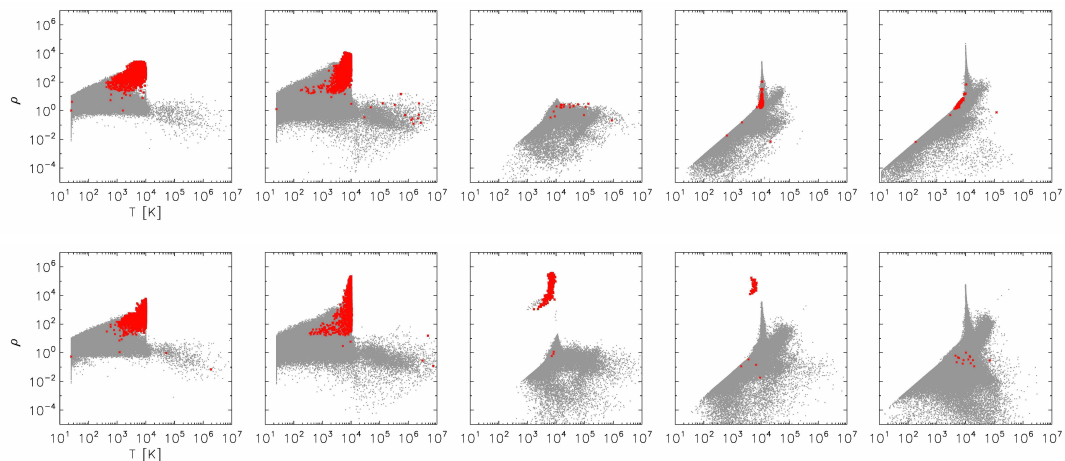
Figure 3.7: Temperature and density of gas particles. Red dots indicate gas that is bound to the central halo, while grey dots are for particles in all other parts of the simulated volumes. Results from two simulations of different mass illustrate the effect of self-shielding. Simulation 2, shown on top, has a final halo mass of $3.5 \times 10^8 \mathrm{M}_\odot$, while simulation 7, shown below, reaches $9.2 \times 10^8 \mathrm{M}_\odot$. Both simulations include supernova feedback and UV radiation, similar to those shown in Figure 3.2. At redshift $z = 7.6$, prior to reionization, the higher mass simulation has been able to keep a larger amount of dense interstellar gas in the centre, whereas feedback has caused the gas in the lower mass galaxy to be more diffuse. At redshift 3.5, the gas in the lower mass galaxy has been lost, while the higher mass galaxy has kept its high density gas, allowing it to form stars up to redshift $z = 1$. In both cases, grey dots, associated with the IGM and smaller haloes, are distributed similarly to the case with UV heating but no shielding in Figure 3.2, indicating that self-shielding is not efficient in these low density environments.
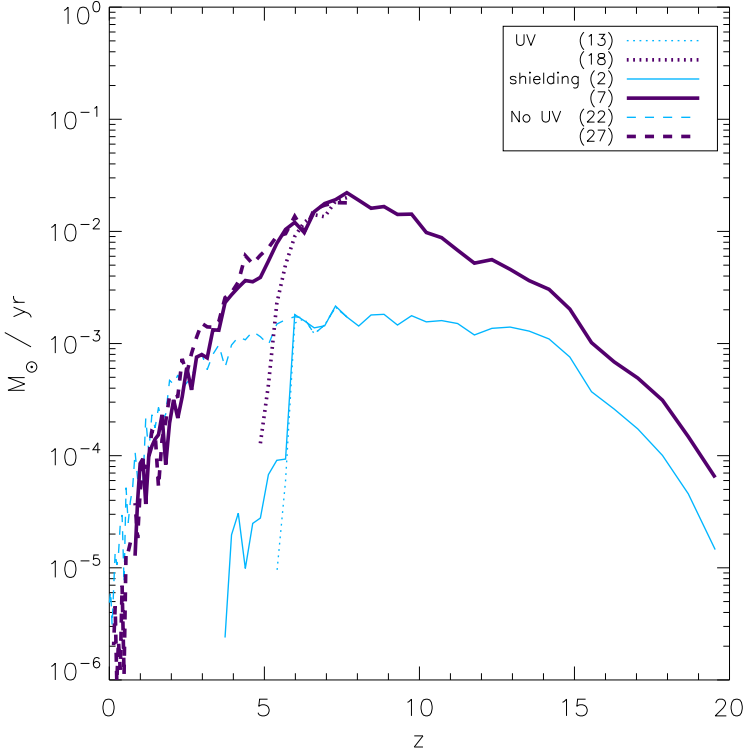
Figure 3.8: Star formation rate in $M_\odot$ yr^{-1}, for a total of six simulations in two groups of different halo masses. Simulations 2, 13 and 22, which have a final halo mass of $\sim 3.5 \times 10^8 M_\odot$, are plotted as thick blue lines, while simulations 7, 18 and 27 reach $\sim 9 \times 10^8 M_\odot$, and are plotted as thin purple lines, in correspondence to the colours used in Figures 3.6 and 3.9 for the same masses. All simulations include supernova feedback, they differ in the treatment of the UV background and/or self-shielding. Simulations 22 and 27 (dashed lines) include no UV radiation. Simulations 13 and 18 (dotted) include a UV background, and simulations 2 and 7 (solid) also include self-shielding. It can be seen that the star formation rates for all systems of a given mass are identical up to redshift $z = 6$. After that, for both masses, they decline sharply in the scenarios with UV background and no shielding (dotted), and more gradually when the UV background is ignored (dashed). However, the impact of self-shielding (solid) is different for the two masses. In the high mass halo, the result with self-shielding resembles the case without UV radiation, whereas in the low-mass halo, the star formation rate drops almost as sharply with self-shielding as without.
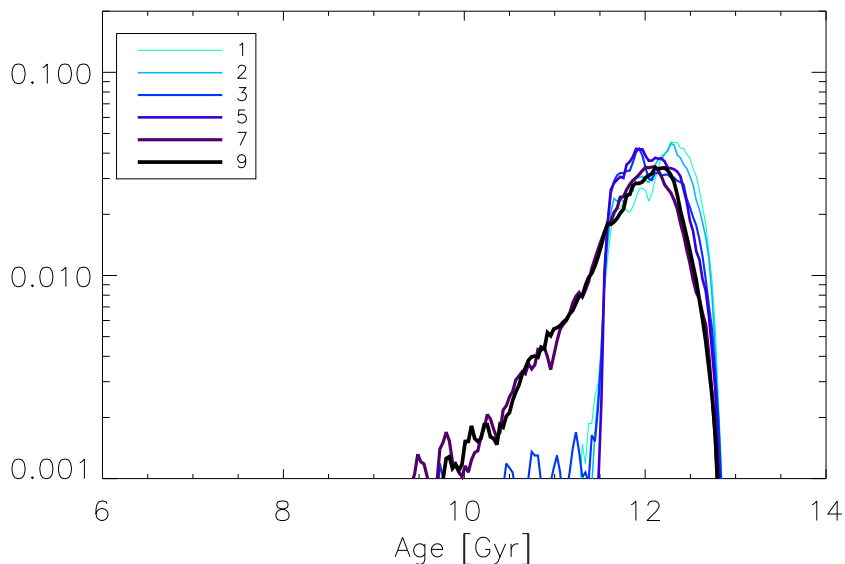
Figure 3.9: Distribution of stellar ages in Gyr, in simulations 1-9, which include feedback, a UV background and self-shielding, as described in the text. As in Figure 3.6, the colours and line strengths indicate different halo masses, from $2.3 \times 10^8 M_\odot$ (simulation 1, lightest blue) to $1.2 \times 10^9 M_\odot$ (simulation 9, black). Other properties are listed in Table 3.1. While simulations 1-5 show only an old stellar population, similar to the top panel of Figure 3.6, a transition occurs around a final halo mass of $\sim 8 \times 10^8 M_\odot$, above which self-shielding becomes effective, allowing star formation to continue beyond $z = 6$.

The age distributions shown in Figure 3.9 reflect this behaviour. Systems with lower mass only have small age spreads resulting from a single burst, comparable with the results without shielding shown in Figure 3.6 (matching colours indicate equal masses). Higher mass objects possess intermediate age tails, similar to the result without a UV background.

Again, we find that while it is the response of the interstellar medium to the UV radiation that ultimately splits the two scenarios, it is the effect of feedback prior to reionization that is at the root of this dichotomy. In the low-mass case, feedback dilutes the gas more efficiently prior to reionization, and thereby prevents it from self-shielding. In the high-mass case, the gas in the centre remains dense enough to become self-shielding and to prevent a blow-away.

While the approximation of self-shielding is very crude, and should be confirmed by more detailed analysis with full radiative transfer, it is interesting that the critical gas density that determines whether galaxies form stars after reionization appears to lie just at the right level to allow the formation of both kinds of dwarf spheroidal galaxies in simulations which include supernova feedback. On the basis of these arguments, it appears that the inclusion of cosmic reionization and a UV background with the possibility of self-shielding is the physically correct assumption. In the subsequent analysis, we continue to use the Haardt & Madau (1996) model, together with the Tajiri & Umemura (1998) approximation for self-shielding.

We note, however, that the environment in which our galaxies form is different to that of the Local Group. As discussed in Chapter 4, this may play an additional role in the star formation history. Possible environmental effects include not only a local variation in the UV background, but also other mechanisms for removing gas, or reducing its density in satellite galaxies. While the removal of gas, by ram pressure stripping, for example, could halt star formation directly, our results indicate that an indirect mechanism might be just as efficient, if it makes the gas susceptible to evaporation after $z = 6$. That such environmental effects play a role is supported by the observation, presented in Section 1.5.5, that dwarf spheroidals close to the centre of the Milky Way tend to have fewer intermediate age stars than those further out, although this trend is less clear for the M31-satellites (Grebel, 1997).

3.4.4 The Role of Low Temperature Cooling

As described in Section 3.2.1, we have performed simulations with and without metal and molecular cooling below 10^4 K. Bromm & Clarke (2002) found in their simulations that atomic hydrogen cooling alone is not sufficient to form the observed dwarf galaxies, and they as well as other authors (e.g. Mashchenko et al., 2008; Revaz et al., 2009) have found different ways to include low temperature cooling due to molecules and metals in their simulations. By contrast, Mayer et al. (2006) and others have only considered cooling above 10^4 K. We have repeated several simulations with additional low temperature cooling, using the extended cooling functions of Maio et al. (2007). Figure 3.10 shows the distribution of gas particles in the temperature-density plane at different redshifts for two simulations with low-temperature cooling. Both simulations have identical initial conditions to Simulations 2 and 7, respectively, and include the full physical model of supernova feedback, UV radiation and self shielding. Figure 3.10 can be compared to Figure 3.7, which shows the evolution without low temperature cooling. In each case, with low temperature cooling, star formation proceeds at slightly higher efficiency at high redshifts. As a consequence of supernova feedback acting at a lower

halo mass, the interstellar gas mass peaks at higher redshift. For the lower mass scenarios, the effect on the total stellar mass is minimal. In the high mass case, however, the decreased gas mass at $z = 6$ decreases the efficiency of self-shielding against the cosmic UV background, and hence the amount of subsequent star formation.

In general, we find that the inclusion of low-temperature cooling does not have a very strong effect on the formation of dwarf galaxies in the mass range of 10^8 to $10^9 \mathrm{M}_\odot$, which we have considered in this study, and which have all began to form stars before reionization. It does not qualitatively alter the response of the interstellar medium to supernova feedback or the UV background.

However, we cannot exclude the possibility that low temperature cooling may have a significant effect on the formation and evolution of galaxies with even lower halo masses, whose virial temperatures are far below 10^4 K. In all of our simulations, we have assumed the gas to be metal-free before the first stars are formed and release metals ab initio. As the cooling function in Figure 3.1 shows, possible pre-enrichment of the intergalactic medium could enhance the cooling efficiency, which might also play a role in this case.

3.5 Exploring the Parameter Space

Even though our model is physically motivated, it also contains a certain degree of parametrisation in addition to the numerical parameters discussed in Section 3.2, which cannot be determined ab initio in our simulations. We have therefore explored a range of variables that have a direct physical significance, some of which we hope to constrain by comparison with observations, and others that may simply help to explain the variation amongst the observed systems.

3.5.1 Total Mass: Scaling Relations

Measurements of stellar kinematics of the Local Group dwarf spheroidal and ultra-faint dwarf galaxies have recently revealed a striking similarity in the inferred virial mass contained within the central 300 pc. It is consistent with a common value of $10^7 \mathrm{M}_\odot$ over several orders of magnitude in luminosity (Strigari et al., 2008). This suggests that all dwarf spheroidals reside in similar dark matter haloes. Why then do they have such a large variation in stellar mass?

Some of the effects of the depth of the potential well have already been described in Sections 3.4.2 and 3.4.3, reflecting the fact that no parameter can really be studied in isolation. In this section, we look at the series of simulations that includes all of the physical processes: cooling, star formation, feedback, UV radiation and self-shielding, but focus on a comparison with the observed scaling relations. As
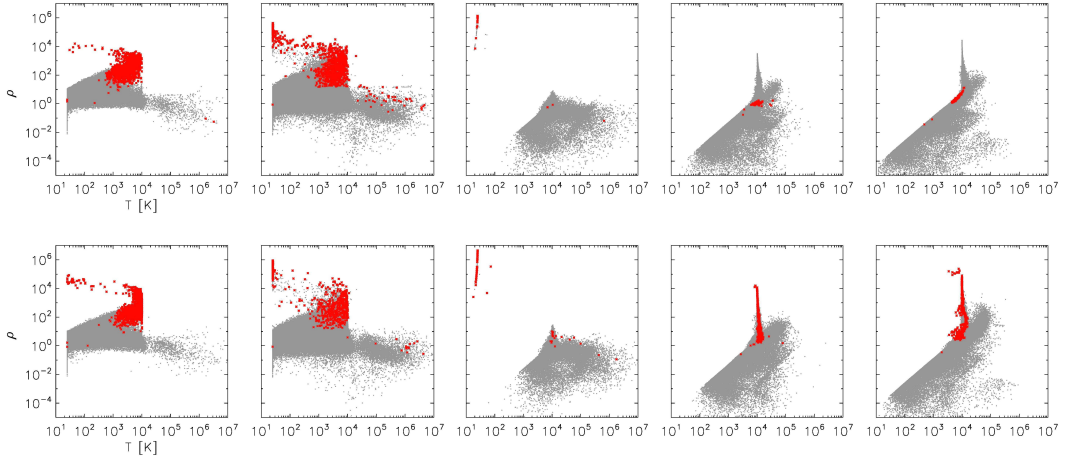
Figure 3.10: Temperature and density of gas particles. Red dots indicate gas that is bound to the central halo, while grey dots are for particles in all other parts of the simulated volumes. Initial conditions for the simulations are identical to Simulations 2 and 7, shown in the top and bottom rows of Figure 3.7, respectively, which include supernova feedback, UV radiation and self-shielding, and which reach final halo masses of 3.5×10^8 and $\sim 9 \times 10^8 M_\odot$. As a result of additional low temperature cooling in both haloes, early star formation and supernova driven outflows occur at a slightly higher rate. In the low mass case, the subsequent evolution is very similar to the situation shown in the top row of Figure 3.7 without low-temperature cooling. As in the case without low temperature cooling, the residual amount of gas is again too small to be effectively self-shielding by the time reionization sets in at redshift $z = 6$. In the high mass scenario, the amount of residual gas at $z = 6$ is also reduced with respect to the case without low-temperature cooling, and hence the effect of self shielding is somewhat lower, leading to slightly less subsequent star formation.
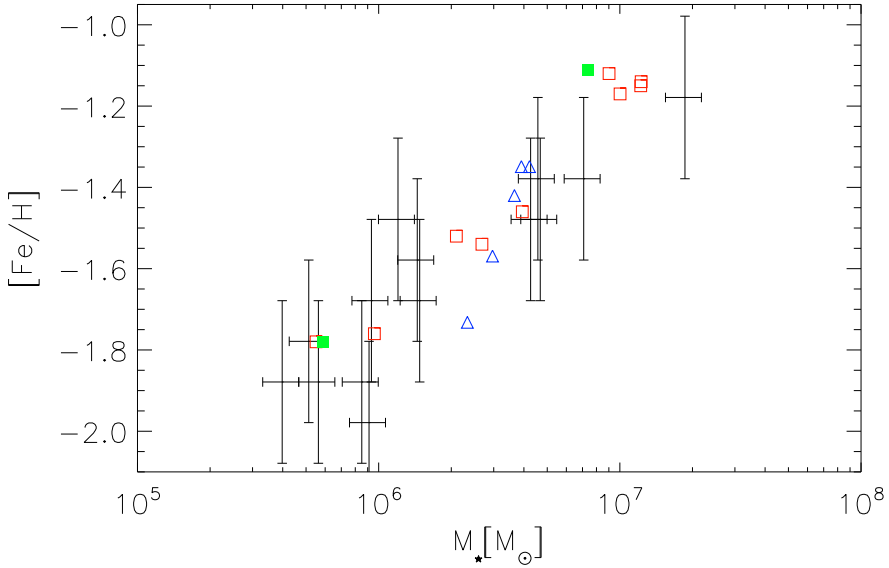
Figure 3.11: Mean metallicity and stellar mass for 14 observed dwarf spheroidals, in black with error bars, together with the results from our simulations. Red squares show a sequence of simulations (1-9) with varying initial masses, which gives a good fit to the observations. Also shown, with blue triangles, is a sequence of simulations with varying parameters of $c_\star$. While it intersects with the observed relation, the slope is much too steep compared with observations. The two filled, green squares are the results of two simulations with increased resolution, as discussed in Section 3.2.6. The observational uncertainties, as given by Woo et al., are 0.2 dex for [Fe/H] and 0.17 dex for stellar mass.
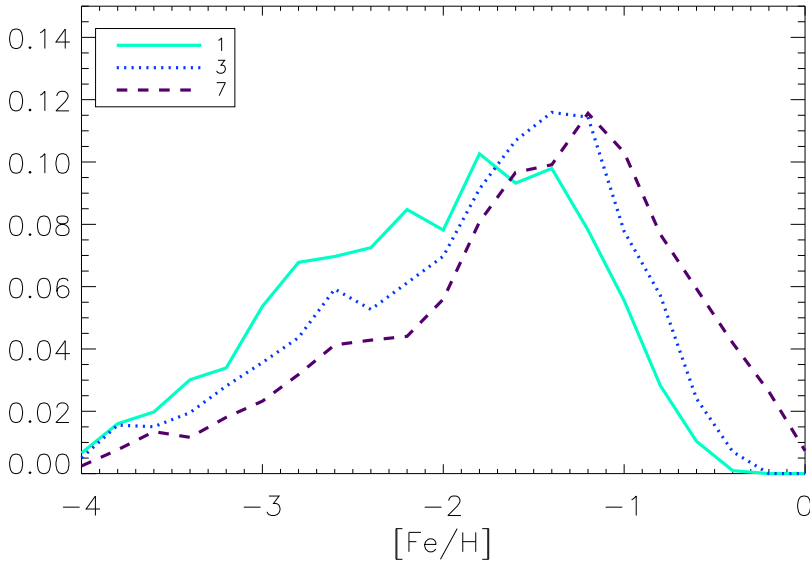
Figure 3.12: Relative, mass-weighted metallicity distribution of individual stars for the three simulations 1, 4 and 7, which vary in final halo mass.

described in Section 3.2.5, we have scaled the initial conditions at constant density, which results in final virial masses between 2.3×10^8 and $1.2 \times 10^9 M_\odot$. This corresponds to masses within 300 pc between 0.9×10^7 and $1.8 \times 10^7 M_\odot$, similar to those obtained by Strigari et al.. We nevertheless find a surprisingly large variation in stellar mass, luminosity, central mass-to-light ratio and metallicity, as summarised in Table 3.1. The final stellar masses range between 5.5×10^5 and $1.2 \times 10^7 M_\odot$, whilst the median iron abundance ranges from $[\text{Fe/H}] = -1.78$ to -1.12.

In Figure 3.11, we show that this is sufficient to reproduce the well-known mass-metallicity relation (e.g. Mateo, 1998) of dwarf spheroidals. We compare the results from our simulations, shown as red open squares, to those of 14 'classical' Local Group dwarf spheroidals, as given by Woo et al. (2008), overplotted as black triangles. We find that there is good agreement, both in the range of metallicities obtained, as well as in the slope of the relation, and that this is not affected by resolution.

We also show the distributions of metallicities of individual star particles per galaxy in Figure 3.12. Comparing this with observed distributions, e.g. by Helmi et al. (2006), we find an overabundance of both metal-rich and metal-poor
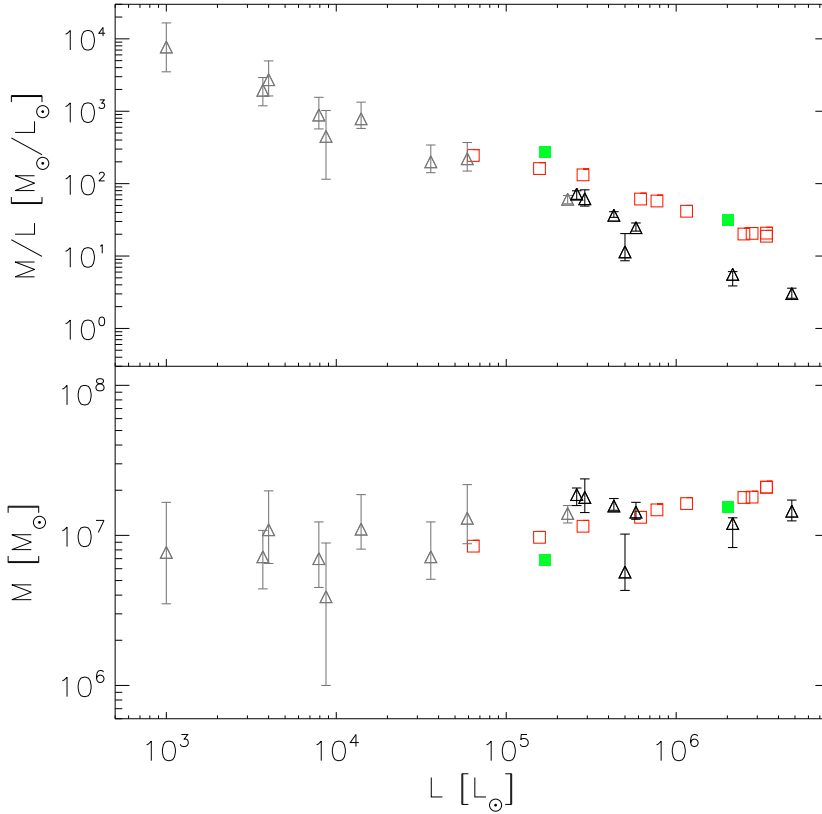
Figure 3.13: Mass-to-light ratio within 300 pc as a function of total luminosity. Simulations 1 through 9 from Table 3.1 and one additional, lower mass simulation are plotted as red squares, together with the 8 'classical' Milky Way satellites and the 10 'SDSS Dwarfs' contained in the analysis of Strigari et al., in black and grey triangles with error bars, respectively. The two filled, green squares are the results of two simulations with increased resolution discussed in Section 3.2.6.

stars for a given median metallicity. We attribute this to a lack of dissipative metal-mixing in the interstellar medium of our simulations. As a result, pockets of relatively metal-poor (or metal-rich) gas survive longer, and are able to form more stars of corresponding metallicity, which is reflected in a comparatively broad stellar metallicity distribution, as well as steeper negative metallictity gradients compared with observations.

In Figure 3.13 we compare the same set of simulations to observed Milky Way satellite galaxies in terms of their luminosities and mass-to-light ratios. The observational sample is identical to the one used by Strigari et al. (2008), and comprises 8 'classical' dwarf spheroidals, as well as 10 of the newly-discovered ultra-faint galaxies (Willman et al., 2005; Belokurov, 2007). While the observed galaxies span an even larger range in luminosity than the ones we have simulated, we find a similar, tight inverse correlation between luminosity and mass-to-light ratio. Whereas Strigari et al. find only a very weak dependence $M_{0.3} \propto L^{0.03 \pm 0.03}$, our relation is somewhat steeper at $M_{0.3} \propto L^{0.24}$. This is still a remarkably weak dependence, and it allows us to reproduce a large range in luminosity with an $M_{0.3}$ mass that varies by only a factor of two. As we discuss below, the remaining difference may point to the fact that our model does not yet include all physical effects, and that our assumption of an underlying mass distribution is not the full story. Strigari et al. also note that for the most luminous dwarf spheroidals such as Fornax, the mass-to-light ratios relating the mass within 300 pc to the total luminosity in the observed galaxies tend to be underestimates, since their stellar populations are typically more extended.

3.5.2 Kinematics

As shown in Table 3.1, the mean one-dimensional velocity dispersions in each galaxy resulting from our simulations are in the range of 6.5 to 9.7 kms^{-1}. This is comparable to the observed range of 7 to 10 kms^{-1} for six of the seven 'classical' Local Group dwarf spheroidals in the sample of Walker et al. (2007). The one exception, Fornax, has a velocity dispersion of about 12 kms^{-1}. Its stellar population, which includes several globular clusters, is more spatially extended, and its stellar mass is also slightly higher than that of the most luminous galaxy in our simulations. At the faint end, an extrapolation of our results might also be consistent with the corresponding values of the eight ultra-faint Milky Way satellites presented in Simon & Geha (2007), which have velocity dispersions between 3.3 and 7.6 kms^{-1}.

We also investigated the influence of supernova feedback on the shape of the dark matter distribution. It is still an open question whether flat cores, rather than the cusps predicted by dissipationless cold dark-matter models exist in the central regions of dwarf galaxy haloes. While for a stellar system with uniform

mass-to-light ratio, the shape of the gravitational potential can be uniquely determined from the observed velocity dispersion and surface brightness profiles, in the case of the highly dark-matter dominated dwarf spheroidal galaxies, the unknown mass-to-light ratios result in a degeneracy between the gravitational potential variation and the velocity anisotropy (Dejonghe & Merritt, 1992). The same data, when analysed with different anisotropy assumptions, can therefore result in different density profiles, and as van den Bosch & Swaters (2001) and Evans et al. (2009) have shown, the stellar kinematics of dwarf spheroidal galaxies are generally not sufficient to distinguish between cored and cusped profiles. Nevertheless, reports of central-density cores in dwarf galaxies (e.g. Carignan & Beaulieu, 1989; de Blok et al., 2001; Łokas, 2002) have been considered as evidence for warm dark-matter (e.g. Moore, 1994). Within the framework of ΛCDM, numerical simulations by Navarro et al. (1996), Read & Gilmore (2005), Mashchenko et al. (2008) and others have suggested that cores of kpc scale may form either as a result of dynamical coupling to supernova-induced bulk gas motions, or the rapid ejection of large amounts of baryonic matter. Our simulations fail to fulfil these requirements in two ways. The ejection of gas is not sufficiently rapid (which would also be difficult to reconcile with the observed age-spreads), and our dark matter haloes continue to evolve and grow after star formation and supernova rates have peaked, instead of simply settling to an equilibrium configuration. As a result, we do not observe the formation of cores in our runs with feedback. The final dark matter density distributions can be described by NFW-profiles up to the resolution limit.

3.5.3 Star Formation Efficiency

We have also run a number of simulations where we have varied the star-formation parameter $c_\star$, the constant of proportionality that enters the Schmidt law for the rate at which cold gas gets turned into stars (see Section 3.2.2). When the star formation is parametrised in this way in galactic chemical evolution models for late type galaxies, the choice of $c_\star$ has a strong influence on the star formation rate (Ferreras & Silk, 2001), and hence the stellar age distribution, as well as on the final stellar mass. We find no such strong influence in our simulated dwarf spheroidals, in agreement with Katz et al. (1996) and others. The star formation rate increases with $c_\star$ at all redshifts, and as a result, the final stellar mass scales as roughly $M_\star \propto c_\star^{0.25}$ over the range of $c_\star$ between 0.01 and 0.1. In the example of initial conditions identical to simulation 4 in Table 3.1, this corresponds to a range in final stellar masses of 2.3 to $4.2 \times 10^6 M_\odot$. This relatively weak dependence points to the fact that in dwarf galaxies, the main factor that determines the overall star formation is not the specific efficiency of turning cold gas into stars, but the amount of feedback and UV heating they can sustain before

star formation gets shut down, which in our models strongly depends on the depth of the potential.

There is nevertheless some degeneracy between star formation efficiency and halo mass when it comes to the amount of stars formed. This can be broken partially by considering chemical evolution. In Figure 3.11 we have included a simulation sequence of differing star formation efficiency but identical initial conditions, represented by blue diamonds, and we compare it to the observed mass-metallicity relation, as well as to the relation obtained from the sequence of simulations with varying total masses. Besides the much narrower range in stellar mass of the $c_\star$ sequence, its slope is also too steep when compared with observations, which in contrast, are well-matched by the varying mass sequence. While the amount of scatter prevents us from selecting a particular value of $c_\star$, it appears that the range in luminosities and the mass-metallicity relation cannot be explained by a simple scaling of the star formation efficiency. For most of our simulations, we have adopted a value of $c_\star = 0.05$, in agreement with Stinson et al. (2007) and Mashchenko et al. (2008).

3.5.4 Supernova-Progenitor Lifetimes

Our feedback model includes both supernovae type II and type Ia. The delay time of supernovae type II is theoretically constrained to be on the scale of Myrs, but due to the uncertain nature of their progenitors, that of supernovae type Ia is much more uncertain. We find that in our simulations, the bulk of the thermal feedback released in time to influence the star formation history is provided by supernovae type II. However, it has long been suggested (e.g. Burkert & Ruiz-Lapuente, 1997), that the slower type Ia supernovae feedback can influence the star formation in dwarf galaxies. In particular, the delay time for supernovae type Ia influences both the total iron enrichment, and the position of the turnover point on the $[\alpha/\text{Fe}]$ / $[\text{Fe/H}]$ diagram. In dwarf spheroidal galaxies with very short star formation episodes, this effect is particularly strong. In all simulations presented in this work, we assume a uniform delay time distribution with a maximum delay time of 1 Gyr. We have performed simulations with minimum delay times between 100 Myrs and several Gyrs, and found that once the minimum lifetime is increased above several hundred Myrs, the $[\alpha/\text{Fe}]$ ratios are too high, and there is no visible turnover point on the $[\alpha/\text{Fe}]/[\text{Fe/H}]$ diagram, contrary to the observed distribution of red giants in Local Group dwarf spheroidals (e.g. Shetrone et al., 2003; Tolstoy et al., 2003).

The two scenarios are illustrated in Figure 3.14, which shows the $[\text{Ca/Fe}]$ ratios for minimum lifetimes of 10^8 years (upper panel) and 5×10^8 years (lower panel) in two simulations with initial conditions identical to simulation 2 in Table 3.1 that both have an age-spread of ~ 1.1 Gyrs. With a more careful analysis and
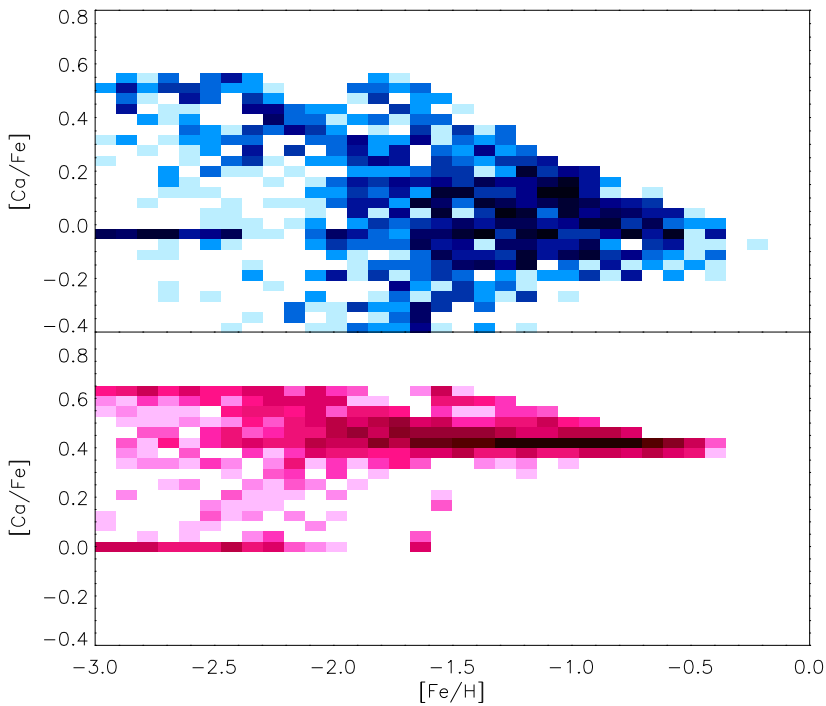
Figure 3.14: Abundance ratios of [Ca/Fe] vs [Fe/H] of the stars, in simulations with a minimum supernova Ia lifetime of 10^8 years (top) and 5×10^8 years (bottom). The distribution shown on top is for simulation 1, and shows the characteristic drop due to the transition from pure type II to type Ia element ratios. The second simulation is identical to simulation 1 in all other parameters, but due to the increased lifetime of the SN type Ia progenitors, the relative abundances remain fixed at the SN type II ratios.

better constraints on other aspects of the chemical evolution model, such as the mixing of elements, the initial mass function and the yields, those dwarf spheroidal galaxies which show evidence for enrichment by type Ia supernovae despite an apparently short star-forming phase might therefore provide an upper bound on the minimum lifetime of supernova type Ia progenitors. On the other hand, we are satisfied that allowing the lifetime to be a 'free parameter' of the model, the best fit to the observations is obtained with a minimum lifetime of around 100 Myrs, compatible with the value suggested by Matteucci & Recchi (2001).

3.6 Summary

We have studied the formation and evolution of dwarf galaxies with halo masses in the range of $\sim 2 \times 10^8$ to 10^9 M$_\odot$ in full cosmological simulations including cooling, supernova feedback and UV radiation. Our models have resulted in the formation of galaxies similar to the Local Group dwarf spheroidals. They span a wide range in luminosity, 6.4×10^4 to 3.4×10^6 L$_\odot$ and median metallicity, from [Fe/H]$= -1.83$ to -1.12. The variation in total mass, 2.3 to 11.8 $\times 10^8$ M$_\odot$, is surprisingly small, but it is comparable to the values inferred from observations in the Local Group. The range of velocity dispersions, 6.5 to 9.7 kms^{-1}, is also in good agreement with the observed range. Our simulations have resulted in two kinds of age distributions, either a single burst of star formation lasting around 1 Gyr, or a burst followed by a tail extending over several Gyrs. Both of these have Local Group analogues. However, in some sense the sample of dwarf spheroidal galaxies in the Local Group is even more diverse. Our limited set of initial conditions did not produce a system as luminous and extended, or with such a large age-spread as Fornax, nor were we able to resolve systems as faint as some of the ultra-faint dwarf galaxies.

We have shown that in our simulations, feedback from supernovae and the cosmic UV background shape both the dynamical and the chemical evolution of dwarf spheroidal galaxies. As a result, these are inseparably linked, which is reflected in the scaling laws such as the mass-metallicity relation. Feedback is essential for the evolution of all galaxies in our models, while additional UV radiation is required to reproduce the full range of observed galaxies, particularly those which only have a short burst of star formation. We have demonstrated that, with a sensible choice of parameters, the formation of systems comparable to Local Group dwarf spheroidal galaxies is possible. While we stress that we do not suggest that the dwarf spheroidal population in the Local Group reflects merely a variation in halo mass, we conclude that it is possible to reproduce the wide range of observed stellar masses and metallicities, as well as differing star formation histories within a single evolutionary scenario, and for a narrow range

of dynamical masses, as observed.

Our simulations put the Local Group dwarf galaxies in a unique position where the gravitational potential is at a critical value with respect to the combined effects of supernova feedback and UV heating. We find that both are necessary to reproduce the observations. In this scenario, a number of dynamical and stellar evolution effects conspire to reproduce the observed scaling relations. More massive galaxies start off with a proportionally higher initial gas mass, and in addition turn a larger fraction of it into stars, because their deeper potential wells moderate supernova-driven outflows and also allow the gas to self-shield against the UV background. On top of that, more efficient recycling of the gas leads to higher metallicities, and a more extended star formation history results in a younger stellar population with higher specific luminosities. While all these effects undoubtedly play a role in the real systems, differing assembly and accretion histories, and differing environments are likely also to influence dwarf spheroidal structure.

With regard to the 'laboratory' characteristics of dwarf spheroidals mentioned in our introduction and underlined by our results, as well as in view of the enormous difference in scale compared with the disk galaxies studied by Scannapieco et al. (2008), the addition of low-temperature cooling and self-shielding has relatively minor effects. It is a noteworthy and reassuring result that the same numerical model effectively works for both kinds of galaxies. Our models do not yet include the mixing of elements in the interstellar medium. In addition, their environment differs from the Local Group, where environmental effects are clearly reflected in relations such as the apparent dependence of star-formation timescale on Galactic distance (van den Bergh, 1994; Grebel, 1997). Nevertheless, it remains to be seen how important they are compared to feedback and the UV background. Our choice of initial mass function has produced a residual population of metal-free stars in the simulations, which are not observed. The inclusion of early enrichment by Population III stars might remove this discrepancy. Simulations by Wise & Abel (2008) have recently studied how massive Population III stars, and the resulting photoionization at redshifts ~ 30 may affect the interstellar medium in dwarf galaxies. This would be an interesting addition to our models. Addressing these issues should lead to a more complete understanding of the evolution of dwarf galaxies, and should also allow us to make more detailed comparisons with individual objects, exploiting the high quality data that have become available in recent years.

Table 3.1: Overview of numerical simulation results for isolated dwarf galaxies

Label	f_s	$M_\star$ $[10^6 M_\odot]$	M_g $[10^6 M_\odot]$	M_{tot} $[10^6 M_\odot]$	$M_{0.3}$ $[10^6 M_\odot]$	$M_{1.8}$ $[10^6 M_\odot]$	$M/L_{0.3}$ $[M_\odot/L_\odot]_V$	$M/L_{1.8}$ $[M_\odot/L_\odot]_V$	$r_{1/2}$ [pc]	Δ_{age} [Gyrs]	[Fe/H]	σ $[\text{kms}^{-1}]$
Simulations including feedback, UV radiation and self-shielding[1]												
1	0.368	0.55	0.099	233.8	8.48	79.0	129	555	244	1.13	-1.78	6.55
2	0.422	0.96	0.005	348.8	9.71	103.6	100	409	303	1.15	-1.76	7.26
3	0.464	2.10	0.009	466.1	11.5	125.7	39	223	226	2.51	-1.52	7.54
4	0.500	2.68	0.006	585.3	13.2	147.3	39	209	246	1.78	-1.54	8.12
5	0.531	3.94	0.14	701.8	14.8	165.9	26	156	212	1.21	-1.46	8.47
6	0.559	9.02	0.010	809.3	16.3	185.7	13	81	164	3.10	-1.12	8.62
7	0.585	10.02	0.005	922.3	17.9	203.5	13	80	171	3.23	-1.17	9.08
8	0.608	12.20	0.011	1042	17.9	218.5	12	71	190	3.30	-1.15	9.62
9	0.630	12.26	0.012	1162	21.0	235.1	14	76	181	3.21	-1.14	9.71
Simulations including UV radiation but no supernova feedback[1] [3]												
10	0.422	18.77	0.82	318.4	14.5	113.3	8	28	118	3.75	-0.71	-
11	0.531	99.50	9.64	645.6	27.0	216.5	6	14	160	6.46	-0.21	-
Simulations including feedback, UV radiation but no shielding[1]												
12	0.368	0.53	0.002	233.2	8.40	79.2	129	571	271	1.09	-1.78	6.39
13	0.422	0.99	0.005	351.7	10.3	103.8	98	407	289	1.11	-1.70	7.43
14	0.464	1.95	0.015	463.8	11.6	126.0	48	240	254	1.11	-1.52	7.67
15	0.500	2.75	0.19	582.7	13.5	148.1	38	201	248	1.16	-1.48	8.31
16	0.531	4.19	0.20	697.8	15.5	168.6	27	152	208	1.17	-1.38	8.40
17	0.559	6.91	0.55	811.2	16.6	187.6	17	105	186	1.14	-1.27	8.45
18	0.585	6.69	0.38	939.4	18.0	202.6	18	113	180	1.21	-1.29	9.12

Continued on next page...

Table 3.1 – Continued

Label	f_s	$M_\star$ [$10^6 M_\odot$]	M_g [$10^6 M_\odot$]	M_{tot} [$10^6 M_\odot$]	$M_{0.3}$ [$10^6 M_\odot$]	$M_{1.8}$ [$10^6 M_\odot$]	$M/L_{0.3}$ [$M_\odot/L_\odot$]$_V$	$M/L_{1.8}$ [$M_\odot/L_\odot$]$_V$	$r_{1/2}$ [pc]	Δ_{age} [Gyrs]	[Fe/H]	σ [kms^{-1}]
19	0.608	9.31	0.58	1051	18.1	217.9	15	89	197	1.18	-1.32	9.38
20	0.630	9.65	0.65	1179	18.9	235.2	16	93	196	1.12	-1.31	9.74

Simulations including feedback but no UV radiation[1]

Label	f_s	$M_\star$	M_g	M_{tot}	$M_{0.3}$	$M_{1.8}$	$M/L_{0.3}$	$M/L_{1.8}$	$r_{1/2}$	Δ_{age}	[Fe/H]	σ
21	0.368	1.38	0.077	229.6	9.08	79.24	36	202	180	7.96	-1.09	6.28
22	0.422	2.58	0.10	344.2	11.8	105.3	27	143	180	7.60	-1.03	7.11
23	0.464	4.58	0.08	458.4	13.4	128.6	19	105	178	5.49	-1.08	7.39
24	0.500	5.72	0.11	576.2	15.4	150.3	18	99	165	5.25	-1.06	8.17
25	0.531	7.14	0.098	685.9	16.3	158.5	16	90	171	4.53	-1.08	8.33
26	0.559	9.26	0.086	798.5	17.4	186.9	14	81	157	2.59	-1.12	8.75
27	0.585	10.95	0.064	909.0	17.5	204.3	13	76	169	3.66	-1.05	9.17
28	0.630	13.70	0.003	1147	20.1	236.9	12	69	181	3.71	-1.09	10.0

Simulations including feedback, UV radiation and self-shielding[2]

Label	f_s	$M_\star$	M_g	M_{tot}	$M_{0.3}$	$M_{1.8}$	$M/L_{0.3}$	$M/L_{1.8}$	$r_{1/2}$	Δ_{age}	[Fe/H]	σ
29	0.422	0.59	0.008	338.7	6.88	104.1	157	737	375	1.21	-1.78	7.20
30	0.630	7.35	0.066	1141	15.5	235.4	18	133	245	2.62	-1.11	9.50

Notes: Col. 2: Scale factor (length) of the initial conditions relative to Hayashi et al. (2004), Col. 3: Stellar mass, Col. 4: Gas mass within 1.8 kpc, Col. 5: Halo mass (M_{200}), Col. 6: Dark matter mass within 0.3 kpc, Col. 7: Dark matter mass within 1.8 kpc, Col. 8: Mass-to-light ratio (V-Band) within 0.3 kpc, Col. 9: Mass-to-light ratio (V-Band) within 1.8 kpc, Col. 10: Half light radius (projected), Col. 11: Formation time interval containing 90 % of $M_\star$, Col. 12: Median stellar iron abundance, Col. 13: RMS stellar velocity dispersion
Remarks: [1] Initial number of particles: 1.7×10^5 gas, 8.7×10^5 dark matter. [2] Initial Number of particles: 1.21×10^6 gas, 2.83×10^6 dark matter. [3] Simulations terminated at $z = 0.68$.

4 The Formation of the Local Group Dwarf Galaxies

We investigate the formation and evolution of dwarf galaxies in a high resolution, hydrodynamical cosmological simulation of a Milky Way sized halo and its environment. Our simulation includes gas cooling, star formation, supernova feedback, metal enrichment and UV heating. In total, 90 satellites and more than 400 isolated dwarf galaxies are formed in the simulation, allowing a systematic study of the internal and environmental processes that determine their evolution. We find that 95% of satellite galaxies are gas-free at $z = 0$, and identify three mechanisms for gas loss: supernova feedback, tidal stripping, and photo-evaporation due to re-ionization. Gas-rich satellite galaxies are only found with total masses above $\sim 5 \times 10^9 \mathrm{M}_\odot$. In contrast, for isolated dwarf galaxies, a total mass of $\sim 10^9 \mathrm{M}_\odot$ constitutes a sharp transition; less massive galaxies are predominantly gas-free at $z = 0$, more massive, isolated dwarf galaxies are often able to retain their gas. In general, we find that the total mass of a dwarf galaxy is the main factor which determines its star formation, metal enrichment, and its gas content, but that stripping may explain the observed difference in gas content between field dwarf galaxies and satellites with total masses close to $10^9 \mathrm{M}_\odot$. We also find that a morphological transformation via tidal stripping of infalling, luminous dwarf galaxies whose dark matter is less concentrated than their stars, cannot explain the high total mass-to-light ratios of the faint dwarf spheroidal galaxies.

4.1 Introduction

In Chapter 3, it was shown that dark matter-dominated, early type dwarf galaxies comparable to the Local Group dwarf spheroidals (see Chapter 1 for a complete characterisation) *can* form in isolation through the processes of supernova feedback and UV radiation, which regulate and eventually quench star formation, and eject most of the interstellar gas. In particular, it was found that the dependence of the efficiency of both effects on the depth of the gravitational potential can explain the observed scaling relations between total and stellar mass (Figure 3.13) and between stellar mass and metallicity (Figure 3.11).

An alternative scenario for the formation of dwarf spheroidal galaxies involves the transformation of gas-rich, more luminous dwarf-irregular galaxies into the gas-free, low-luminosity early type galaxies via environmental effects, namely ram pressure and tidal stripping.

Ram pressure refers to the pressure exerted on the interstellar gas of a satellite galaxy as it passes through the hot intergalactic medium in a dense environment (Einasto et al., 1974). Ram-pressure stripping affects the interstellar gas, but not the stars or dark matter. While this mechanism is observable in galaxy clusters, estimates of the gas density of the Milky Way halo (e.g. Murali, 2000) show it to be several orders of magnitude too low for ram pressure stripping to be efficient (Mayer et al., 2001). Tidal perturbations are caused by the differential gravitational acceleration across the diameter of a satellite as it orbits the main halo. They affect gas, stars and dark matter alike, and can alter the internal kinematics and morphology of the satellite ("tidal distortion"), as well as remove mass from the objects ("tidal stripping"). Tidal stripping can still change the composition of objects, if the spatial distribution of the components differ. Clear observational evidence for tidal stripping within the Milky Way halo is provided by the presence of tidal streams (e.g. Johnston et al., 1999, now also observed around other galaxies). These elongated substructures consist of stars that were tidally unbound from satellite galaxies, and deposited along their orbits.

Numerical simulations (Mayer et al., 2001, 2006; Klimentowski et al., 2009) have shown that tidal stripping by an external potential like that of the Milky Way halo can indeed transform an evolved, disk-like dwarf galaxy into a less luminous, early type dwarf galaxy. Evidence for environmental effects is also provided by the observed relations between galactocentric distance and the duration of star formation in classical dwarf spheroidals (Grebel, 1997), and between distance and HI masses of early type dwarf galaxies in the Local Group (Blitz & Robishaw, 2000; Grebel et al., 2003), as shown in Figure 1.2.

Most present day dwarf spheroidals, however, show no sign of tidal distortion in their stellar kinematics (Walker et al., 2007), indicating that strong tidal interactions would have had to be limited to their past. Models in which similar

mass late type progenitors are transformed into different mass dwarf spheroidals based on orbital parameters alone, may have difficulty in explaining the strong-mass metallicity scaling relation (Grebel et al., 2003). Most dwarf spheroidals also show metallicity gradients, which are reproduced in simulations where star formation is regulated by internal processes (Revaz et al., 2009), but are not typically found in dwarf irregulars, and may not be preserved during strong tidal stirring.

Comparisons of early type dwarf galaxies, in the Virgo cluster (Michielsen et al., 2008), and the Fornax cluster (Koleva et al., 2009), both to field dwarf galaxies, found no clear difference between the environments. Recently, comparing Coma cluster dwarf galaxies to dwarf galaxies in poor groups, Annibali et al. (2010) reported that dwarf galaxies in low-density environments may experience more prolonged star formation, evidence that the morphology-density relation also extends to dwarf galaxies. It should be also be emphasised, that even if the environmental correlation is weak, external effects could still play an important role, if the responsible mechanisms are also efficient in low-density environments.

Two isolated dwarf spheroidal galaxies, Cetus (Whiting et al., 1999) and Tucana (Lavery & Mighell, 1992), have been discovered in the Local Group, with distances of 780 ± 40 kpc and 890 ± 50 kpc, respectively (Bernard et al., 2009). Deep observations and modelling of the stellar populations by Monelli et al. (2010) suggests that these presently isolated objects are similar to oldest Milky Way dSph satellites; in contrast to the morphology-distance relation, and implying a formation mechanism independent of environment. However, it is not known whether present isolation also implies isolated evolution.

So far, simulations have largely separated internal and external mechanisms, by either investigating the formation of isolated dwarf galaxies (Stinson et al., 2007; Valcke et al., 2008; Revaz et al., 2009; Sawala et al., 2010), or the transformation of evolved objects in an external gravitational potential (Mayer et al., 2001, 2006; Klimentowski et al., 2009). In reality, all effects are simultaneously present in the Local Group. In this chapter, results from *Aquila* simulation are presented, which includes the formation of a Milky Way sized galaxy and its environment in a fully cosmological context of a ΛCDM universe. The satellites that grow and evolve are thus subject to tidal forces, but also all astrophysical processes associated with cooling, star formation, supernova feedback and UV heating. This simulation allows us to study all these effects in a consistent manner, and to compare their relative importance for the evolution of each object individually, as well as for the ensemble of the Milky Way satellites.

This chapter is organised as follows: Section 4.2 contains a description of the initial conditions for the simulation, the numerical methods, and the method for the identification of substructure. Section 4.3 describes the formation and

time evolution of the halo along with its substructures. In Section 4.4 we take a closer look at the different mechanisms for gas removal in individual satellites. Section 4.6 summarises the statistical properties of the present-day satellite population and the derived scaling relations. In Section 4.7, we also compare the population of satellites to the population of isolated dwarf galaxies formed in the same simulation. The chapter concludes with a summary in Section 4.8.

4.2 The Aquila Simulation

The Aquila simulation was set up and run by C. Scannapieco, with the principal aim of studying the formation of disk galaxies in a ΛCDM universe. The results presented here are based on simulation "AQ-C-5" of Scannapieco et al. (2009), which resulted in the formation of a Milky Way sized disk galaxy. For the purpose of this work, the focus is on the formation and evolution of the $\sim$90 satellites of the central galaxy, and the isolated dwarf galaxies that form in the environment.

4.2.1 Initial Conditions

The initial conditions used here are based on one of several haloes (labelled halo "C"), which were extracted from the Millennium II simulation, and resimulated with pure dark matter in the *Aquarius* project (Springel et al., 2008). The cosmological parameters are identical to those of the Millennium simulations, $\Omega_m = 0.25, \Omega_\Lambda = 0.75, h = 0.73$ and $\sigma_8 = 0.9$, consistent with WMAP-1 cosmology. The simulation is performed with periodic boundary conditions in a box of side length 137 Mpc ($100h^{-1}$ Mpc in comoving coordinates). Similar to the resimulations described in Chapter 5, the central Lagrangian region is filled with an equal number of high resolution dark matter and gas particles, at a mass ratio of $\Omega_{DM} = 0.21$ to $\Omega_b = 0.04$. Particle masses in the level 5 *Aquila* simulation are $2.6 \times 10^6 M_\odot$ for dark matter and 2–$4 \times 10^5 M_\odot$ for gas particles. Star particles which form have a mass of 1–$2 \times 10^5 M_\odot$. A comoving softening of 1 kpch^{-1} is used. Note that despite the limited accuracy of gravitational forces at the softening scale, tidal accelerations due to an external potential are almost unaffected by the softening.

4.2.2 Computational Methods

The simulations are performed with the smoothed particle hydrodynamics code GADGET-3 (Springel, 2005; Springel et al., 2008), together with the star formation and feedback model of Scannapieco et al. (2005, 2006). The same model is also used in the simulations presented in Chapters 3 and 5, and a more detailed description is given in Section 3.2. Specific to this simulation, a star formation

parameter of $c_\star = 0.1$ is used, whereas most simulations presented in Chapter 3, and all simulations of Chapter 5 use a value of $c_\star = 0.05$. Section 3.5 contains a discussion of the effect of varying $c_\star$. The energy per supernova is set to 0.7×10^{51} ergs, identical to the value of Chapter 5, but slightly lower than the value of 1.0×10^{51} ergs used in Chapter 3. The energy and metals are distributed equally between the hot and cold gas phases. The cooling model is based on Sutherland & Dopita (1993), with metal-dependent cooling above $10^4 K$, and the UV heating mechanism is implemented following Haardt & Madau (1996). Self-shielding (described in Section 3.4.3) and "seeding" (described in Section 5.4.5) are not used here. However, we do not expect this to significantly alter the results.

The mass resolution of the Aquila simulation is several hundred times lower than what can be achieved in simulations of individual dwarf galaxies like those presented in Chapters 3 and 5. Primarily, this is attributable to the much larger Lagrangian volume, but the presence of a large galaxy with its high cold gas fraction and specific star formation rate also increases the computational cost per particle. As a result, the properties of individual dwarf galaxies are not resolved with the same level of detail. Still, the large number of satellites that form allow a number of statistical comparisons. In addition, the fact that the same astrophysical and numerical models are used in the high resolution simulations presented Chapters 3 and 5 allows a direct comparison and an estimation of the effects of resolution. A full simulation with an 8 times higher mass resolution is currently being performed, which will allow for somewhat more detailed statements, as well as to resolve even fainter satellite galaxies.

The Aquila project also includes a comparison of different hydrodynamical models. Okamoto & Frenk (2009); Okamoto et al. (2010) and Wadepuhl & Springel (2010) have used the same initial conditions, coupled to different models of astrophysical effects. The star formation and feedback model of Wadepuhl & Springel (2010) is based on Springel & Hernquist (2003), combined with a black hole wind model and a model for cosmic rays. They conclude that cosmic rays, or some other mechanisms in addition to thermal supernova feedback and UV heating are necessary in order to bring the satellite luminosity function in agreement with observations. Our results agree qualitatively with their simulations including cosmic rays, indicating that the supernova feedback strength varies between the models. Okamoto et al. investigate the result of varying the effect of feedback on the star forming gas. They show that stellar mass and metallicity scale strongly with circular velocity (i.e. subhalo mass), and conclude that a threshold established by re-ionization results in the small fraction of visible satellite galaxies populating a much larger number of satellite subhaloes. Neither study investigates the *isolated* dwarfs and compares them to the satellites, which is the focus of this chapter.

4.2.3 Identification of Substructure

In each snapshot, haloes are identified in a two step process using a Friends-of-Friends (FoF) algorithm. The FoF groups are defined first by linking only the dark matter particles. In a second step, star and gas particles are linked to the particles already belonging to these groups in the same way. In the Aquila simulation, the larger haloes, and in particular, the main halo that will become the host of the "Milky Way" galaxy, also contain a number of gravitationally bound, over-dense substructures called *subhaloes*, which are identified using the SUBFIND algorithm of Springel et al. (2001). For each FoF halo, SUBFIND begins by computing a smoothed local density by an SPH-interpolation over all particles of the halo. A potential substructure is first identified as a local overdensity with respect to this smooth background density. It is then subjected to gravitational unbinding, whereby all unbound particles are iteratively removed, until the substructure either vanishes, falling below the threshold of 20 particles, or is identified as a genuine self-bound subhalo.

In order to trace subhaloes over time between different snapshots, the 20 most bound dark matter particles of each subhalo in a given snapshot were compared to the list of particles in all subhaloes of the previous snapshot, identifying as the progenitor the subhalo that contained at least 11 of the 20 particles amongst its 20% of most bound particles. The process is repeated until a progenitor is no longer found, and we define this as the time of *formation*. If the subhalo can be linked to a subhalo in a previous snapshot, but not to its most bound particles, we consider the progenitor to have fragmented, and define this as the time of *fragmentation*. Fragmentation can be due to the breaking-up of larger haloes, or to the amplification of substructures above the particle threshold, without the newly identified subhaloes hosting galaxies. In Table 4.1, fragmentation is indicated with an asterisk next to the formation redshift. We note that a large majority of subhaloes of satellite galaxies can be traced back as independent objects well beyond $z = 6$.

Most of the subhaloes belonging to the main halo at $z = 0$ belong to different groups at earlier times. We call the time when a subhalo is *first* identified as a subhalo of the main halo the time of *infall*, noting that some subhaloes subsequently become transitorily isolated, and fall in again at a later time.

For consistency with the previous chapters, the term *halo mass* and *subhalo mass* will sometimes be used interchangeably when referring to the total mass of a satellite subhalo. Conversely, when the mass of the host halo is considered, this will be stated explicitly. When referring to a given set of "subhaloes", the central and dominant subhalo which contains the Milky Way galaxy is generally omitted for the remainder of this chapter.

4.3 Time Evolution of the Aquila Simulation

Figures 4.1, 4.2 and 4.3 respectively show the time evolution of the projected dark matter, gas and stellar mass distributions in the central region of the simulation. Each panel is centred on the position of the main subhalo (which is the host of the "Milky Way"), and shows all particles within a cubic volume of side length 1 Mpc At each redshift, the X, Y and Z-coordinates are defined parallel to the principal moments of the inertia tensor of the halo, with eigenvalues $I_x > I_y > I_z$. Keeping the volume fixed in comoving coordinates corresponds to a zoom-out in physical coordinates by a factor of 7.5 as the universe grows with time from $z = 6.5$ to $z = 0$. The squares indicate the position of all satellite subhaloes belonging to the main FoF halo identified at the time of the snapshot, with the size of the squares in all figures indicative of (but not strictly proportional to) the dark matter mass of the subhalo.

In Figure 4.2, where the blue colour indicates gas density, red boxes denote the subhaloes that contain gas, while white boxes denote subhaloes that are gas-free. It can be seen that even at high redshifts, the majority of subhaloes are gas-free, and only four relatively massive satellites contain gas at $z = 0$. The smallest of these four satellites, which are the subject of Section 4.5.1, has a total mass of $\sim 5 \times 10^9 \mathrm{M}_\odot$. All lower mass satellites, many of which formed stars, have lost their gas during their evolution. The different mechanisms of gas loss, internal and environmental, are discussed in Section 4.4.

In Figure 4.3, the green colour shows the stellar density, which is clearly dominated by the central object and its halo. Here, red boxes show subhaloes that contain stars, while white boxes show haloes that are essentially dark. At $z = 0$, there are 90 subhaloes containing stars, including the four which contain gas, as shown in Figure 4.2. The highest mass subhalo that does not contain any stars at $z = 0$ has a mass of $4.3 \times 10^8 \mathrm{M}_\odot$. The lower mass limit for star formation becomes difficult to assess, because of the limited resolution of our simulation. The total number of subhaloes with stars is comparable, however, with observational estimates of the number of dwarf satellites around the Milky Way.

The halo reaches a final virial mass of $1.6 \times 10^{12} \mathrm{M}_\odot$, comparable to recent observational estimates of the Milky Way halo, for example $10^{12} \mathrm{M}_\odot$ (Xue et al., 2008), $1.4 \times 10^{12} \mathrm{M}_\odot$ (Smith, 2007), $1.6 \times 10^{12} \mathrm{M}_\odot$ (Gnedin et al., 2010) and $2.4 \times 10^{12} \mathrm{M}_\odot$ (Li & Helmi, 2008). The corresponding spherical virial radius is ~ 250 kpc, but we include as satellites all subhaloes within the FoF group. 40% of the satellites are presently located outside of r_{vir}, with the furthest satellite at a galactocentric distance of 490 kpc. The central galaxy reaches a stellar mass of $10.8 \times 10^{10} \mathrm{M}_\odot$, higher than current observational estimates for the Milky Way, for example $5.5 \times 10^{10} \mathrm{M}_\odot$ from (Flynn et al., 2006). Distributions of the different mass components, and the positions of all satellites at $z = 0$ are shown in three orthogonal projections along
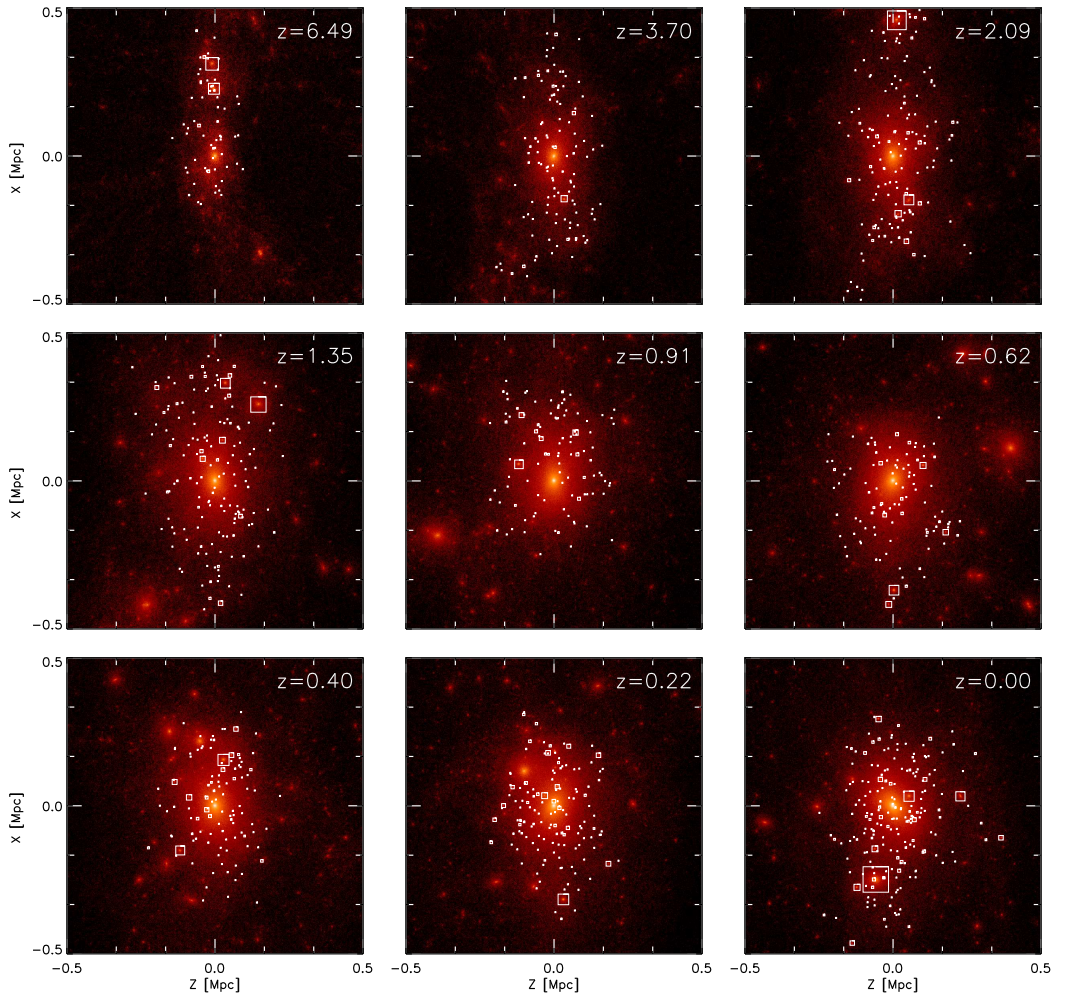
Figure 4.1: Evolution of the dark matter distribution in the central region of the Aquila simulation. Each panel shows a box of sidelength 1 Mpc (co-moving), centred on the central subhalo, and oriented along the major (X) and minor (Z) component of the inertia tensor of the main halo. The squares show the position of identified subhaloes belonging to the FoF-group of the main halo present at each snapshot, with the area proportional to the subhalo mass. Over time, the distribution of mass and of subhaloes changes from an elongated distribution at high redshift to a more rounded distribution at lower redshift (different projections of the subhaloes at $z = 0$ are shown in Figure 4.4).
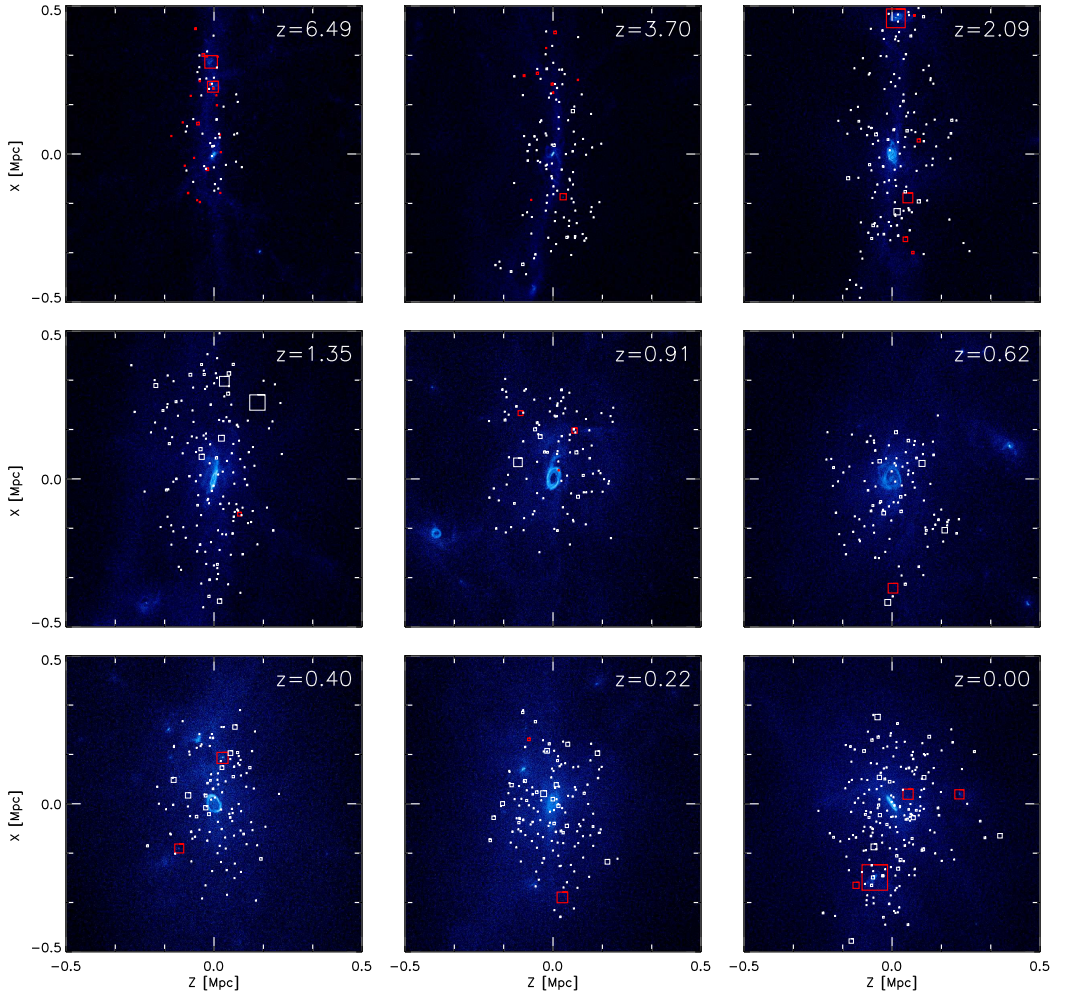
Figure 4.2: Gas distribution in the central region of the Aquila simulation at different redshifts, in volumes identical to Figures 4.1 and Figures 4.3. Subhaloes of the main FoF halo with gas are shown as red squares, Gas-free subhaloes are shown in white. While most satellites contain gas at $z = 7$, this fraction drops significantly, and only four of the most massive satellites are not gas-free at $z = 0$.
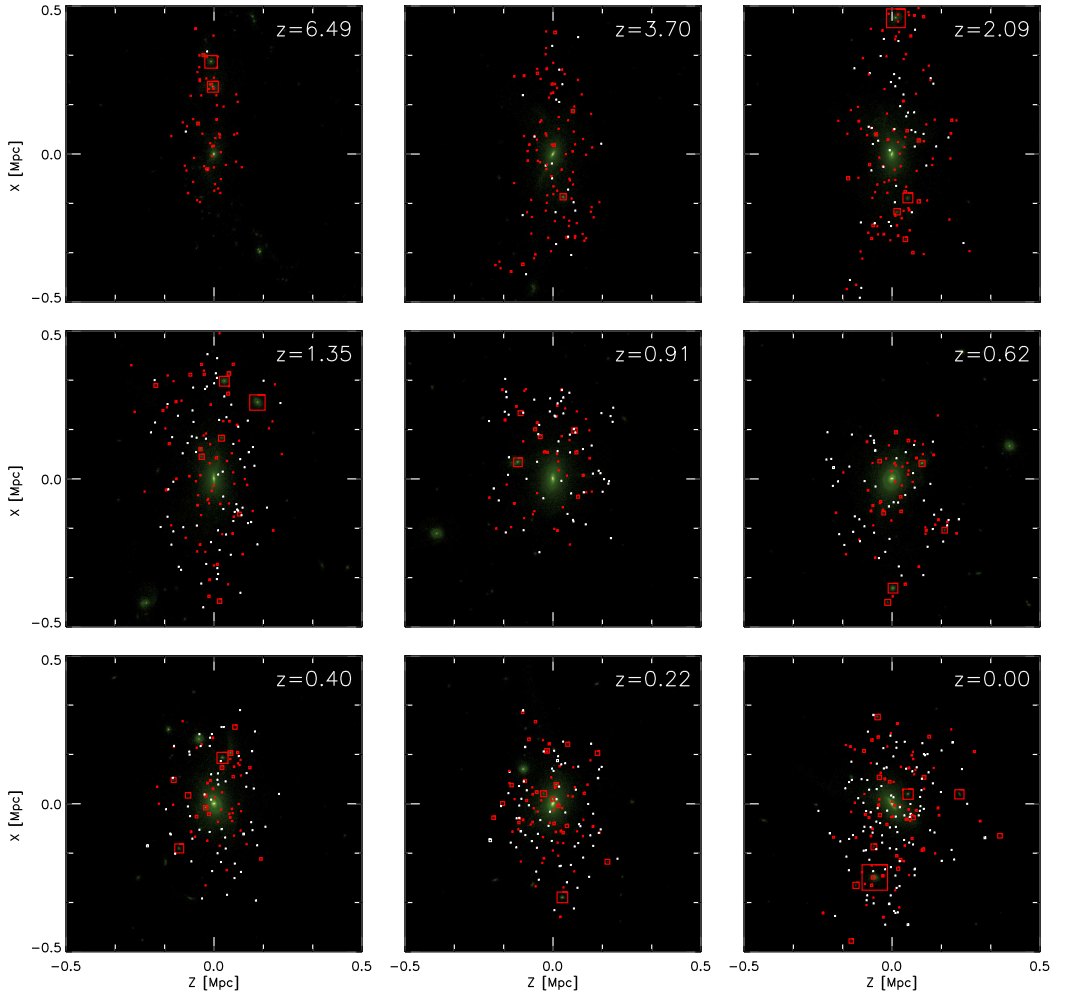
Figure 4.3: Stellar mass distribution in n the central region of the Aquila simulation at different redshifts, in volumes identical to Figures 4.1 and Figures 4.2. The central, Milky Way type galaxy dominates the total stellar mass at every redshift. The positions of satellite galaxies are shown in red, while dark subhaloes are shown as white squares. The size of each square corresponds to the dark matter mass of each subhalo. While nearly all subhaloes present at $z = 7$ also contain stars, the fraction drops to $\sim 45\%$ at $z = 0$, with more massive subhaloes more likely to contain stars.
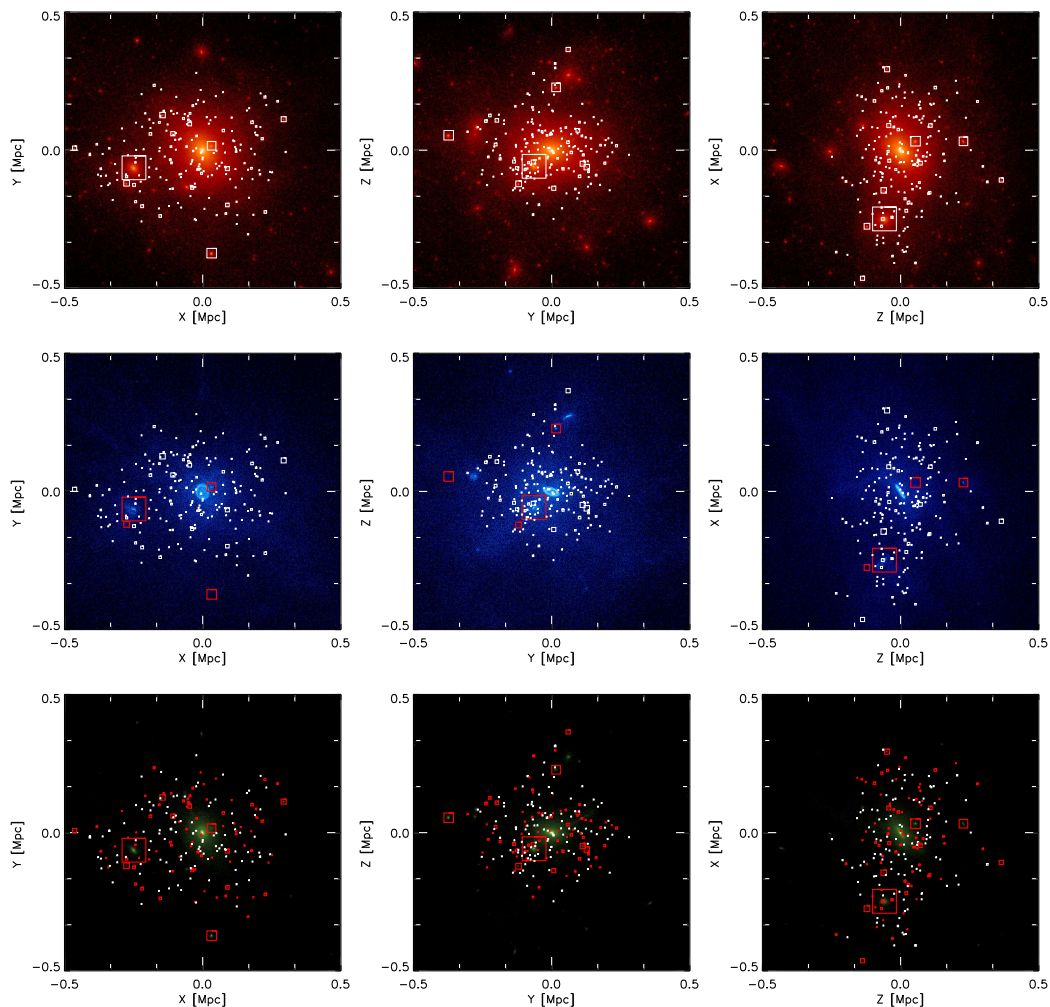
Figure 4.4: Projections of the dark matter (top), gas mass (middle) and stellar mass (bottom) distributions at $z = 0$, with the location of subhaloes overplotted as squares. As in Figures 4.1 – 4.3, the size of the squares indicate the dark matter mass of each subhalo. Analogous to Figure 4.2 and 4.3, in the middle row, red and white squares distinguish satellites which have gas from those that are gas-free, while in the bottom row, the distinction is between subhaloes with and without stars. Notable from the middle row is the pair of late-infalling, gas-rich satellites 1 and 7, as described in Section 4.5.1 .

the principal axes of the inertia tensor of the halo in Figure 4.4. By comparison with the flattened distribution seen at high redshift, the final shape of the halo appears round and largely featureless. This transformation from a triaxial mass distribution, expected from purely gravitational assembly, to an oblate halo similar to that observed, is also studied in Tissera et al. (2010), who attribute the difference to baryonic effects.

4.4 Formation and Evolution of Satellites

When the environment is included, different mechanisms of gas loss can play a role, and all are observed in the simulation. The internal and external mechanisms often act simultaneously, and are not always easy to disentangle. Just as the supernova heating aids in the gas removal by UV radiation, discussed in Chapter 3, the thermal expansion caused by the energy input can also make gas more easily lost by tidal interactions. In section 4.4.1, we discuss four exemplary cases of gas loss which are representative of the total subhalo population in terms of their final properties, but where the different mechanisms are relatively easily identified. Section 4.5 considers two extreme cases of subhaloes very heavily affected by stripping. Section 4.5.1 describes four satellites that still contain gas at $z = 0$, and contrasts them to the many gas-free satellites.

4.4.1 Gas Loss by Example

In the top panel of Figure 4.5, we show the evolution of the three mass components, dark matter (black), gas (blue) and stellar mass (green) of 4 selected subhaloes, each representing a different formation scenario. Also shown in the bottom panel of Figure 4.5 is the distance to the centre of mass to the main halo as a function of redshift.

- In the top left in Figure 4.5 is subhalo 14. Here, the gas is blown out by the combined effect of supernova feedback and UV heating, while the dwarf halo is still in isolation. As it approaches the central halo, some gas is re-acquired at $z \sim 3.5$, but this does not lead to renewed star formation. This residual gas is lost when the dwarf halo finally falls in to the central halo at $z = 2.1$. As it spirals inwards on multiple orbits, the dark matter mass decreases from its peak of $2.4 \times 10^9 M_\odot$ to its $z = 0$ value of $1.3 \times 10^9 M_\odot$. On the final two passages, the stellar mass also decreases slightly.

- In the top right, subhalo 23 loses its gas already at high redshift while still in isolation, similar to subhalo 14. It evolves passively and gas-free from $z = 3$ onwards, falling into the main halo at $z = 1.53$. The dark matter mass and stellar mass are not significantly affected after infall up to $z = 0$.
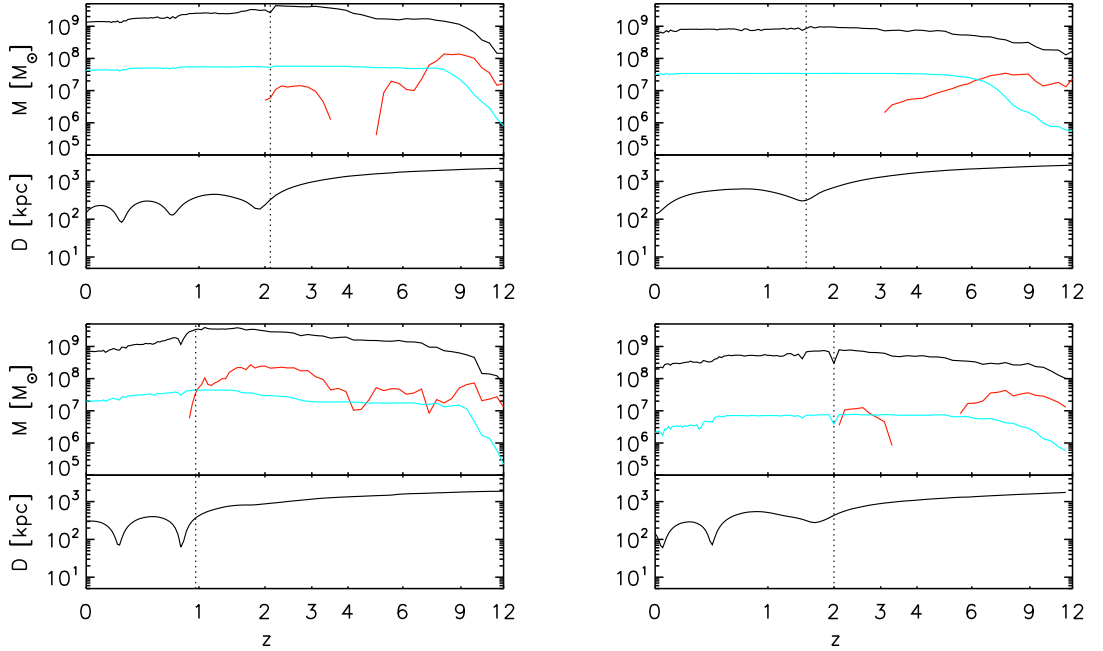
Figure 4.5: Evolution of the mass components (top) and distance to the centre of the central galaxy (bottom) for four subhaloes: 14 (top left), 23 (top right), 25 (bottom left) and 56 (bottom right) as a function of redshift. In each of the top panels, the black line denotes the dark matter mass, the red line denotes the gas mass, and the blue line denotes the stellar mass. The dotted lines denote the time of infall. Before outflow and/or stripping, the galaxies reach peak baryon masses of $\sim 5 \times 10^7$–$3 \times 10^8 M_\odot$, corresponding to $\sim 2 \times 10^2$–10^3 SPH particles.

- Subhalo 25, in the bottom left, keeps a significant amount of gas and continues to form stars up to its infall at $z = 0.96$. The ISM is stripped before it reaches the pericentre for the first time, and star formation ceases. The dark matter mass is subsequently reduced from its peak value of $4 \times 10^9 M_\odot$ to $6.6 \times 10^8 M_\odot$ on two close pericentre passages, while the stellar mass also decreases, particularly during the second passage.

- In the bottom right, subhalo 56, is a peculiar case. Having lost some gas due to supernova feedback, the remainder is lost almost instantaneously at $z = 6$, when the effect of the UV background sets in. As for subhalo 14, a small amount of gas gets re-accreted and is lost again as the subhalo

Figure 4.6: Orthogonal projections of the gas distribution at $z = 0$, identical to the middle row of Figure 4.4, together with the orbits of the four subhaloes 14 (white), 23 (red), 25 (light blue) and 56 (magenta). The square at the end of each line denotes the present position of the subhalo, while the tail end extends to $z = 1.9$. All four subhaloes contain stars at $z = 0$, but only halo 25 also contains gas until $z = 0.8$, as indicated by the corresponding dotted segment of the light blue orbit.

approaches the central halo. The galaxy first becomes a satellite at $z = 2.0$, but does not get close to the centre on its first orbit, resulting in no stripping of stars, and only a small reduction of the dark matter mass. The final two passages are much closer, and as a result, the dark matter and stellar mass are both significantly reduced.

Three of the four objects have peak dark matter masses between 7×10^8 and $2.5 \times 10^9 \mathrm{M}_\odot$, with subhalo 56, which loses its gas due to UV, has a peak mass of 5×10^8. The final dark matter masses lie between 5.8×10^8 to $2 \times 10^8 \mathrm{M}_\odot$, with final stellar masses in the range of 2×10^6 to $4 \times 10^7 \mathrm{M}_\odot$, and corresponding stellar mass – total mass ratios of 50-100. The four objects follow the overall scaling relations of Figures 4.8 to 4.9, and are also similar to the results of isolated dwarf galaxy simulations presented in Chapter 3, except for higher final stellar mass – total mass ratios for those objects most strongly effected by stripping.

Figure 4.6 shows the orbits of the four subhaloes described above in three different projections after z=1.9. While the four satellites are on similar orbits (in contrast to the two cases shown in Figure 4.7, it can be seen that only subhalo 25 (light blue curve) still has gas when it enters the main halo; the other three having already fallen in gas free. All four subhaloes are gas free during most of their evolution as satellites.
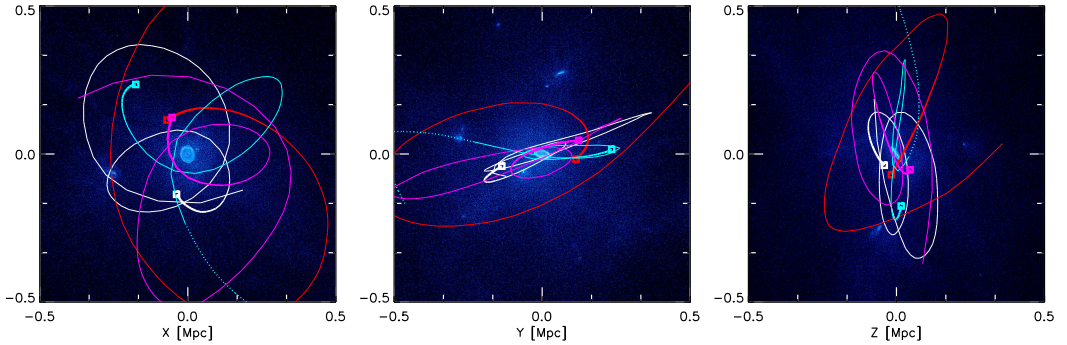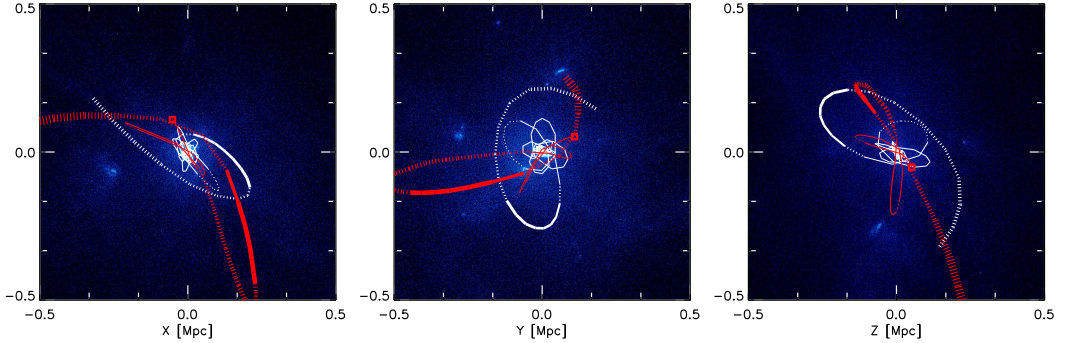
Figure 4.7: Orthogonal projections of the gas distribution at $z = 0$, identical to the middle row of Figure 4.4, together with the orbits of subhaloes 3 (white) and 5 (red) after $z = 2.45$. Both of the subhaloes lost more than 97% of their dark matter mass since infall, and the thickness of the line changes along the orbit proportional to the dark matter mass relative to the infall mass. Dotted line segments denote the presence of gas, while solid lines indicate a gas-free phase. The squares denote the present positions of the satellites.

4.5 Two Extreme Cases

Two satellites, subhaloes 3 and 5, have final stellar masses that exceed their dark matter mass. They can be identified as outliers on the $M_\star$–M_{DM} relation shown in Figure 4.8, and are off the chart in the $M_\star/M_{DM,z=0}$–$M_\star/M_{DM,infall}$ relations of Figure 4.9. This testifies to the fact that their dark matter masses decreased by a factor of 35 in the case of subhalo 5, and even ~ 200 for subhalo 3. Not surprisingly, the orbits of the two haloes, plotted in Figure 4.7, both include a number of recent close pericentre passages. A difference in orbital shape is also apparent in comparison with Figure 4.6. The dashed and solid line segments in Figure 4.7 indicate the presence or absence of gas, respectively. It can be seen that both objects still have gas when they first fall into the main halo. Interestingly, they both go through a gas-free phase on their first pericentre passage, but both recollect gas twice during their subsequent evolution, only to lose it again at each pericentre passage.

The two objects enter the halo with stellar mass – total mass ratios of 30 to 40 and properties similar to dwarf irregular galaxies, including gas to stellar mass ratios of order unity. They end up gas-free, with significantly reduced stellar masses, but also with final stellar mass – total mass ratios close to unity. Quantitatively, this result should be taken with caution, as the close pericentre passages make

the evolution of the subhaloes also dependent on the detailed properties of the simulated central galaxy. In addition, some particles belonging to the outer parts of a satellite subhalo may be misattributed to the main halo instead, even though they remain gravitationally bound, and continue to move with the subhalo. However, qualitatively, this result suggests that strong tidal stripping *decreases*, rather than increases, the total mass-to-light ratio of satellite galaxies, and is therefore not a viable way to transform gas-rich, bright dwarf irregulars into the gas-free, faint dwarf spheroidals with *high* mass-to-light ratios observed around the Milky Way.

4.5.1 Satellite Galaxies with Gas

Something can also be learnt about gas loss by considering the four satellites that still contain gas at $z = 0$. With halo masses between 5×10^9 to $8 \times 10^{10} \mathrm{M}_\odot$, these are among the most massive subhaloes; no subhalo less massive than $5 \times 10^9 \mathrm{M}_\odot$ still contains gas at $z = 0$. None of these four satellite galaxies had particularly close encounters with the central galaxy, the minimum distance range from ~ 80 to 330 kpc. However, this does not clearly separate them from the gas-free satellites, many of which are on even less bound orbits, or already fell in gas-free. The present galactocentric distances are also not significantly different among the two sub-populations.

Interestingly, two of the only three satellite galaxies which are more massive than $5 \times 10^9 \mathrm{M}_\odot$ *and* gas-free, are hosted in subhaloes 3, 5, which underwent particularly strong tidal interactions and were discussed in more detail in Section 4.5. Thus, it appears that maximal total masses of a few $\times 10^9 \mathrm{M}_\odot$ and orbits which avoid the inner halo are both required to retain any gas at $z = 0$. Equivalently, masses below a few $\times 10^9 \mathrm{M}_\odot$ or very close orbits, are both sufficient to produce gas-free satellite galaxies. If the majority of dwarf spheroidals reside in subhaloes with masses below $10^9 \mathrm{M}_\odot$ at present as well as at infall, cases of orbital metamorphosis are rare.

It is also worth noting that the most massive surviving satellite (subhalo 1), fell in as late as $z = 0.13$, and did so together with subhalo 7, another gas-rich companion. The two can easily be identified in Figures 4.1 to 4.3, where both are visible only in the last panels. It has been noted previously that the presence of two satellites as bright as the Magellanic Clouds near the Milky Way is rather unusual in ΛCDM (e.g Boylan-Kolchin et al., 2010). Tremaine (1976) showed that dynamical friction in the halo of the Milky Way would lead to a rapid decay of the orbits of such large satellites, which would therefore be short-lived, surviving only a few Gyrs. Proper motions (e.g. Besla et al., 2007; Piatek et al., 2008) suggest that the Magellanic Clouds are indeed near their first pericentre after infall.

4.6 Scaling Relations

At redshift $z = 0$, the halo contains 199 satellite subhaloes, with masses between 10^{11} and $10^{8}\mathrm{M}_\odot$. Of these, 90 have stars, and 4 also contain gas. The properties of all satellites are listed in Table 4.1 on page 112 of the appendix. They include the present stellar, gas and dark matter mass, their present galactocentric distance and the distance of closest approach, the infall redshift, the mass at infall, the median and maximum stellar metallicity, and the minimum and median stellar ages. In this section, we explore the scaling relations among these properties. We focus in particular to the way in which the formation and evolution of the satellite population is linked to the subhalo mass, and to the influence of the environment.

4.6.1 Stellar Mass - Halo Mass

Figure 4.8 shows the relationship between present stellar mass and dark matter mass of all satellites that contain stars at $z = 0$. In the left panel, the dark matter mass is the current mass of each subhalo, while in the right panel, the dark matter mass is the mass of the satellite at infall, i.e. when it first became a subhalo of the host halo (see Section 4.2.3). In both cases, there is a clear correlation of stellar mass and halo mass, indicating that the processes that determine the amount of star formation per subhalo are regulated primarily by its mass. For a halo with an infall mass of $\sim 10^{9}\mathrm{M}_\odot$, the corresponding stellar mass is between a few times 10^{5} to a few times $10^{7}\mathrm{M}_\odot$. It should be noted that the minimum stellar mass resolved in the simulations is $2 \times 10^{5}\mathrm{M}_\odot$.

The two subhaloes discussed in Section 4.5, which underwent particularly strong tidal stripping, can be identified as outliers in the relation of stellar mass to present halo mass. Overall, the scatter is noticeably smaller when the mass at infall, rather than the present day mass is considered, suggesting that the evolution of the satellite after infall also plays a role in some cases. However, it is worth noting that environmental effects primarily reduce the *halo mass*, rather than the *stellar mass*, contrary to the scenario described in Section 1, whereby faint dwarf galaxies are formed through stripping of baryons.

Figure 4.8 also includes a comparison with results from our earlier simulations of isolated dwarf galaxies with much higher resolution. In both panels, the black stars denote results from simulations labelled 12–20, with total masses of 2.3×10^{8}–$10^{9}\mathrm{M}_\odot$, presented in Chapter 3, with stellar particle masses of 5.4×10^{2}–$2.7 \times 10^{3}\mathrm{M}_\odot$. Blue stars are adopted from Chapter 5, where six haloes with representative merger histories and a common mass scale of $\sim 10^{10}\mathrm{M}_\odot$ were re-simulated, with a stellar particle mass resolution of $9 \times 10^{3}\mathrm{M}_\odot$. Despite the difference in resolution of up to two orders of magnitude, the results are in good agreement between the different sets of simulations, particularly when the dark
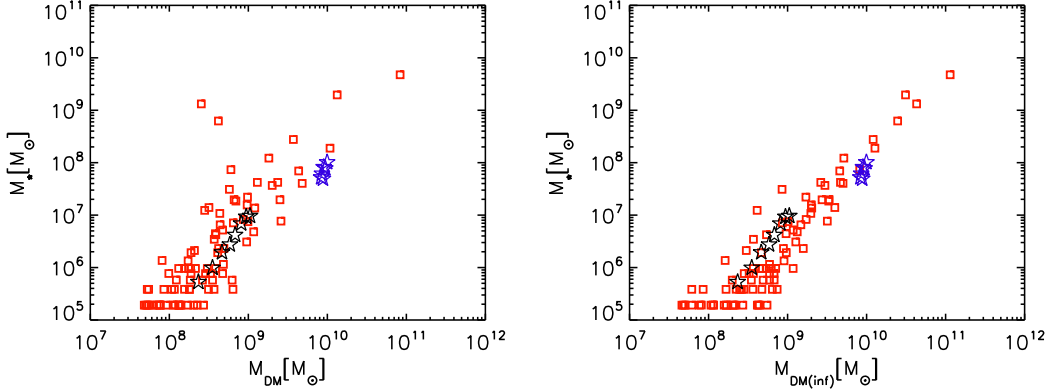
Figure 4.8: Stellar mass per subhalo as a function of mass in dark matter. In both panels, red squares denote satellite galaxies in the *Aquila* simulation. The left panel shows the dark matter mass at $z = 0$, while the right panel shows the mass at infall. In both cases, stellar mass and total mass are clearly correlated. For comparison, the star symbols denote the results of high-resolution simulations of individual dwarf galaxies: black stars are haloes 12–20 of Sawala et al. (2010), blue stars are haloes 1–6 of Sawala et al. (2011). The smaller scatter in the relation between stellar mass and infall mass is testament to the fact that for most satellites, the stellar component is determined before infall. The scatter increases for smaller objects, and reaches about two orders of magnitude at an infall mass of $\sim 10^9 M_\odot$. For masses below $10^9 M_\odot$, an increasing fraction of haloes is completely dark. As haloes without stars are not included in these plots, this may give the false visual impression of a flattening relation or decreasing scatter at the low mass end.
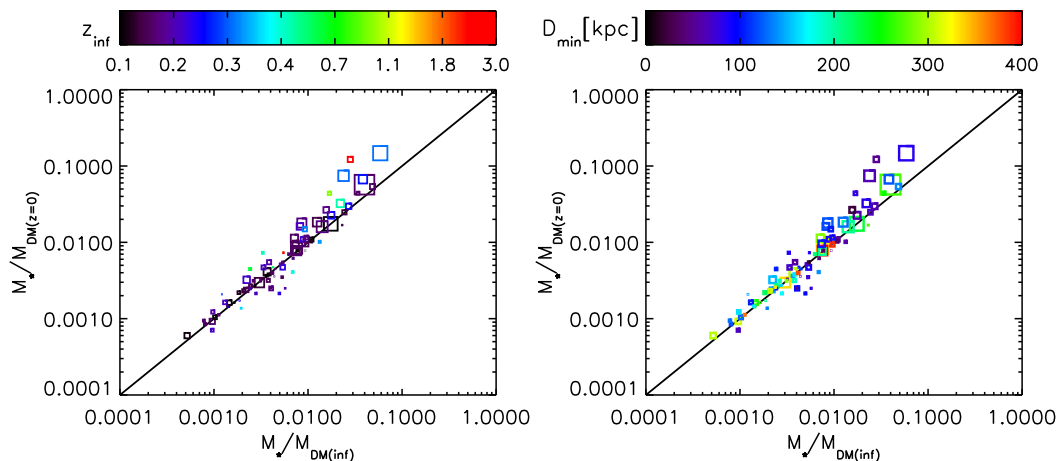
Figure 4.9: Ratio of stellar mass to halo mass of each subhalo at present, compared
to the same ratio to infall. The colour coding in the left panel indicates
the infall redshift of each subhalo, while the colour coding in the right
panel indicates the distance of closest approach between the subhalo
and the centre of the host halo. The size of the symbol is representative
of the present total mass of each object. Haloes above the black line
increased their stellar mass - halo mass ratio since infall, while haloes
below the black line decreased it.

matter masses are corrected for the effect of stripping, as shown in the right panel.
Because the same code has been used in all three sets of simulations, it follows
that the results are not strongly affected by resolution.

The two panels in Figure 4.9 both show the change in stellar mass – halo mass
ratio of each object from infall to the present. The ratio at infall is shown on the
x-axis, while the present ratio is shown on the y-axis. Most points lie close to
the black line, which indicates a constant ratio. Notably however, the majority of
haloes are above the line, meaning that their stellar mass fraction has increased
since infall. This can be understood as a consequence of preferential stripping of
dark matter compared to stellar matter, which is more centrally concentrated and
therefore more strongly bound to the satellite. In the left panel, the colour-coding
is by infall redshift; black and blue symbols indicate recent accretion, yellow and
red symbols indicate infall at high redshift. In general, satellites that fell in earlier
are more likely to have changed their ratio since infall, as expected if the change
is due to continuous tidal stripping. In the right panel, the colour-coding is done
by distance of closest approach between the subhalo and the halo of the central
galaxy. As expected, haloes that had closer encounters are also the ones that
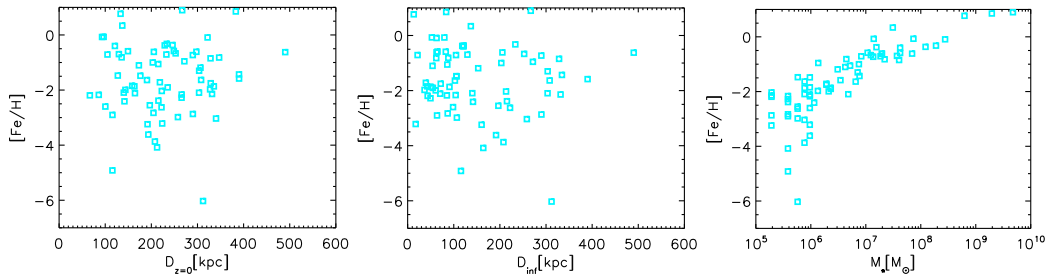
Figure 4.10: Maximum stellar iron abundance within each subhalo, as a function of present distance (left), distance of closest approach (centre), and stellar mass (right). Note that those satellites with only primordial abundances are not included. As is observed in the Local Group, there is a clear correlation of metallicity with stellar mass, but not with present position nor distance of closest approach.

underwent a slightly stronger change in the stellar mass to halo mass ratio since infall. It appears that the haloes with the greatest distance ($D_{min} > 300$kpc) have seen no change in the ratio, but these are commonly also subhaloes that have fallen in only recently ($z_{inf} < 0.2$). In both panels, the sizes of the symbols indicate total mass; larger satellites are typically found with higher stellar mass – total mass ratios, independent of infall time or orbit.

4.6.2 Stellar Populations

Due to the small numbers of stellar particles per subhalo in the simulation, a detailed analysis of stellar populations is not possible. As a proxy for star formation history, we consider the maximum iron abundance [Fe/H] of the stars in each satellite galaxy. Because iron is formed only in the late stages of stellar evolution and injected into the interstellar medium via supernovae, the amount of iron observed in stars corresponds the specific degree of reprocessing of material within each galaxy, and the intensity and duration of star formation.

Figure 4.10 shows the maximum stellar iron abundance of the satellites, as a function of present distance (top left), distance of closest approach (top right), and present-day stellar mass (bottom). Note that satellites with only a single generation of stars have primordial abundances, i.e. [Fe/H] $\equiv -\infty$, and therefore do not appear on the plotted relations.

The lack of a correlation on both the left and central panels indicate that the iron abundance does not depend strongly on either present distance, or distance of closest approach in the past. By contrast, there is a strong correlation with

stellar mass, as observed in the Local Group, and also reproduced in our earlier simulations of isolated dwarf galaxies, shown in Figure 3.11 and discussed in Chapter 3. At lower stellar mass, the scatter increases, similar to the trend in the relation of stellar mass and halo mass seen in Figure 4.8.

4.7 Isolated Dwarf galaxies

Evident from Figures 4.1 through 4.4, the high resolution volume also contains plenty of structures outside of the Milky Way halo. In this section, we compare the population of Milky Way satellites discussed in the previous chapters to the isolated dwarf galaxies that form in the remaining volume. At $z = 0$, there are a total of 2097 subhaloes in the simulation, only $\sim 10\%$ of which are part of the most massive halo. Not all objects outside of the main group are truly isolated, as some of the other FoF groups also contain multiple subhaloes (see Section 4.2.3). The second largest FoF group in the simulation hosts a galaxy with a stellar mass of $1.1 \times 10^{10} \mathrm{M}_\odot$ and contains 68 additional subhaloes. The next most massive galaxy in the simulation has a stellar mass of $1.7 \times 10^9 \mathrm{M}_\odot$. Throughout this section, we consider as *isolated* all subhaloes which are not part of the two most massive haloes. Of these 1810 subhaloes, 420 host stars, and 144 also contain gas. We compare these to the *satellites* of the Milky Way halo, that were discussed in the previous sections.

Figure 4.11 shows the relation of stellar mass to halo mass for satellite galaxies (in red) and for these isolated dwarfs (in blue). When the mass ratios are compared at $z = 0$ (upper panel), the satellites contain a systematically higher stellar mass for a given halo mass compared to the isolated galaxies. The difference is reduced when the infall masses are considered for the satellites (lower panel). The trend that low-mass, isolated subhaloes still show a higher mean dark matter mass in this second relation may be partly due to the fact that they typically grow in mass until $z = 0$, while satellites peak at $z_{inf} > 0$. However, it is also partly attributable to the identification of substructures, which requires a higher density if the mean background density is higher. Interestingly, in the upper panel, the population of isolated dwarf galaxies also shows two outliers in the $M_\star - M_{DM}$ relation, which are denoted by blue open circles in both panels. While these two deviate not as significantly as the satellites which were discussed in Section 4.5, it points to the fact that even some dwarf galaxies which are isolated at $z = 0$, may have undergone interactions in the past. The two objects with high stellar to total mass ratios were never satellites of the main halo, but have interacted with smaller groups of galaxies, which also lead to tidal stripping, mostly of dark matter. In the lower panel, we plot their dark matter masses before their last interactions, which brings them closer to the relation defined by both populations.
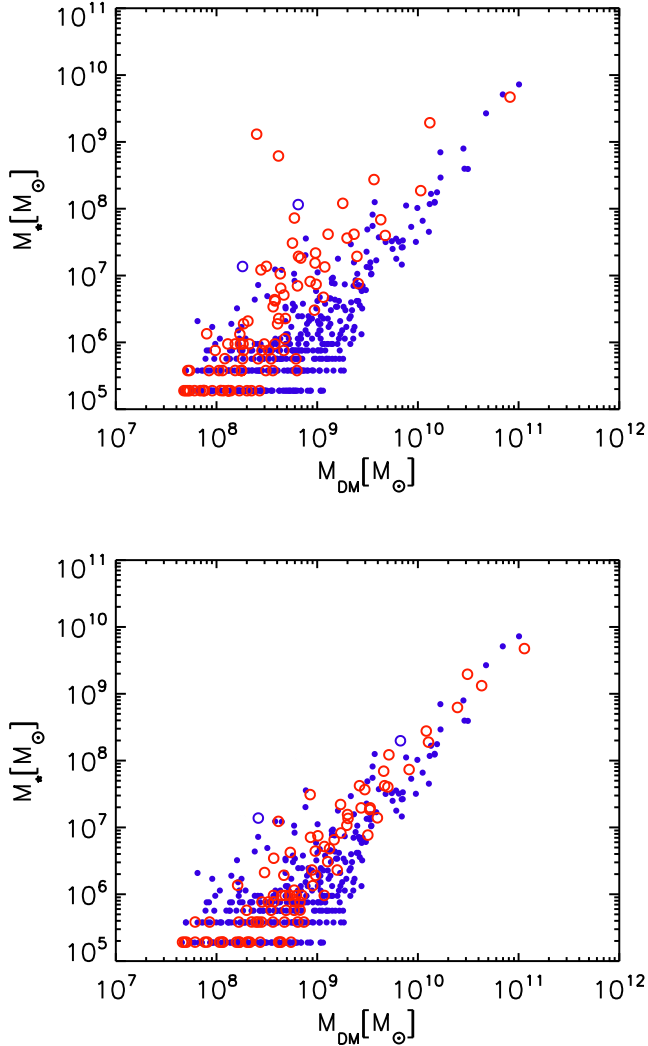
Figure 4.11: Stellar mass per subhalo as a function of dark matter mass. In both panels, *isolated* galaxies are shown as blue dots, *satellite* galaxies are overplotted as red, open circles. The two blue, open circles represent dwarf galaxies presently isolated, but which had past interactions, as described in the text. In the upper panel, the dark matter mass of both the isolated and the satellite galaxies is taken at $z = 0$, while the infall mass of the satellites and the interacting isolated galaxies is used in the lower panel, as in Figure 4.8. The fraction of subhaloes without stars (not shown) is 55% for the satellite subhaloes of the Milky Way, and 77% for the isolated subhaloes.
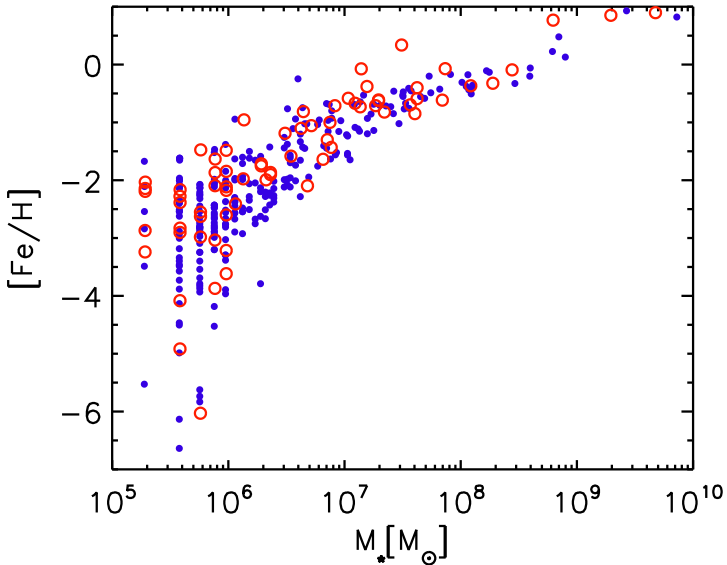
Figure 4.12: Maximum stellar iron abundance, for *isolated* dwarf galaxies (blue) and *satellite* subhaloes (red). There is no significant difference in either the correlation of metallicity with stellar mass, or in the amount of scatter, which in both cases increases significantly at the low mass end.

It is also worth noting that the fraction of subhaloes without stars are different among the two populations: Whereas 45% of the satellite subhaloes contain stars at $z = 0$, only 23% of the isolated subhaloes contain stars. This indicates that the lowest mass subhaloes, which are unable to form stars even in isolation, often do not survive to $z = 0$ if they become satellites.

Figure 4.12 compares the maximum iron enrichment [Fe/H] of stars in satellites and isolated galaxies, similar to the bottom panel in Figure 4.10. In both cases, there is a clear trend of increasing metallicity with stellar mass, with a large scatter at the low mass end, partly attributable to discreteness effects. At a given mass, the iron enrichment and the scatter are similar in both populations, indicating that mass, rather than environment, is the primary determinant for the star formation history of dwarf galaxies.

In Figure 4.13, we compare the gas content of satellites and isolated dwarf galaxies as a function of halo mass. As described in Section 4.5.1, there are only four satellite galaxies with gas at $z = 0$, which are found in some of the most massive subhaloes. Most of the isolated dwarf galaxies at $z = 0$ are also gas free,
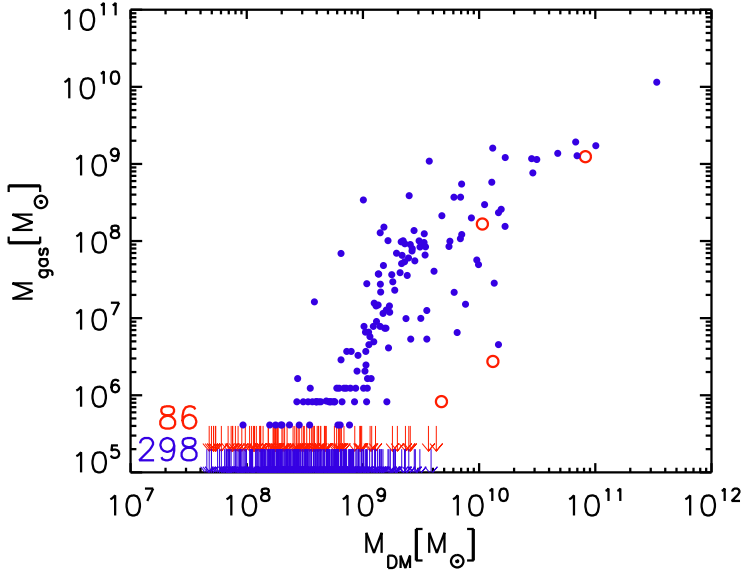
Figure 4.13: Gas mass as a function of present subhalo mass for *isolated* dwarf galaxies (blue) and *satellite* dwarf galaxies (red). Filled (open) circles indicate isolated (satellite) galaxies with $M_{gas} > 0$; arrows show the dark matter masses of galaxies that contain stars, but no gas. The red and blue numbers indicate the total number of gas-free subhaloes with stars for the two populations. The fraction of gas-free galaxies over the mass range shown, is $\sim 95\%$ for satellites, and $\sim 75\%$ for isolated dwarf galaxies.

but about one quarter of the isolated galaxies still contain some gas at $z = 0$. Among the isolated galaxies, there is a sharp drop in gas mass at subhalo masses of $\sim 2 \times 10^9 \mathrm{M}_\odot$. More massive isolated galaxies predominantly contain gas, less massive galaxies are most often gas-free, and resemble the satellite population. This points to a mass-threshold below which gas removal is efficient, and mostly independent of environment, while more massive galaxies can keep their gas in isolation. Close to this mass threshold, the populations differ; while some isolated dwarf galaxies still contain gas, no gas is found in the satellites. It should be noted, however, that while there are only four satellite galaxies with gas at $z = 0$, the total number of satellite galaxies above the mass threshold is also very low. The most massive, gas free galaxies are found in subhaloes of $\sim 5 \times 10^9 \mathrm{M}_\odot$ in both the satellite and the isolated populations.

4.8 Summary

Before summarising, it should be emphasised again that some of the results presented in this paper are scraping the resolution limit of the *Aquila* simulation, which was designed to study much larger galaxies. We have, however, been able to demonstrate that the results are consistent with our much higher resolution simulations of individual dwarf galaxies. The simulation is also not enough to solve all the questions pertaining to the dwarf galaxy satellites of the Milky Way; the so-called *ultra-faint* dwarfs are clearly outside the scope of the simulation, and even some of the classical faint satellites are only resolved with a handful of particles. Tidal effects, believed to be the main stripping mechanism, should not depend very strongly on force resolution. However, if ram-pressure stripping were effective in the Local Group, it would likely be severely underestimated, because the gas pressure is only poorly determined, and pressure gradients are artificially smoothed in the SPH formalism.

While the resolution is limited, it is reassuring that the properties of these galaxies tend to agree with the higher resolution simulations of isolated dwarf galaxies, and that the number of $\sim 20 - 30$ dwarf-spheroidal-like galaxies with stellar masses in the range of $\sim 10^6 \mathrm{M}_\odot$ qualitatively agrees with the observational counts. At the same time, the fact that the simulation was not *designed* to study dwarf galaxies may actually be an advantage: Considering that dwarf galaxies and Milky Way sized galaxies form in the same universe, it is only natural that they are simulated with the same realisation of the physical laws and parameters.

We have described the formation of the satellite population in a cosmological simulation of a Milky Way sized halo and its environment, that includes hydrodynamics, cooling, star formation, supernova feedback, enrichment and UV radiation. Of the 199 subhaloes with masses above $6 \times 10^7 \mathrm{M}_\odot$, 90 contain stars and four contain gas at $z = 0$.

We identified different mechanisms of gas-removal, both independent of environment (supernova feedback and UV heating), and caused by interactions with the host halo (tidal stripping). It was found that with a few notable exceptions, the properties of the satellites as a whole depend only weakly on environment, but very strongly on the mass of the subhalo. The satellite galaxies that contain stars follow a steep stellar mass – total mass relation, and a stellar mass–metallicity relation which are similar to those observed, and indistinguishable from those for isolated dwarf galaxies in the same simulation. The relations are also similar to those obtained by high resolution simulations of isolated dwarf galaxies, discussed in Chapter 3.

In our simulation, tidal interactions after infall affect the dark matter haloes of satellites more strongly than their stellar components. The result is an average *increase* in total stellar mass – halo mass ratio, or a corresponding *decrease* in total mass-to-light ratio after infall. This is difficult to reconcile with the transformation of luminous, late type galaxies with moderate mass-to-light ratios into dwarf-spheroidals with the high mass-to-light ratios inferred from observations, and required from abundance-matching arguments (e.g. Guo et al., 2010). Furthermore, the trend of decreasing mass-to-light ratio is more pronounced for satellites on closer orbits, and with earlier infall times. This suggests that, if dwarf spheroidal galaxies of different luminosities originated from common, gas rich and bright progenitors subject to different levels of interaction, their final stellar mass after stripping would scale *proportional* to their total mass-to-light ratio; the opposite of which is commonly inferred from observations.

Peñarrubia et al. (2010) have shown in purely gravitational simulations that preferential stripping of stars may be possible in a Milky Way potential if the infalling satellite haloes are cusped, so that the dark matter is more concentrated than the stars. Unfortunately, our fully cosmological, hydrodynamical simulations fall short of resolving the inner parts of satellite subhaloes to distinguish between cusped and cored profiles by several orders of magnitude, but the softened potential acts as an *effective* core. While the direct observational evidence for cusps or cores in dwarf spheroidals is still not clear, it should be noted that cores are not necessarily unique to "warm" dark matter: as shown by Navarro et al. (1996), and recently confirmed in simulations by Governato et al. (2010), baryonic feedback processes may result in cores in low-mass, cold dark matter haloes. If cores are a universal feature of dwarf galaxies, the transformation of dwarf irregulars to dwarf spheroidals purely via tidal effects would be difficult to reconcile with our results.

Instead, we find that satellite galaxies that end up with high total mass-to-light ratios at $z = 0$ are already faint on infall, and many of them have already lost their gas as a result of supernova feedback and UV radiation. While tidal interactions can remove remaining interstellar gas, as we observe in several cases, all these results suggest that the star formation of dwarf spheroidal galaxies is mostly determined independent of environment, and very strongly dependent on mass.

At a total mass of $\sim 1 - 3 \times 10^9 \mathrm{M}_\odot$, the populations of isolated and satellite dwarf galaxies differ in the fraction of galaxies with gas. Whereas all satellite galaxies in this mass range are gas-free, isolated galaxies show a sharp decline in gas fraction, but many of them still contain gas at $z = 0$. Qualitatively, this is in agreement with the HI mass–distance relation reported by Grebel et al. (2003) and Geha et al. (2006). In the mass regime of dwarf spheroidals, however,

with stellar masses below $10^7 M_\odot$ and inferred dynamical masses below $10^9 M_\odot$, both the satellites and most of the isolated dwarf galaxies are gas-free. Consequently, the dwarf spheroidal galaxies formed in the simulation do not follow a clear morphology-distance dichotomy. If such a sharp relation exists, the galaxies that constitute this relationship would not only have to form in a different way compared to the simulation, but also be on different orbits, as we find that present day position is not a good proxy for past interaction.

Table 4.1: Data for satellite galaxies in the *Aquila* simulation

Label	$M_\star$ [$10^6 M_\odot$]	M_{gas} [$10^6 M_\odot$]	M_{DM} [$10^8 M_\odot$]	M_{inf} [$10^8 M_\odot$]	Z_{inf}	Z_{form}	D [kpc]	D_{min} [kpc]	[Fe/H]
1	4745.17	1259.41	833.43	1142.22	0.13	9.37*	266.9	266.9	-1.06
2	1960.70	2.78	133.21	310.85	0.53	10.91	383.1	83.5	-0.94
3	1322.04	–	2.54	429.65	2.32	12.07	13.2	13.2	-0.63
4	188.92	168.56	108.16	128.96	0.07	5.23*	233.5	233.5	-1.82
5	623.97	–	4.18	247.15	2.10	15.47	133.3	13.2	-0.72
6	276.84	–	37.15	121.12	0.50	14.73	321.9	62.8	-1.49
7	40.32	0.84	48.05	50.31	0.13	13.34*	328.3	328.3	-2.21
8	69.45	–	43.37	45.73	0.70	4.67*	205.4	205.4	-1.89
9	122.04	–	18.19	51.53	1.07	12.07	246.1	121.5	-1.84
10	42.12	–	23.53	46.69	0.15	9.86	121.0	121.0	-2.05
11	19.61	–	25.15	27.30	0.13	9.37	490.2	490.2	-2.36
12	7.68	–	25.90	31.83	0.38	10.38	390.0	334.5	-2.74
13	36.82	–	20.05	29.71	0.09	8.45*	129.6	129.6	-1.95
14	42.11	–	13.00	26.31	2.20	13.34	149.3	82.6	-2.09
15	73.51	–	6.02	81.83	2.90	15.47	96.6	52.5	-1.43
16	13.64	–	12.06	20.23	0.13	16.25	289.9	289.9	-1.93
17	22.03	–	9.76	17.05	1.36	5.83*	346.9	62.0	-2.21
18	4.80	–	11.69	13.24	0.05	10.38	303.4	303.4	**
19	15.60	–	9.65	20.01	0.24	14.73	228.9	118.4	-2.16
20	7.49	–	9.89	10.16	0.13	12.07	203.0	203.0	-2.90
21	3.08	–	9.52	12.70	0.26	9.86	306.6	152.9	-2.86
22	8.26	–	8.63	17.18	1.41	7.22	104.9	104.9	-2.23
23	30.98	–	5.76	8.52	1.60	12.69	137.0	137.0	-1.40
24	18.51	–	6.96	33.16	0.18	12.07	232.6	21.6	-1.98
25	19.63	–	6.61	33.58	0.99	12.69	297.6	62.6	-1.88
26	7.10	–	6.46	8.58	0.13	8.90	303.6	303.6	-3.05
27	0.38	–	6.39	7.38	0.07	7.62	304.1	304.1	**
28	0.58	–	6.24	4.90	0.13	11.48	312.0	312.0	**
29	10.77	–	4.36	19.70	0.92	11.48	248.7	64.7	-2.32
30	5.19	–	4.73	11.78	0.85	11.48	215.0	86.0	-2.23
31	2.31	–	4.90	15.81	2.10	10.91	163.3	90.8	-2.99
32	6.54	–	4.40	14.73	0.55	8.02	190.6	102.5	-2.85
33	1.15	–	4.84	5.91	0.10	7.62	141.7	141.7	-3.05
34	0.77	–	4.73	6.74	0.24	9.37	340.2	258.5	-4.45
35	13.93	–	3.17	39.60	3.09	9.37	93.1	79.6	-1.09
36	2.31	–	4.20	8.87	0.21	8.02	235.4	54.7	-2.57
37	4.23	–	3.87	5.41	0.15	0.15	173.0	54.0	-2.19
38	4.42	–	3.83	9.57	0.92	8.45	135.6	88.1	-1.77
39	1.92	–	4.09	9.63	0.33	8.90	328.7	71.7	-3.05
41	12.32	–	2.80	4.12	0.13	10.38	252.6	252.6	-1.74

Continued on next page...

Table 4.1 – Continued

Label	$M_\star$ $[10^6 M_\odot]$	M_{gas} $[10^6 M_\odot]$	M_{DM} $[10^8 M_\odot]$	M_{inf} $[10^8 M_\odot]$	Z_{inf}	Z_{form}	D [kpc]	D_{min} [kpc]	[Fe/H]
42	3.46	–	3.70	3.70	0.13	8.02	390.2	390.2	-3.30
43	0.96	–	3.85	6.22	0.17	10.91	100.3	98.4	-4.82
45	0.38	–	3.68	4.73	0.31	7.62	447.4	127.2	**
46	0.58	–	3.52	5.91	0.24	8.90	257.5	106.7	-3.36
47	0.77	–	3.33	3.70	0.18	8.02	307.9	307.9	-2.96
48	0.38	–	3.13	3.63	0.21	8.45	212.5	164.0	-4.08
49	0.96	–	3.02	3.68	0.92	12.07	193.4	191.6	**
51	0.77	–	2.87	3.26	0.65	2.74	207.7	207.7	-4.07
52	0.19	–	2.71	5.49	0.28	6.50	357.1	66.6	**
53	0.58	–	2.63	3.48	0.73	7.62	222.0	222.0	-2.86
56	2.11	–	2.08	3.00	2.10	12.07	143.7	60.8	-6.99
57	0.19	–	2.25	4.38	0.50	7.62	259.8	120.2	**
58	0.96	–	2.15	5.36	1.11	7.62	176.3	106.0	-2.62
59	1.92	–	1.88	4.66	0.53	10.38	218.5	39.5	-2.36
60	0.19	–	2.04	2.15	0.14	1.36	129.8	129.8	**
63	0.96	–	1.86	4.79	1.47	11.48	164.4	70.6	-4.77
64	0.77	–	1.88	2.82	3.29	10.38	140.2	140.2	-4.07
65	0.58	–	1.84	1.99	0.13	7.22	196.6	196.6	-2.89
66	1.34	–	1.73	9.02	1.20	8.45*	327.3	36.7	-2.98
67	0.96	–	1.75	4.44	1.67	10.38	223.5	17.5	**
68	0.38	–	1.80	2.47	1.03	10.91	267.2	97.9	**
70	0.38	–	1.80	2.80	1.07	8.02	235.1	172.1	**
71	0.19	–	1.71	1.69	0.13	4.42	367.7	367.7	**
73	0.96	–	1.55	11.76	0.79	10.91	158.5	42.6	-2.38
74	0.38	–	1.55	2.23	1.11	1.11*	265.7	104.1	-2.16
78	0.96	–	1.31	7.07	3.71	15.47	86.0	85.1	-2.58
79	0.19	–	1.40	2.71	1.41	10.38	136.0	136.0	**
83	0.19	–	1.34	1.58	0.44	0.44*	207.3	207.3	**
84	0.19	–	1.34	2.01	1.47	8.02	251.0	214.5	**
86	0.19	–	1.31	1.69	1.53	7.22	307.0	170.2	**
87	0.58	–	1.23	6.76	2.45	7.22	127.3	105.6	-2.13
94	0.38	–	1.16	6.41	1.30	10.38	265.5	49.5	-2.28
95	0.19	–	1.18	1.16	1.36	1.36*	261.9	261.9	**
97	0.19	–	1.12	1.14	0.35	0.60	222.6	213.3	-2.03
98	0.38	–	1.07	1.66	0.18	4.17	115.7	63.7	-2.90
101	0.77	–	0.99	5.91	1.67	8.45	335.5	50.1	-2.06
105	1.36	–	0.81	1.62	0.13	11.48	271.6	271.6	-1.68
110	0.19	–	0.92	4.14	2.58	6.85	188.1	145.8	**
113	0.38	–	0.85	0.85	0.28	0.28*	115.6	115.6	-4.92
119	0.19	–	0.77	4.27	0.79	10.91	66.7	43.3	-2.19
120	0.19	–	0.77	2.08	1.67	1.82	78.8	78.8	**

Continued on next page...

Table 4.1 – Continued

Label	$M_\star$ $[10^6 M_\odot]$	M_{gas} $[10^6 M_\odot]$	M_{DM} $[10^8 M_\odot]$	M_{inf} $[10^8 M_\odot]$	Z_{inf}	Z_{form}	D [kpc]	D_{min} [kpc]	[Fe/H]
123	0.19	–	0.74	0.81	0.13	10.91	331.6	331.6	-2.14
128	0.19	–	0.70	0.77	0.42	0.42*	191.7	160.4	-3.24
133	0.19	–	0.61	0.61	0.13	0.28	290.0	290.0	-2.87
147	0.38	–	0.55	0.61	0.14	0.42	215.3	215.3	-2.39
152	0.38	–	0.53	2.61	1.25	1.25*	204.6	86.8	-2.83
159	0.19	–	0.55	1.07	0.29	0.29*	271.5	74.8	**
161	0.19	–	0.53	0.50	0.04	0.04*	144.7	144.7	**
167	0.19	–	0.50	0.48	0.05	0.05*	165.1	165.1	**
177	0.19	–	0.48	0.46	0.13	0.33*	379.8	379.8	**

Notes: Col. 2: Stellar mass, Col. 3: Gas mass, Col. 4: Dark matter mass (all at z=0), Col. 5 : Dark matter mass (at infall), Col. 6: Infall redshift, Col. 7: Formation redshift, Col. 8: Distance to the centre of central galaxy (at z=0), Col. 9: Distance of closest approach, Col. 10: Maximum stellar iron abundance.

Remarks: ** indicates that more than half of the stars have primordial abundances. – indicates that the mass of the component is zero. Z_{form}* with an asterisk indicates the redshift of *fragmentation*, as defined in Section 4.2.3. A total of 109 "dark" subhaloes, without baryons, are omitted.

5

What is the (Dark) Matter with Dwarf Galaxies?

We present cosmological hydrodynamical simulations of the formation of dwarf galaxies in a representative sample of haloes extracted from the Millennium-II simulation. Our six haloes have a $z = 0$ mass of $\sim 10^{10} M_\odot$ and show different mass assembly histories which are reflected in different star formation histories. We find final stellar masses in the range of $5 \times 10^7 - 10^8 M_\odot$, consistent with other published simulations of galaxy formation in similar mass haloes. Our final objects have structures and stellar populations consistent with observed dwarf galaxies. However, in a ΛCDM universe, $10^{10} M_\odot$ haloes must typically contain galaxies with much lower stellar mass than our simulated objects if they are to match observed galaxy abundances. The dwarf galaxies formed in our own and all other current hydrodynamical simulations are more than an order of magnitude more luminous than expected for haloes of this mass. We discuss the significance and possible implications of this result.

5.1 Introduction

Dwarf galaxies are by far the most abundant type of galaxy in the Local Group and in the Universe. They span a large range of stellar masses, morphologies and star formation histories. The largest dwarf irregulars such as the large Magellanic Cloud have stellar masses of $\sim 10^9 M_\odot$, rotationally supported and HI-rich disks, and strong ongoing star formation. In contrast, dwarf spheroidal galaxies have stellar masses from $10^7 M_\odot$ to below $10^3 M_\odot$, they possess no interstellar gas, and they show no sign of rotational support or ongoing star formation.

The number of dwarf galaxies observed in the Local Group continues to grow as new, 'ultra-faint' satellite galaxies are discovered (e.g. Martin et al., 2006; Chapman et al., 2007; Belokurov et al., 2010). Estimates using luminosity functions corrected for completeness and bias predict the total number of faint satellites to be an order of magnitude higher still (Tollerud et al., 2008; Koposov et al., 2008). Nevertheless, this is still much smaller than the total number of dark matter subhaloes found in high-resolution simulations of the standard ΛCDM cosmology (e.g. Klypin et al., 1999; Moore et al., 1999; Diemand et al., 2007; Springel et al., 2008). This difference has become known as the "Missing Satellites Problem". It may only be an apparent discrepancy, however, since it can be removed if one accounts for the fact that not all low-mass subhaloes must contain stars, and those that do may have very high mass-to-light ratios. Several astrophysical mechanisms have been suggested that can lead to a number of visible satellite galaxies similar to that observed. Perhaps haloes were able to form a few stars initially, but the baryonic components of all haloes below some critical mass were subsequently destroyed by supernova feedback (e.g. Larson, 1974; Dekel & Silk, 1986; Ferrara & Tolstoy, 2000). Alternatively (or perhaps additionally) photoionization may have prevented star formation in the smallest haloes (e.g. Efstathiou, 1992; Somerville, 2002; Hoeft et al., 2006; Simon & Geha, 2007). As Sawala et al. (2010) have shown, these two mechanisms can combine to produce very high mass-to-light ratios in haloes of $10^9 M_\odot$ and below, perhaps reconciling the number of very faint dwarf galaxies produced in ΛCDM simulations with the observations.

In this work, we turn our focus to more massive dwarf galaxies, and follow the evolution of the objects that form in haloes of $10^{10} M_\odot$. Our initial conditions are based on six haloes selected from the Millennium-II simulation (MS-II, Boylan-Kolchin et al., 2009), and resimulated at high resolution using smoothed particle hydrodynamics (SPH). Our simulations include cooling and star formation, supernova feedback, metal-enrichment and a cosmic UV background. Starting at redshift $z = 49$, we are able to follow the formation of each individual halo and its central galaxy in their full cosmological context, all the way to $z = 0$.

On the other hand, the large volume of our parent simulation allows us to verify that our sample of resimulated haloes is representative of haloes of similar mass,

and to predict a stellar mass – halo mass relation that can be tested against observation. With a box size of 137 Mpc and a mass resolution of $9.4 \times 10^6 M_\odot$, the MS-II has sufficient dynamic range to capture the statistics of the assembly of dark matter haloes between 10^9 and $10^{14} M_\odot$. By comparing its halo/subhalo mass function to the observed SDSS stellar mass function of Li & White (2009), Guo et al. (2010) derived a typical mass-to-light ratio for each halo mass. This analysis assumes a monotonic relationship between halo mass and galaxy mass with relatively small scatter, but does not rely on any other assumptions about the processes involved in galaxy formation. We use its result to test the viability of our simulations and the underlying physical model as a description of the formation of "typical" ΛCDM dwarf galaxies.

The present work constitutes the first direct comparison of high resolution, hydrodynamical simulations of individual dwarf galaxies with the observed abundance of such objects. We combine the ability to follow star formation self-consistently in individual objects with the ability to draw conclusions about the general population of dwarf galaxies.

This chapter is organised as follows: We begin in Section 5.2 by reviewing the current status of simulations of the formation of dwarf galaxies. Section 5.3 describes the selection of haloes for resimulation and the generation of our high resolution initial conditions, while the numerical methods of our hydrodynamical simulations are discussed briefly in Section 5.4. In Section 5.5, we show results for six haloes of final mass $10^{10} M_\odot$, and compare the properties of the galaxies to previous work, and to observation. In Section 5.6, we consider the predictions of our simulations for the stellar mass – halo mass relation and discuss the discrepancy with that inferred from comparing the observed stellar mass function to the halo abundance in ΛCDM simulations. We conclude with a summary and interpretation of our results in Section 5.7.

Unless stated otherwise, where we refer to the mass of a *galaxy*, we mean the stellar mass $M_\star$, whereas the mass of a *halo* includes the total dynamical mass enclosed within r_{200}, the radius that defines a spherical overdensity 200 times the critical density of the universe. When quoting the results for our own simulations, we always use physical mass units of $M_\odot$, assuming h = 0.73.

5.2 Review of Previous Work

Earlier examples of numerical studies of dwarf galaxy formation and evolution in $\sim 10^{10} M_\odot$ haloes include simulations by Pelupessy et al. (2004), Stinson et al. (2007, 2009), Valcke et al. (2008), Mashchenko et al. (2008) and Governato et al. (2010).

Table 5.1: Results of earlier numerical simulations

Reference	$M_\star$	M_{tot}	v_c or $\sigma_\star$
	$[10^7 M_\odot]$	$[10^9 M_\odot]$	$[km\ s^{-1}]$
Pelupessy et al. (2004)[1]	18	15	80
Stinson et al. (2007)[2]	7.86	5.0	15.1
Stinson et al. (2007)[2]	22	8.6	20.1
Stinson et al. (2007)[2]	38.6	14	29.9
Stinson et al. (2009)[3]	1.72	14	16.8
Valcke et al. (2008)[4]	57.9	4.1	35.2
Valcke et al. (2008)[4]	48.8	4.1	30.9
Mashchenko et al. (2008)[5]	1.0	2.0	–
Governato et al. (2010)[6]	48	35	56
Governato et al. (2010)[6]	18	20	54

Notes: Col. 2: Stellar mass, Col. 3: Halo mass (M_{200}), Col. 4: Maximum rotation velocity[1,6] or 1-D velocity dispersion[2,3,4]. All quantities are measured at $z = 0$, except for Mashchenko et al., where the halo mass is at $z = 5$ and stellar mass at $z = 6.2$.

Remarks: [1]Static initial conditions set up to reproduce the dwarf irregular galaxy DDO 47; [2,3]Static NFW profiles with initial baryon fractions of 10%[2] and 1%[3]; [4]Runs DH01 and DH02, assuming static, simplified Kuz'min Kutuzov profiles with $a = c = 4$ kpc (DH01) and 6 kpc (DH02).

The first three have investigated the evolution of dwarf galaxies embedded in dark matter haloes of constant mass. Pelupessy et al. used initial conditions modelled after dwarf irregular galaxy DDO 47, set up with a stellar disk of $1.8 \times 10^8 M_\odot$ and a gas disk of $1.9 \times 10^8 M_\odot$ inside a dark matter halo of $1.5 \times 10^{10} M_\odot$. Thus, the stellar mass to halo mass ratio is not a result of their simulation, but was chosen *a priori*. They show that the star formation behaviour in such a system is consistent with observations. Valcke et al. studied the formation of dwarf elliptical galaxies assuming cored initial dark matter profiles following Dejonghe & de Zeeuw (1988), and gas at a mass fraction of 17.5%. Cooling, star formation and feedback are included in their simulations, making their final stellar masses of $4.9 - 5.8 \times 10^8 M_\odot$ for haloes of $4.1 \times 10^9 M_\odot$ a direct prediction of their models. Stinson et al. also assume fixed dark matter profiles in their initial conditions, and perform simulations that include cooling, star formation and feedback. In Stinson et al. (2007), a fixed initial baryon fraction of 10% is assumed, and stellar masses of $7.9 \times 10^7 - 3.9 \times 10^8 M_\odot$ are produced in haloes of $5 \times 10^9 - 1.4 \times 10^{10} M_\odot$. In Stinson et al. (2009), the baryon fraction is varied, and we also include their result with a very low initial baryon fraction of 1%, that leads to a smaller stellar

mass.Valcke et al. and Stinson et al. do not include a UV background, which may contribute to the high star formation efficiency in their simulations.

Mashchenko et al. (2008) and Governato et al. (2010) both performed simulations that include the formation of the dark matter halo in a cosmological volume. Mashchenko et al. used constrained initial conditions, aimed at reaching a halo mass of $10^9 M_\odot$ at $z = 6$, and followed the evolution up to $z = 5$. At this time, their halo reached a mass of $2 \times 10^9 M_\odot$, with $10^7 M_\odot$ of stars formed. By comparison with the typical evolution of haloes in the MS-II (see Figure 5.2), we note that this is consistent with a mass of $10^{10} M_\odot$ at $z = 0$. The extent of additional star formation up to $z = 0$ is unknown, however. Most recently, Governato et al. have performed hydrodynamical simulations of two dwarf irregular galaxies at very high resolution, which they follow up to $z = 0$. This makes these most comparable to our own simulations, and also makes their results most directly comparable to observed, present-day dwarf galaxies. Their simulations start with values of $\Omega_m = 0.24$, $\Omega_b = 0.042$, and predict stellar masses of 1.8 and $4.8 \times 10^8 M_\odot$ in two haloes of 2.0 and $3.5 \times 10^{10} M_\odot$, respectively.

While these five sets of simulations vary in the setup of the initial conditions, the cooling, star formation and feedback recipes, the treatment of the cosmic UV background, the simulation code and the numerical resolution, they all predict final stellar masses consistent with $\sim 10^8 M_\odot$ for dark matter haloes of $\sim 10^{10} M_\odot$. We give an overview of some of the relevant properties of these simulations in Table 5.1.

5.3 Initial Conditions

The parent simulation, as well as our high-resolution resimulations, are performed in the context of a ΛCDM cosmology, with $\Omega_\Lambda = 0.75$, $\Omega_m = 0.25$, h= 0.73 and $\sigma_8 = 0.9$, identical to the values used for the original Millennium simulation (Springel et al., 2005).

The Millennium-II simulation followed structure formation in a volume of 137^3 Mpc^3 using 2160^3 dark matter particles and periodic boundary conditions. This corresponds to a mass resolution of $9.43 \times 10^6 M_\odot$, and a force resolution of 1.37 kpc. At $z = 0$, it contains about 12 million Friends-of-Friends (FoF) haloes with at least 20 particles, corresponding to a minimum resolved halo mass of $1.9 \times 10^8 M_\odot$. Haloes of $\sim 10^{10} M_\odot$, the mass at $z = 0$ that we select for our resimulations, are resolved with over 10^3 particles.

Out of more than 10^4 haloes within our mass range in the MS-II, we identified 25 haloes as resimulation candidates, based on the condition that all particles within twice the virial radius at redshift $z = 0$ were in a connected region and inside a sphere of radius 0.67 Mpc in the initial conditions. Out of these, six
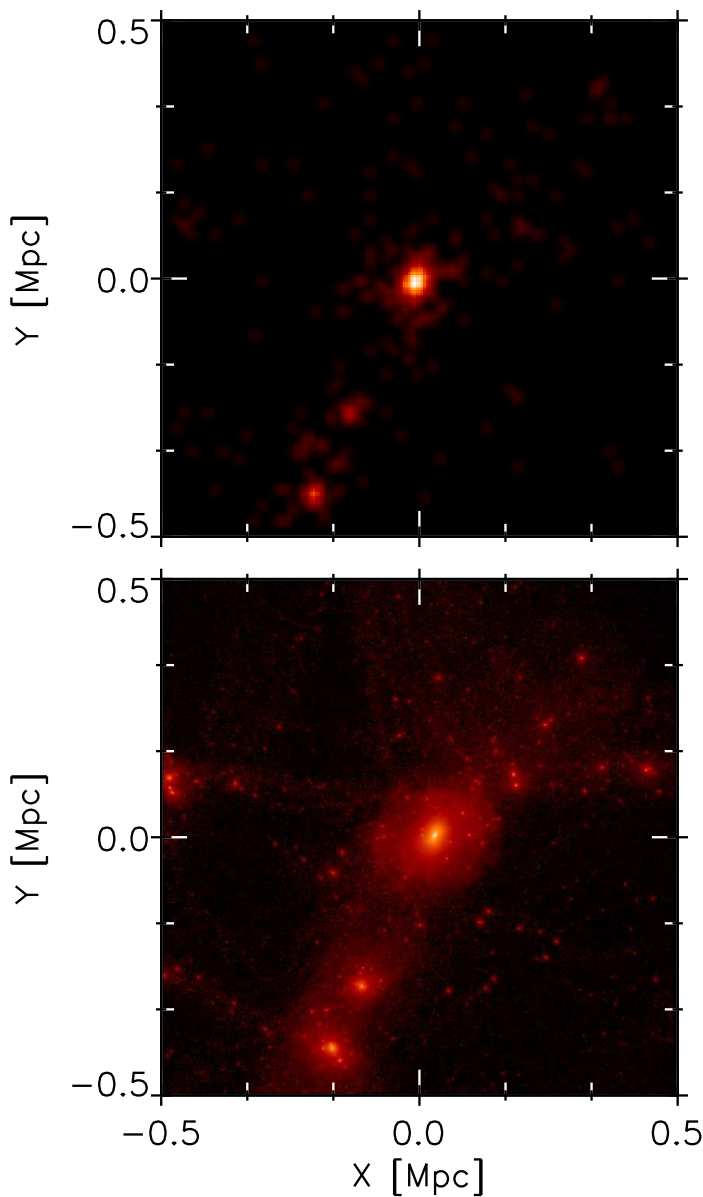
Figure 5.1: Comparison of Halo 4 at $z = 0$ in a pure dark matter resimulation and in the parent Millennium-II simulation. The top panel shows the dark matter distribution in a box of sidelength 1 Mpc in the original MS-II, while the bottom panel shows the distribution in the resimulation. Both panels are centred on the same absolute coordinates for the parent box of sidelength 137 Mpc, showing the position of the halo and the main substructures to be in perfect agreement, with additional substructures resolved in the resimulation. The FoF mass of the halo also agrees to within less than 1%.

haloes were selected in order to study a varied but representative sample of mass accretion histories (see Figure 5.2). The initial conditions for the resimulations were generated by re-sampling the region of interest with a high number of low mass dark matter particles, while the remaining volume was sampled with increasingly coarser resolution, sufficient to capture the long-range tidal field. To account for the higher Nyquist frequency of the resimulations, small-scale fluctuations were added to the displacement and velocity fields of the original MS-II using the method of second-order Lagrangian perturbation theory described in Jenkins (2010). The process of the initial conditions is also illustrated in Section 2.1.

Figure 5.1 shows the final distribution of dark matter particles in slices centred on a dwarf halo in the MS-II and in one of our high-resolution resimulations (pure dark matter). The difference in mass between the central FoF halo in the resimulations and in the MS-II is $< 1\%$, equivalent to ~ 10 particles in the parent simulation. The position and velocity are well reproduced, and the agreement also extends to substructures outside the main halo. The structure resolved in the MS-II is again found at the correct mass and location, while some additional substructure is visible only in the resimulation.

We have performed resimulations both with pure dark matter and with gas particles added, splitting each high-resolution dark matter particle at a mass ratio of $\Omega_{\rm b} = 0.046$ to $\Omega_{\rm DM} = 0.204$. All resimulations start at $z = 49$ and are evolved up to $z = 0$. The hydrodynamical simulations include 1.1×10^6 high resolution dark matter particles of $8 \times 10^4 {\rm M}_\odot$, and an equal number of gas particles of $1.8 \times 10^4 {\rm M}_\odot$. The initial stellar particle mass is $9 \times 10^3 {\rm M}_\odot$. At $z = 0$, the individual haloes are resolved with more than 10^5 particles within r_{200}. The volume outside of the high-resolution region is sampled with an additional 7.6×10^5 dark matter particles of varying mass to include the evolution of structure on large scales.

To check for possible biases due to our selection method, we have compared our candidates for resimulation to the total population of similar mass haloes in the MS-II. Figure 5.2 shows as solid lines the merger histories of the six selected dark matter haloes in the high resolution simulations, together with the typical mass accretion history, derived from merger trees of $\sim 10^4$ randomly selected, similar mass haloes. At each redshift, the inner and outer grey regions indicate the 3rd, 16th, 84th and 97th percentiles, equivalent to 1σ and 2σ deviations from the mean mass for a Gaussian mass distribution. It can be seen that the variance within our sample is higher than the expected variance within a random sub-sample of haloes. This allows us to follow the evolution of haloes with a range of merger histories in a limited number of simulations. However, there is no systematic bias in the mass accretion history of our haloes, so our sample can be considered a reasonably unbiased representation of $10^{10} {\rm M}_\odot$ haloes in the MS-II.
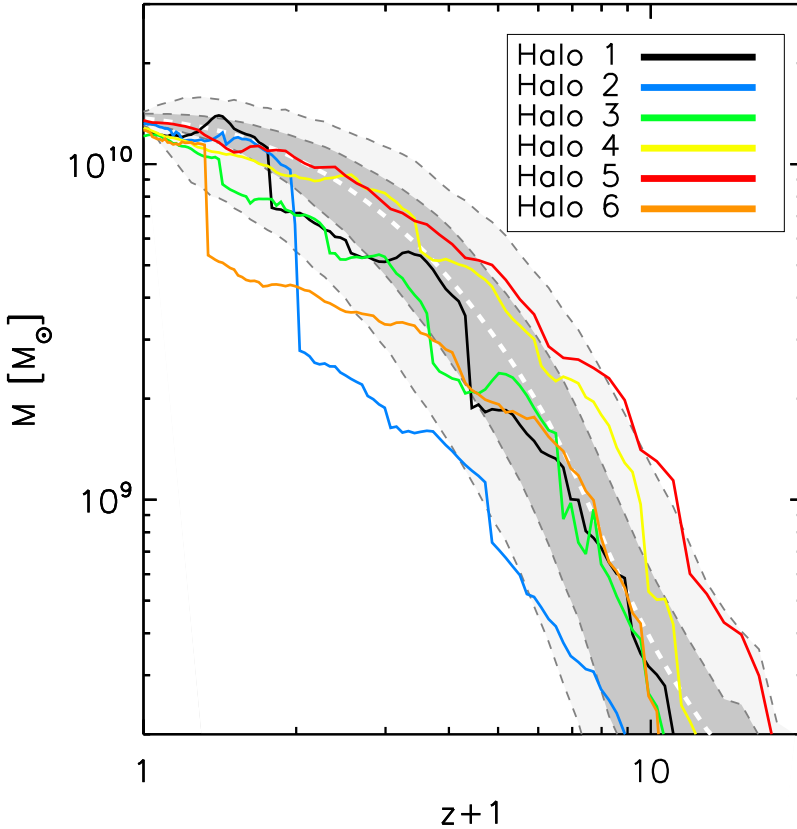
Figure 5.2: Evolution of FoF-halo mass as a function of redshift in our pure dark matter resimulations. The solid coloured lines show the mass accretion history of the six haloes we have resimulated at high resolution. Overplotted as a thick dashed line is the mean halo mass from the Millennium-II simulation, for all haloes of similar final masses. Also shown are the 1σ and 2σ upper and lower bounds at each redshift, in dark and light shades, respectively. It can be seen that there is a variety of assembly histories, both in the parent simulation, and in the sample of resimulated haloes. Haloes 3 and 6 have undergone recent major mergers, while Halo 5 formed significantly earlier than the five others. The variety within our sample is somewhat greater than expected for a random sub-sample of the MS-II, but there is no systematic bias in formation history. Formation redshifts, defined as the time when a halo reaches half its peak mass, lie between 1 and 2.5, consistent with a median formation redshift of 2. Note that the halo mass m_{200} can differ from the FoF-mass by $\sim 5 - 15\%$, and due to outflows, the total mass in each of the six haloes is reduced to $\sim 10^{10} M_\odot$ in the resimulations with gas.

5.4 Numerical Methods

The high-resolution simulations presented here have been performed using the Tree-PM code GADGET-3 (Springel, 2005; Springel et al., 2008), which includes gravity and smoothed particle hydrodynamics. As an extension, metal-dependent cooling, star formation, chemical enrichment and energy injection from type II and type Ia supernovae have been implemented in the multiphase gas model of Scannapieco et al. (2005, 2006). This model has previously been used to study the formation both of large disk galaxies (Scannapieco et al., 2008, 2009), and of dwarf spheroidal galaxies (Sawala et al., 2010). In Sections 5.4.1 to 5.4.5, we briefly explain the most important characteristics of this code, and refer the interested reader to the above references for a more detailed description.

5.4.1 Gravitational Softening

In order to reduce two-body interactions arising from the particle representation of the matter distribution, the gravitational potential is modified by replacing the divergent $1/r^2$ dependence with $1/(r^2 + \epsilon^2)$, where ϵ is the gravitational softening scale (Aarseth, 1963). The choice of ϵ represents a compromise between the errors due to residual two-body effects, and the loss of spatial resolution below several softening scales. We begin our simulations with a softening length fixed in comoving coordinates to 1/10th of the mean interparticle spacing for each particle type, corresponding to $\sim 1\mathrm{h}^{-1}$ kpc in the high resolution region. After the collapse of the halo, we keep the softening scale in this region constant in physical coordinates from $z = 7$, at a value of 155 pc. Power et al. (2003) give a lower limit $\epsilon_{acc} = r_{200}/\sqrt{N_{200}}$ to prevent strong discreteness effects in haloes, which corresponds to ~ 140 pc for a $10^{10}\mathrm{M}_\odot$ object resolved with $N_{200} \sim 10^5$ particles. We also resimulated one of our haloes, Halo 4, with a physical softening scale of 77.5 pc, and checked that this did not alter the results significantly.

5.4.2 Cooling and UV Background

Above the hydrogen ionisation temperature of 10^4 K, our gas cooling model is based on metal-dependent cooling functions of Sutherland & Dopita (1993). The model assumes collisional excitation equilibrium, and does not include metal or molecular cooling below 10^4K. In addition, we include Compton cooling, which is the main coolant at high redshift. It depends on the free electron density, as well as on the temperature difference between the gas and the evolving CMB. For this purpose, the ionisation states of H, He, and the free electron number density are computed analytically, following the model of Katz et al. (1996). We have included UV background radiation in our model, which adds a heating term to

the net cooling function of the partially ionised gas. In all simulations, the UV background is present from $z = 6$, and its spectral energy distribution and the time evolution of its intensity follow the model of Haardt & Madau (1996). A test simulation of Halo 4 without the UV background produced over twice as many stars by $z = 1$, compared to the simulation which includes UV radiation.

5.4.3 Star Formation Criteria

Cold gas particles can spawn, or be converted into, star particles, subject to certain conditions. We require the gas particle to be in a region of convergent flow. In addition, we impose a physical density threshold ρ_c on the local gas density. The existence of a threshold for star formation is motivated by observations (e.g. Kennicutt, 1989, 1998). Calculations by Quirk (1972) as well as numerical simulations, e.g. by Katz et al. (1996); Springel & Hernquist (2003); Bush et al. (2008) and others have shown that the observed Kennicutt-Schmidt relation can be reproduced in disk galaxies by imposing a volume density threshold, even though different values are assumed. Koyama & Ostriker (2009) demonstrated with high-resolution simulations of the turbulent interstellar medium that the star formation rate depends only weakly on the choice of ρ_c, and values in the range 0.1 cm^{-3} (Stinson et al., 2009) to 100 cm^{-3} (Governato et al., 2010) can be found in the recent literature. Governato et al. reported better convergence in their high-resolution simulation with a choice of 100 compared to 0.1. In this work, we adopt a value of 10 cm^{-3}. We have also tested a density threshold of 0.1 cm^{-3}, more similar to our own previous work. In this case, star formation starts at higher redshift and is less bursty. For Halo 4, the final stellar mass increases by $\sim 36\%$ with a threshold of 0.1 cm^{-3}. This difference is less than the variance in stellar mass between individual haloes, and does not qualitatively affect the stellar mass-halo mass ratio. The limited effect of ρ_c results from the fact that star formation is mostly self-regulating in our simulations. We also impose a threshold $\rho_{\mathrm{g}}/\overline{\rho_{\mathrm{g}}} \geq 10^4$ on the local gas overdensity relative to the cosmic mean, which ensures that star formation only takes place in virialized regions even at very high redshift.

5.4.4 Star Formation Efficiency

Subject to the constraints described in Section 5.4.3, the star formation efficiency is regulated by a single efficiency parameter $c_\star$, so that the star formation rate density is given by $\dot{\rho}_\star = c_\star \rho_g t_{\mathrm{dyn}}^{-1}$, where t_{dyn} is the local gas dynamical time. The creation of an individual stellar particle of mass $m_\star$ from a gas particle of mass m_g during the time interval Δt is stochastic, with probability given by:

$$p_\star = \frac{m_g}{m_\star} \left[1 - \exp\left(-\, c_\star \frac{\Delta t}{t_{\mathrm{dyn}}} \right) \right]$$

In simulations with radiative transfer, Gnedin et al. (2009) found that dust acts as a catalyst for molecular cloud formation, suggesting that star formation may be less efficient in the low metallicity environment of dwarf galaxies. As our simulations cannot follow cloud formation, we do not take this into account and assume a constant $c_\star$. Ricotti et al. (2002) showed that if star formation is strongly self-regulating, the star formation rate is determined primarily by the thermodynamic properties of the gas and depends only very weakly on $c_\star$. This result was confirmed in our previous work (Sawala et al., 2010), and in all simulations presented here, we adopt our earlier value of $c_\star = 0.05$.

Each star particle is produced with a single stellar population, whose metallicity is inherited from the parent gas particle. We assume a Salpeter initial mass function (Salpeter, 1955), and calculate stellar luminosities using the stellar synthesis model of Bruzual & Charlot (2003).

5.4.5 Multiphase Interstellar Medium and Feedback

For each star particle, we determine the rate as well as the yields of supernovae type II and type Ia. Chemical yields are calculated separately for the two types, following Woosley & Weaver (1995) and Thielemann (1993), respectively. Supernovae type II are assumed to be instantaneous, while supernovae type Ia follow a uniform delay time distribution between 100 Myrs and 1 Gyr. We assume a constant energy production of 7×10^{50} ergs per supernova, which is released into the interstellar medium (ISM) as thermal energy.

The multiphase scheme of Scannapieco et al. (2006) allows an overlap of diffuse and dense gaseous components. This preserves the multiphase structure characteristic of the ISM, in which components with very different temperatures and densities coexist. It also avoids the overestimation of density in diffuse gas near high density regions which can cause a serious underestimate of its cooling time. The decoupling is achieved by considering as neighbours in the SPH smoothing kernel only gas particles with similar thermodynamical properties, as defined by the ratio of their entropic functions.

Supernova energy is shared equally between the hot and cold phases. Cold particles which receive supernova feedback accumulate energy until their thermodynamic properties are comparable to those of their local hot neighbours. At this point, the energy is released and the particles are promoted to the hot phase.

We supplement Scannapieco et al. (2006) by including a seeding mechanism that defines reasonable properties for the local hot phase, even if no neighbouring particles are considered hot at the time. A cold gas particle which has received sufficient supernova energy to raise its thermodynamic properties to this level can thus be promoted, even if it currently has no hot neighbours. This ensures that the distribution of supernova feedback is not delayed at the earliest stages of star formation, when the entire interstellar medium can be in a cold and dense configuration (see Figure 5.3). The seeding mechanism does not create heat artificially and conserves energy. We have checked that the amount of gas required to seed the hot phase is small, and that the ensuing evolution of the two phases is consistent.

5.5 Galaxy Formation

The different merger histories of the dark matter haloes described in Section 5.3 are reflected in their gas accretion histories, and in the evolution of the galaxies that form within them. Section 5.5.1 describes the co-evolution of the halo and its galaxy, while Section 5.5.2 discusses the properties of the final objects.

5.5.1 Galaxy Evolution

The halo assembly histories vary significantly, both among our selected sample and among the total population of $10^{10} M_\odot$ haloes. As shown in Figure 5.2, haloes 3 and 6 had recent major mergers at $z = 0.32$ and $z = 0.21$, respectively, whereas haloes 1 and 2 experienced their last major mergers around $z = 1$. Haloes 4 and 5 have not undergone any major mergers since before $z = 2$. Halo 5 is also significantly more massive compared to the other haloes at high redshift.

The six panels in Figure 5.3 show the gas mass bound to each of the six haloes as a function of redshift. While the total coloured area indicates the total amount of gas in each halo, the star formation rate in the main progenitor, overplotted in black, depends on the presence of cold and dense gas, shown in red and orange colours. We find that two different mechanisms lead to a burstiness of star formation in our simulations. On timescales of hundreds of Myrs, self-regulation of star formation and supernova feedback lead to periodic variations in the gas density, and periodic star formation behaviour. This confirms the earlier results of Pelupessy et al. (2004), Stinson et al. (2007), Mashchenko et al. (2008), Valcke et al. (2008) and Revaz et al. (2009). In addition, gas-rich mergers can induce starbursts. These bursts are irregular and can be separated by several Gyrs. For example, the star formation episodes in Halo 4 beginning at $z = 8$, 4.3 and 2.1 are preceded by mergers at $z = 8.5$, 4.7 and 2.4 with haloes of 2×10^8, 3×10^8 and $10^9 M_\odot$, respectively, which bring in fresh gas.
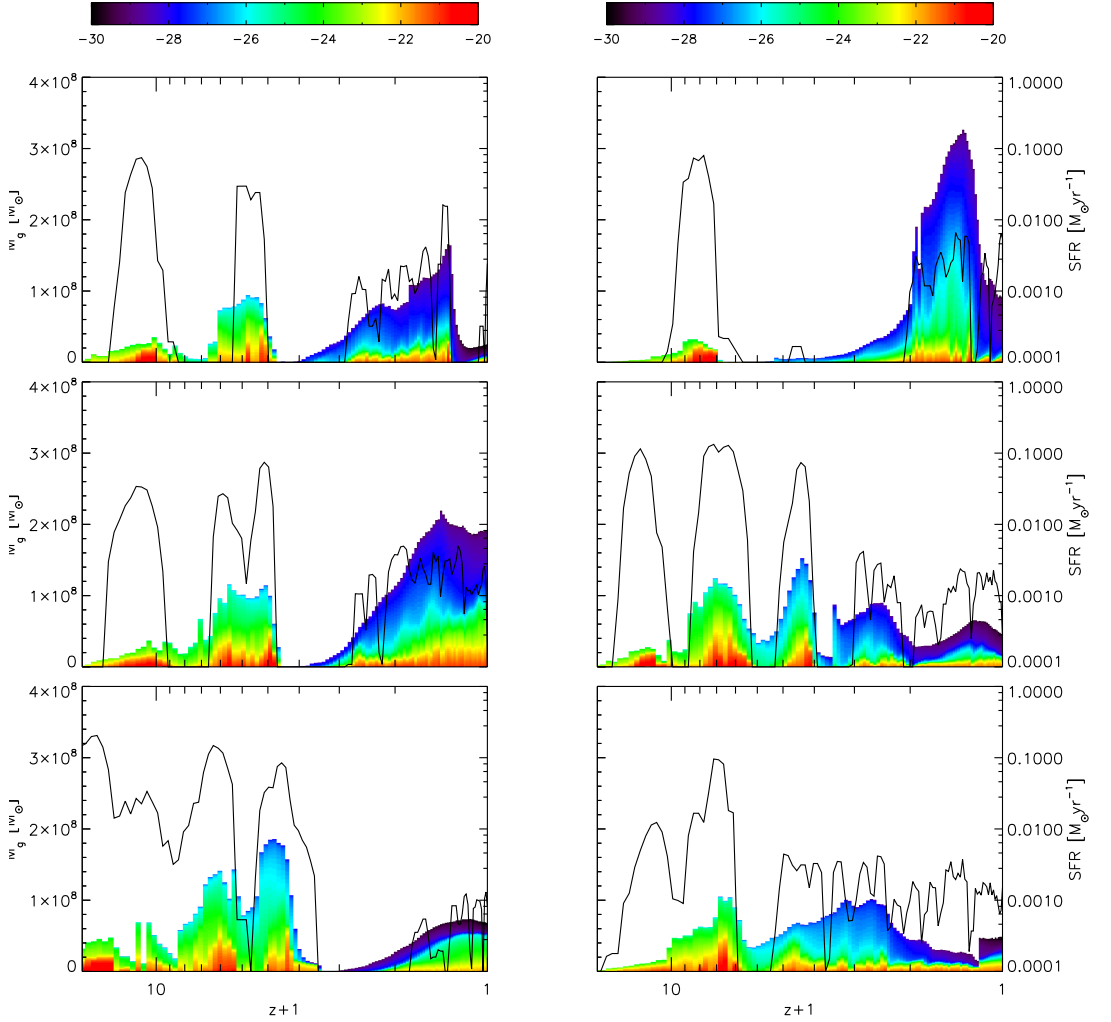
Figure 5.3: Evolution of total gas mass and star formation rate as a function of redshift. The top row shows, from left to right, haloes 1-3, while the bottom row shows haloes 4-6. The coloured area indicates the total amount of gas in each halo in units of $M_{\odot}$, corresponding to the scale on the left. The colour coding indicates the differential amount of gas at a given mass density in units of g cm^{-3}, as denoted by the colour bars above. Overplotted in black is the star formation rate as a function of redshift, in units of $M_{\odot}$ yr^{-1}, corresponding to the scale on the right. In each halo, star formation is tightly coupled to the amount of dense gas, and occurs in bursts, often separated by several 100 Myrs, and associated both with supernova feedback and with mergers. Halo 5 assembles earlier than the five others, and its significantly higher mass at early times leads to a more prolonged starburst in the galaxy contained within it. All galaxies are star-forming at $z = 0$.
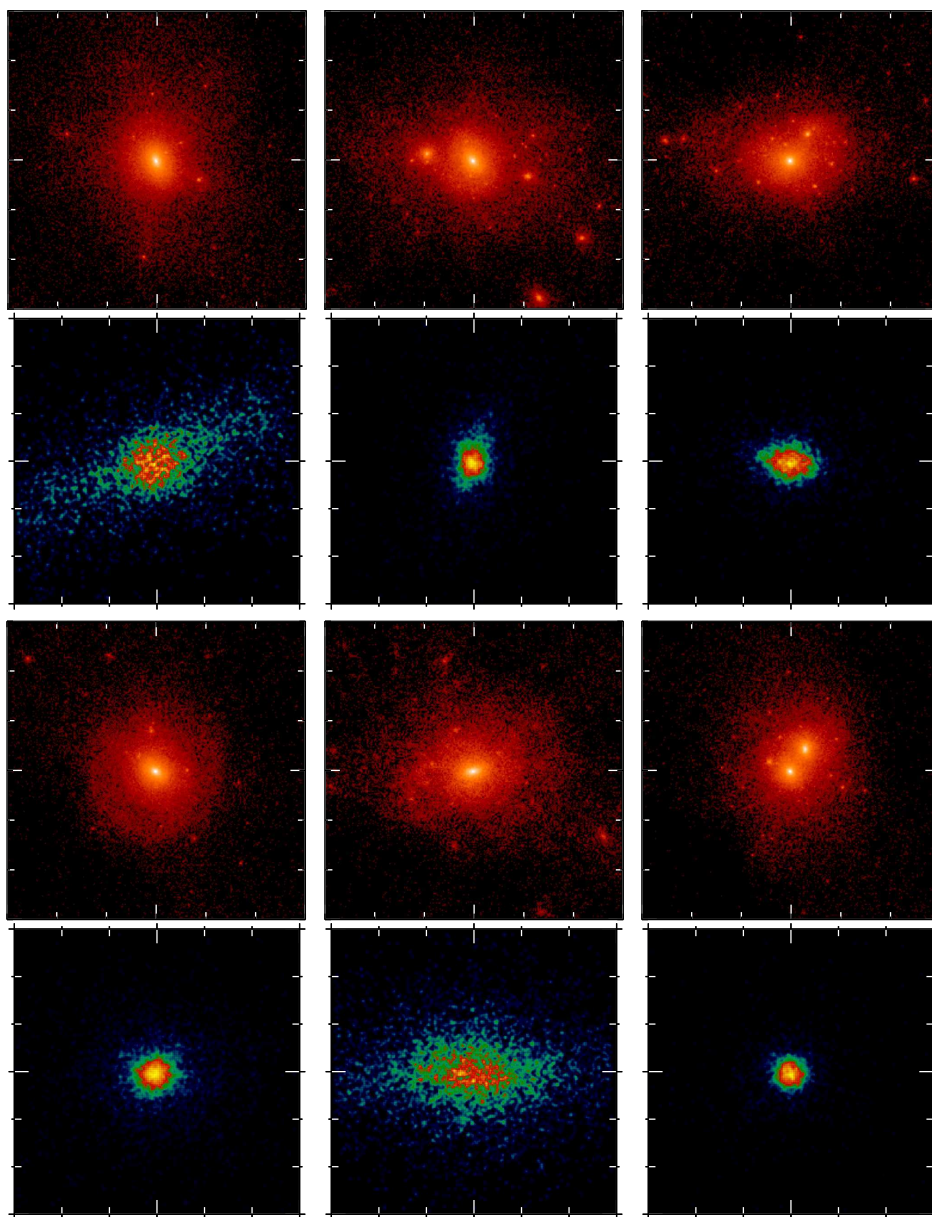
Figure 5.4: Distributions of dark matter (box size 200^3 kpc^3) and stars (box size 2^3 kpc^3) at $z = 0$ in haloes and galaxies 1-6, ordered from top-left to bottom-right. Only the galaxy in Halo 5 (bottom centre) has a stellar disk, whereas Halo 6 (bottom right), which had the most recent major merger, still shows the two progenitors.

Observations of periodic bursts lasting several hundred million years have been reported for three dwarf galaxies by McQuinn et al. (2009), while a number of dwarf galaxies (Leo I (Dolphin, 2002), Leo A (Cole et al., 2007), IC 10 (Cole, 2010), IC 1613 (Skillman et al., 2003), DDO 210 (McConnachie et al., 2006) and Carina (Koch et al., 2006b)) show extended, quiescent periods between star formation epochs. Cole (2010) suggest mergers and gas accretion as triggers for star formation, but note that individual bursts and mergers can no longer be linked observationally after several Gyrs.

The star formation history of each individual galaxy in our simulations reflects a combination of internal self-regulation via supernova feedback, and the supply of fresh gas via accretion and mergers. These two effects largely determine the variance in stellar mass between the haloes in our simulations; while differences in merger histories increase the variance, self-regulation via feedback decreases it. In our sample of six haloes of equal final mass, the galaxy stellar masses vary by about a factor of two.

Gas-rich mergers after $z = 6$ imply that the progenitors did not lose all their gas due to the UV background. In our simulations, such mergers occur with haloes that would reach masses above $\sim 10^9 M_\odot$ by $z = 0$. Sawala et al. (2010) showed that at this mass, a combination of UV and supernova feedback removes gas efficiently, while UV radiation alone is not always sufficient. Observations of Local Group dwarf spheroidals (e.g. Monelli et al., 2010) also suggest that reionization had at most a minor effect on these galaxies.

Some major mergers also contribute stars. The fraction of final stellar mass formed outside of the main progenitor ranges from $\sim 5\%$ in Halo 5, accreted at $z = 5.2$, to close to 40% for Halo 1, resulting from two major mergers at $z = 3.4$ and $z = 0.8$. Haloes 2 and 6 both accrete $\sim 25\%$ in mergers at $z = 0.4$ and 1, respectively, while haloes 3 and 4 accrete $\sim 7\%$ in mergers at $z = 0.5$ and $z = 2.4$. Since haloes 3, 4 and 5 follow a more typical assembly history, we expect the typical fraction of stars formed outside the main progenitor in dwarf galaxies of $M_\star \sim 10^8 M_\odot$ to be $< 10\%$, albeit with possible exceptions.

In general, we find that the mean metallicity evolves with age, indicating the recycling of enriched gas in subsequent generations of stars. At each stellar age, we also find a spread in metallicities, which indicates the incorporation of fresh material. However, we note that due to a lack of diffusive metal mixing, the metallicity spread in our simulated stellar populations can be as high as 3 dex, which is larger than observed.

Table 5.2: Overview of numerical simulation results

Halo	$M_\star$	M_g	M_{DM}	$r_{1/2}$	$\sigma_\star$	$L_\star$	Z_{MM}
	$[10^7 M_\odot]$	$[10^7 M_\odot]$	$[10^9 M_\odot]$	[kpc]	[km s^{-1}]	[km s^{-1}kpc]	
1	7.81	2.81	9.41	0.87	21	1.4	0.77
2	5.25	6.23	8.34	0.39	17	0.7	0.96
3	4.94	19.4	8.80	0.28	15	1.1	2.65
4	8.14	4.17	8.98	0.36	19	0.4	2.37
5	10.2	7.11	9.94	0.74	33	19	5.17
6	6.17	5.07	8.54	0.68	18	0.3	0.38

Notes: Col. 2: Stellar mass, Col. 3: Gas mass, Col. 4: Dark matter mass (all measured inside r_{200} at $z = 0$), Col. 5: Stellar half-mass radius, Col. 6: Deprojected 1-D RMS stellar velocity dispersion, Col. 7: Specific stellar angular momentum $L = |\mathbf{r} \times \mathbf{v}|$ ($\sigma_\star$ and $L_\star$ measured within 3 kpc), Col. 8: Redshift of last major merger (progenitor mass ratio $< 3 : 1$).

5.5.2 Galaxy Properties

Several properties of the six simulations are listed in Table 5.2. They appear to be in broad agreement with the previous studies discussed in Section 5.2. The final baryon fraction of the haloes are between 1.1 and 2.7 % of the total matter. The final stellar masses of the six galaxies fall between 4.9×10^7 and $1.0 \times 10^8 M_\odot$, which corresponds to stellar mass to total mass ratios in the range of $\sim 5 \times 10^{-3} - 10^{-2}$. All galaxies are star-forming at $z = 0$.

The final gas masses vary from 2.8×10^7 to $1.9 \times 10^8 M_\odot$. Observed dwarf galaxies of this stellar mass typically have a substantial HI content (e.g. Staveley-Smith et al., 1992; Geha et al., 2006; de Blok et al., 2008). In our simulations, we cannot directly measure the amount of HI gas. Defining the cold gas as the total amount of gas at temperatures below the peak of the cooling curve and correcting for the contribution of helium and metals, we derive approximate upper limits for the HI masses between 10^7 and $1.2 \times 10^8 M_\odot$. We adopt the notation of Geha et al. (2006) in defining the HI mass fraction as $f_{HI} = M_{HI}/(M_{HI} + M_\star)$, noting that He, H_2, hot gas and metals are neglected in the denominator. We derive upper limits for f_{HI} between 11% and 71% in our six galaxies with a median of 35%. In a sample of 101 flux-selected SDSS dwarf galaxies of similar stellar mass, Geha et al. find a higher mean HI fraction of 60%. However, individual galaxies show a large scatter in f_{HI}, with several as high as 95%, and others with upper limits below 10%.

The range of stellar half-mass radii in our six simulations is 0.28 to 0.87 kpc.

This is comparable to the typical values obtained by Geha et al. (2006) for half-light radii (r-band), even though the observed sample also contains a handful with half-light radii greater than 1.5 kpc. We note that only Halo 5, which has the most quiescent assembly history, contains a galaxy with a rotationally supported stellar disk, as reflected by the specific angular momentum $L_\star$. The other five haloes have more ellipsoidal morphologies and very little rotation. This is in contrast to the result of Governato et al. (2010), who report pristine disk galaxies in both of their simulations, albeit in haloes of 2.0 and $3.5 \times 10^{10} M_\odot$.

Observations also suggest that isolated dwarf galaxies of this stellar mass are more frequently disk-like (e.g. Hunter & Elmegreen, 2006; Geha et al., 2006). The latter find that 30% of edge-on dwarf galaxies show coherent rotation profiles, a number which drops to 18% when all axis-ratios are included, but this should be considered as a lower limit. In a volume-limited sample, Sánchez-Janssen et al. (2010) report that less than 30% of galaxies with stellar masses of $10^8 M_\odot$ have apparent axis ratios below 0.5, and less than 5% below 0.3 (their data is plotted in Figure 1.4 in Chapter 1). They attribute this flattening to stellar feedback. Compared to these observations, our simulated sample of six haloes is too small to assess the statistical significance of a 1 in 6 result. It should also be noted that the stellar half-mass radii of our galaxies are only resolved with a few softening lengths. Therefore, results on details of the galactic structure from our simulations are inconclusive.

5.6 Stellar Mass – Halo Mass Relation

In Section 5.3, we explained how we constructed our initial conditions from the parent simulation. Its large volume and high dynamic range allows us to demonstrate that we have resimulated a representative sample of haloes. We can therefore derive implications for the global population of galaxies that form in similar mass haloes, and compare with expectations from matching the observed stellar mass function to the abundance of haloes in a ΛCDM universe.

Assuming a monotonic relationship between stellar mass and maximum halo mass, Guo et al. (2010) have compared the abundance of haloes/subhaloes in the Millennium and Millennium-II simulations to the observed abundance of galaxies as a function of stellar mass obtained from the SDSS DR-7 by Li & White (2009). The observational sample contains over half a million galaxies at low redshift, and extends down to stellar masses of $10^{8.3} M_\odot$ with very small error bars. The combination of the two very large simulations also leads to very small errors on the theoretical halo abundance. The derived stellar mass to halo mass ratio peaks at $M_{halo} = 10^{11.8} M_\odot$ at a star formation efficiency of about 20%, and decreases both for more massive and for less massive haloes (see Figure 5.5). The decrease

in efficiency at the high mass end is generally attributed to AGN feedback (e.g. Croton et al., 2006; Bower et al., 2006), while the decrease for lower mass haloes is assumed to be due to the increasing efficiency of supernova feedback, and the effect of the UV background. This general behaviour was noted earlier from lower precision data by Navarro & Steinmetz (2000), Yang et al. (2003), Dekel & Woo (2003), Conroy & Wechsler (2009) and Moster et al. (2010).

Following Yang et al. (2003), Guo et al. (2010) adopted the following functional form for the mean stellar mass to halo mass ratio:

$$\frac{M_\star}{M_{halo}} = c \left[\left(\frac{M_{halo}}{M_0} \right)^{-\alpha} + \left(\frac{M_{halo}}{M_0} \right)^{\beta} \right]^{-\gamma}$$

They report an accurate fit to the data with parameters $c = 0.129$, $M_0 = 10^{11.4} M_\odot$, $\alpha = 0.926$, $\beta = 0.261$ and $\gamma = 2.440$. At the low mass end, the SDSS DR-7 data of Li & White extends to stellar masses of $2 \times 10^8 M_\odot$ with high accuracy, corresponding to a halo mass of $10^{10.8} M_\odot$. Guo et al. extrapolate this relation down to the lowest halo masses resolved in the MS-II. For halo masses of $\sim 10^{10} M_\odot$, this predicts a stellar mass of $\sim 8 \times 10^5 M_\odot$.

From a similar analysis based on SDSS DR-3, which extends to stellar masses of $3.2 \times 10^8 M_\odot$, Moster et al. (2010) also derive a stellar mass – halo mass relation, in good agreement with Guo et al. (2010) at the high mass end. They predict haloes of $10^{10} M_\odot$ to host galaxies with stellar masses of $\sim 5.7 \times 10^6 M_\odot$, significantly higher than found by Guo et al., but still an order of magnitude lower than our hydrodynamical simulations predict. Moster et al. note, however, that such haloes are at best marginally resolved at their mass resolution ($2.8 \times 10^8 M_\odot$), prohibiting a self-consistent treatment of subhaloes. Consequently, they only include haloes above $1.6 \times 10^{10} M_\odot$ in the conditional mass function. Moster et al. also apply their analysis to an analytic Sheth-Tormen mass function obtained by Vale & Ostriker (2006). In this non-parametric model, a halo mass of $10^{10} M_\odot$ corresponds to a stellar mass of $1.9 \times 10^6 M_\odot$, more similar to the value of Guo et al. (2010).

In Figure 5.5, we plot the stellar mass – halo mass relation of Guo et al. (2010) for haloes between 10^9 and $10^{12} M_\odot$. The solid section of the line shows the relation in the region directly derived from SDSS DR-7 data where the uncertainties are very small. The dashed section denotes an extrapolation to stellar masses below $10^{8.3} M_\odot$, assuming a faint-end slope of $\alpha = -1.15$ for the stellar mass function, as reported by Li & White (2009).

Studies of the faint-end of the stellar mass function are either limited to nearby regions or galaxy clusters, or require corrections for incompleteness and, in the case of photometric redshifts, background subtraction, which introduce considerable uncertainties (e.g. Christlein et al., 2009). As a result, different values for α in
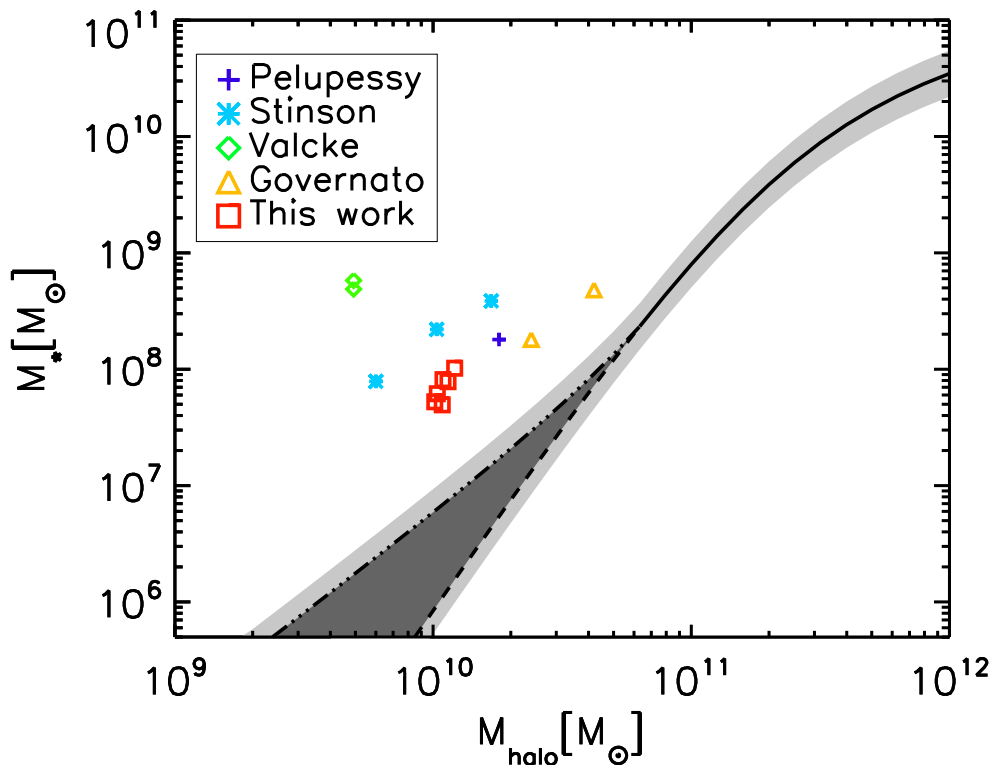
Figure 5.5: The stellar mass – halo mass relation, derived by Guo et al. (2010), compared to the results of several numerical simulations. The solid black line denotes the range constrained by the SDSS DR-7 data, while the dashed line is an extrapolation to lower masses, with a faint-end slope of −1.15 for the stellar mass function. The dark grey area shows the influence of a steeper faint-end slope up to −1.58 (dash-dotted line), while the light grey area represents the maximally allowed dispersion of 0.2 dex in $M_\star$ for a given halo mass. The coloured symbols denote the results of hydrodynamical simulations, as listed in Table 5.1 and Table 5.2, excluding simulations that did not evolve to $z = 0$ or assume a baryon fraction of 1% *ab initio*. The red squares indicate our own six simulations. For consistency, we use the halo masses of the pure dark matter simulations for our own simulations, and apply a correction of 20% to all other haloes, where this information is not available. All hydrodynamical simulations overpredict the stellar mass with respect to the observed relation by more than an order of magnitude.

the range of -1.1 to -1.6 are found in the recent literature (e.g. Trentham et al., 2005; Blanton et al., 2005; Carrasco et al., 2006; Baldry et al., 2008). The dark grey area in Figure 5.5 shows the effect of a steepening of the faint-end slope up to $\alpha = -1.58$, the value reported by Baldry et al. (2008). While this has a strong effect on the lowest mass haloes, we note that it cannot account for the discrepancy we find in haloes of $10^{10} M_\odot$. In order to fit the constraints of SDSS DR-7, the maximal dispersion at fixed halo mass is 0.2 dex in $M_\star$, indicated by the light-grey area. We overplot the results of our six simulations as red squares and add other $z = 0$ predictions from the studies listed in Table 5.1, correcting all halo masses for baryonic effects, as described below. It is apparent that all these hydrodynamical simulations overproduce stellar mass for their respective halo mass by at least an order of magnitude.

In Table 5.3, we compare the properties of our six simulations to the abundance matching predictions. We note that, due to the outflow of baryons, the total mass of our six haloes is almost a factor of $1 - \Omega_b/\Omega_m$ smaller than the masses of the corresponding haloes from the pure dark matter simulation. This effect is expected at such low star formation efficiency. For consistency with Guo et al. (2010), we therefore use the (higher) peak masses of the pure dark matter simulations in deriving the stellar mass predicted for each of our haloes by the abundance matching argument. For all galaxies listed in Table 5.1 whose peak halo mass cannot be defined or is not given, we increase the halo mass in Figure 5.5 by $\Omega_b/\Omega_m \sim 20\%$, the maximally expected correction.

Comparing the results of our simulations to the predictions, we find that the hydrodynamical simulations overproduce stellar mass by a median factor of ~ 50. Alternatively, abundance matching predicts that galaxies of $10^{7.9} M_\odot$, the median stellar mass produced in our hydrodynamical simulations, should reside in haloes with typical masses of $\sim 4.5 \times 10^{10} M_\odot$, rather than $10^{10} M_\odot$. If $10^{10} M_\odot$ haloes really hosted galaxies with $M_\star = 10^{7.9} M_\odot$, a ΛCDM universe would overpredict their abundance by a factor of ~ 4.

This discrepancy is too large to be attributed solely to incompleteness in the observed stellar mass function. Baldry et al. (2008) have used the stellar mass – surface brightness relation of SDSS galaxies in order to estimate the completeness at the faint end. Based on this analysis, Li & White (2009) estimate the completeness at $10^{8.3} M_\odot$ to be well above 70%. Following Baldry et al., the uncertainty in the number of $10^{7.9} M_\odot$ galaxies is much smaller than the discrepancy we report.

The difference is also unlikely to be attributable to numerical errors in our hydrodynamical simulations, or to the specific parametrisation of star formation and feedback in our model. From Table 5.1, it is clear that all other current hydrodynamical models, while succeeding in reproducing many of the observed features of individual dwarf galaxies, also predict similar or higher galaxy mass

Table 5.3: Comparison of stellar mass – halo mass ratios

Halo	$M_\star$	M_{tot}	M_{max}	$M_\star(SMF)$
	$[10^7 M_\odot]$	$[10^9 M_\odot]$	$[10^9 M_\odot]$	$[10^7 M_\odot]$
1	7.81	9.52	12.1	0.154
2	5.25	8.46	11.2	0.1216
3	4.94	9.04	10.7	0.104
4	8.14	9.10	11.8	0.143
5	10.2	10.1	12.5	0.171
6	6.16	8.65	10.7	0.104

Notes: Col. 2: Stellar mass obtained from simulation, Col. 3: Combined mass (m_{200}) of stars, gas & dark matter of the halo in the hydrodynamical simulation, Col. 4: Peak halo mass (m_{200}) in the pure dark matter simulation, Col. 5: Stellar mass corresponding to M_{max} from the abundance matching.

to halo mass ratios. They thus also fail to reproduce the low star formation efficiencies required to explain the observed abundances of dwarf galaxies in a ΛCDM universe.

Haloes of $10^{10} M_\odot$ are well resolved in the Millennium-II simulation, and the number of such haloes in a volume of 137^3 Mpc^3 is clearly large enough for statistical uncertainties to be small. While the assumed cosmological parameters of $\Omega_\Lambda = 0.75$, $\Omega_m = 0.25$ and $\sigma_8 = 0.9$ are only marginally consistent with the five-year WMAP data (Komatsu et al., 2009), this has a negligible effect on the mass function. It is unlikely that the number density of $10^{10} M_\odot$ haloes formed in a ΛCDM cosmology is significantly overestimated in our parent simulation. A lower value of σ_8 would slightly *increase* the abundance of haloes of this mass, but as Yang et al. (2003) have shown, the abundance matching result, which depends on the cumulative abundance of more massive haloes, is almost unchanged at $10^{10} M_\odot$ in ΛCDM.

In warm dark matter (WDM) models, structure is erased below a characteristic free-streaming length that depends on the assumed properties of WDM particles. Zavala et al. (2009) have compared the halo mass functions in high resolution dark matter simulations of ΛCDM and ΛWDM, assuming $m_{WDM} = 1$ keV, and find that the present-day abundance of haloes of $10^{10} M_\odot$ decreases by a factor of ~ 3. These simulations truncate the power spectrum of the initial conditions in the WDM case but neglect thermal velocities, which could increase the effect.

However, recent combined analysis of structures observed in the Lyman-α forest of SDSS and HIRES by Viel et al. (2008) suggest a lower limit of ~ 4 keV for thermal relics in a pure ΛWDM cosmology, which would allow only a much smaller deviation from CDM on these scales. While a WDM model could thus perhaps account for the reported discrepancy between simulations and star formation efficiencies inferred from abundance matching, the required WDM particle mass appears disfavoured by observation. A WDM solution would also significantly alter the internal structure of dwarf haloes, and simultaneously reduce the abundance of lower mass objects.

In principle, one could turn to direct measurements of halo masses for individual galaxies on the relevant scales, to elucidate whether the halo mass function of the ΛCDM model, and the inferred stellar mass – halo mass relationship, are correct. Direct mass estimates, through gravitational lensing (e.g. Mandelbaum et al., 2006) are only available for haloes with masses above $\sim 10^{11.8} M_{\odot}$, however, where they agree with the CDM predictions and the relationship of Guo et al.. For dwarf galaxies, one has to rely on HI rotation curves (e.g. de Blok et al., 2008), which do not give reliable estimates for *total* halo masses.

As demonstrated in Section 5.3, we have been careful to resimulate a representative sample of haloes, and to exclude any systematic bias. Considering the limited variance in stellar mass among the six haloes, statistical fluctuations are an unlikely source for the discrepancy.

It is worth noting that semi-analytical models of galaxy formation (e.g. Kauffmann et al., 1993; Cole et al., 2000) attempt to reproduce the observed faint-end slope of the stellar mass function in a ΛCDM universe by assuming highly efficient supernova feedback in small haloes (e.g. Benson et al., 2003; Khochfar et al., 2007). We have applied the semi-analytical model of Guo et al. (2010, b), which reproduces the Li & White (2009) stellar mass function, to the merger trees of our six resimulated haloes, and also to a randomly selected sample of similar mass haloes from the Millennium-II simulation. We find no difference in the predicted stellar mass between the selected haloes and the random sample, but stellar masses that are roughly two orders of magnitude smaller than in our hydrodynamical simulations. Independent of the cause of the discrepancy between the hydrodynamical simulations and the observed stellar mass function, there is thus a divergence between current hydrodynamical and semi-analytical models for dwarf galaxies. The semi-analytical models are tuned to produce the correct galaxy abundance, whereas hydrodynamical models aim at reproducing the physical processes and the structure of individual galaxies. Clearly, these two aspects cannot be treated separately, if we are to converge to a consistent picture of galaxy formation.

5.7 Summary

We have performed high-resolution hydrodynamical simulations of six $\sim 10^{10} M_\odot$ haloes, extracted from a large, cosmological parent simulation. We find that differences in merger histories lead to the formation of dwarf galaxies with different star formation histories and final stellar masses between 4.9×10^7 and $10^8 M_\odot$. These stellar masses agree with previous simulations of similar mass haloes, and the structure of our simulated galaxies resembles that of observed galaxies of similar stellar mass, to the extent which we can resolve structure in our simulations.

However, all these simulations imply an efficiency of conversion of baryons into stars which is at least an order of magnitude larger than that which is required to explain the observed abundance of dwarf galaxies in a ΛCDM universe. While current hydrodynamical simulations, including our own, are consistent with almost arbitrarily high mass-to-light ratios for the faintest galaxies in haloes of $10^9 M_\odot$ or less, they thus appear to be inconsistent with the mass-to-light ratios of larger dwarf galaxies, even when a moderately steep faint-end slope of the stellar mass function is assumed. The current recipes for mechanisms such as UV heating and supernova feedback appear sufficient to remove the "Missing Satellites Problem" for the smallest satellites. However, isolated dwarf galaxies with stellar masses of $10^8 M_\odot$ are still substantially overproduced in current hydrodynamical simulations, even when these mechanisms are included.

Our results suggest three possible explanations: The current observational count of dwarf galaxies could be incomplete, underestimating the true number density of $10^8 M_\odot$ galaxies by a factor of four or more. In that case, the hydrodynamical simulations could be correct, but the semi-analytical models that produce low abundances of dwarf galaxies have been tuned to incorrect data.

If the count of dwarf galaxies is almost complete at $10^8 M_\odot$, these galaxies must, in a ΛCDM universe, be residing in haloes significantly more massive than $10^{10} M_\odot$, and all current hydrodynamical simulations overpredict the efficiency of star formation by more than a factor of ten. This could be an indication of numerical problems, or, more likely, of incorrect or incomplete assumptions about the relevant astrophysics. Several possible mechanisms may contribute to a star formation efficiency in current simulations that is too high compared to real galaxies:

- Supernova feedback may be more efficient in ejecting gas from dwarf galaxies than current hydrodynamical simulations predict. For example, Guo et al. (2010, b) showed that the observed stellar mass function can be reproduced in semi-analytical models by assuming very strong mass-loading of winds in low mass haloes.

- The full effect of reionization on the IGM may not be captured in current models. As a result, cooling times may be underestimated, and the fraction of gas-rich mergers overestimated. Local sources of extreme UV and soft X-ray radiation may also ionise the interstellar medium, inducing another self-regulation mechanism for star formation (Ricotti et al., 2002; Cantalupo, 2010).

- Low dust content may lead to less efficient cloud formation and shielding at low metallicities. The transformation rate of cold gas into stars, currently assumed to be universal, may therefore be overestimated in dwarf galaxy simulations (Gnedin et al., 2009).

- Processes such as magnetic fields, cosmic rays and the feedback from population-III stars are not included in any of the current models, and may further reduce the star formation efficiency.

Any revised model would however still have to reproduce features of individual galaxies consistent with observations. We also note that a model which substantially decreases the number of $10^8 M_\odot$ galaxies would imply that the halo masses of fainter dwarf galaxies would need to be revised upwards, as some of these would now be required to live in $10^{10} M_\odot$ haloes.

If the observed stellar mass function is complete, and the hydrodynamical simulations correctly capture the relevant physics of galaxy formation, the Millennium-II simulation (and similar ΛCDM simulations) overpredict the number of $10^{10} M_\odot$ dark matter haloes. This would seem to require the underlying physical assumptions of the ΛCDM model to be revised. Warm dark matter may offer a possibility, but only for particle masses of ~ 1 keV, below the limit apparently implied by recent Lyman-α observations.

Of the three proposed scenarios, it appears that missing astrophysical effects in the simulations are the most likely cause of the discrepancy, and the most promising target in search of its resolution. While the three scenarios differ in nature, none is without significant implications for galaxy formation, which will have to be addressed in the future.

The Dwarf Galaxy Population in Semi-Analytical Models: Not the Sum of its Parts?

6.1 Introduction

Direct hydrodynamical simulations, including those presented in Chapters 3 – 5, aim at understanding galaxy formation by replicating the relevant physical processes as accurately as possible. Often starting from cosmological initial conditions, they purport to investigate how the laws of gravity, hydrodynamics and thermodynamics determine the formation and evolution of individual objects, which can be compared to the galaxies we observe. The principles and some technical aspects of this method are described in Chapter 2. Despite their success at reproducing the features of individual galaxies (of which there are many examples, e.g. Governato et al., 2004, 2010; Scannapieco et al., 2009), current direct simulations still lack the dynamic range and time resolution required to simultaneously capture the formation of a galaxy in its cosmological context (r > 1 kpc, $\sim 10^{20}$m; $t_0 \sim 10^{10}$ yr), and to resolve the physics of star formation or supernova feedback (r < 1 Au $\sim 10^{11}$m; $t_{FF}(MC) \sim 10^6$ yr).

As shown in Chapter 4, the task becomes increasingly more difficult if larger galaxies, or galaxies and their environment, have to be taken into account. Processes that cannot be resolved directly have to be parametrised, and those parameters which cannot be fixed ab initio, or constrained by independent observations, become additional degrees of freedom of the model. In current simulations, these include the efficiency of converting cold gas into stars, the stellar initial mass function which determines the number of supernova progenitors, the amount of supernova energy release and its distribution, and large parts of the radiation

transport and cooling mechanisms of the interstellar gas. Rather than predicting the formation of galaxies completely from "first principles", results of simulations have to be compared to observations of real galaxies, and parameters adjusted iteratively, if required.

In some sense, semi-analytical models (White & Frenk, 1991; Cole, 1991; Kauffmann et al., 1993), take an orthogonal, phenomenological approach: Their basic assumption is that the principal mechanisms of galaxy formation can be cast in the form of analytic equations, with boundary conditions given by the cosmological formation of structure, and the observed galaxy population. While relations applied in semi-analytical models are assumed to emerge from the fundamental equations of nature, these do not have to be solved (or even known) explicitly. For example, whereas hydrodynamical simulations may attempt to *compute* the gas cooling rate directly (at least in principle) from atomic and molecular physics, the cross sections of various processes, and the hydrodynamic equations determining the local temperature and density distribution; semi-analytical models *calibrate* the cooling rate by comparing the model predictions to the observed galaxy population. Whereas hydrodynamical simulations attempt to compute the effect of supernova feedback using *known* processes such as the release of thermal energy (or *known unknown* processes like cosmic ray production), semi-analytical models may include a parameter such as wind-mass-loading, which, if calibrated correctly, automatically takes into account *all* processes that give rise to the phenomenon.

In the place of the continuous density distributions found in direct simulations, the basic unit that links the dissipationless dark matter to the observable galaxies in most semi-analytical models are the so called merger trees of haloes and subhaloes, which may be generated from Press-Schechter theory (e.g. Cole et al. (2000), also see Section 1.3.2), or from a numerical pure dark matter simulation such as the MS-II. Haloes and subhaloes are characterised by variables such as mass, concentration and spin. Baryons are assigned to each branch of the tree, according to the equations of the semi-analytical model. The formation and evolution of galaxies depends on the specified recipes, which can also account for mergers and interactions of haloes. Galaxy properties predicted can include stellar masses, colours and ages, star formation, AGN activity, and cold and hot gas content. The results are typically not quoted for individual objects, but in statistical terms, for the galaxy population as a whole, or for sub-populations divided by mass, colour, environment, etc. Important statistical observables include the stellar mass function and derived properties such as the universal star formation rate, as well as spatial correlation functions. Semi-analytical models thus represent a simple way of connecting a numerical dark matter only simulation to the universe observable through galaxy surveys.

In principle, there is no limit to the number of parameters in semi-analytical models, which can lead to degeneracies, as discussed by Neistein & Weinmann (2010). The high degree of parametrisation can also be considered an advantage: whereas current hydrodynamical simulations contain a mix of ab initio physics, known sub-grid recipes such as the IMF, and unknown effects inherent to the numerical implementation, semi-analytical models only contain explicit parametrisations, which leads to a more intuitive interpretation of their results. Combined with the small computational cost of semi-analytical models, this makes it much simpler to test general models of galaxy formation, and thereby make predictions as well as derive constraints for the model. Provided that there is no degeneracy, successful semi-analytical models identify the general relations of galaxy formation; direct simulations connect them to micro-physical laws.

6.1.1 From Galaxies to Galaxy Populations (and back)

Whereas hydrodynamical simulations can resolve the evolution of individual galaxies in some detail, the strength of semi-analytical models is in the predictions for a population or sub-population of galaxies.

However, it is worth remembering that there are areas where the predictions of both methods overlap. Although the results of semi-analytical models are presented only in statistical terms, these are derived from a summation over individual objects. Naturally, the properties of the galaxy population has to arise from the properties of individual galaxies, to the degree that they are resolved by the model, if the model has any correspondence to the physical world. Conversely, as discussed in Chapter 5, if the initial conditions are chosen carefully, the results of hydrodynamical simulations also carry significance for the galaxy population as a whole, even though only a finite number of individual objects are computed explicitly.

The historic distinction between the realms of individual galaxies and the galaxy population has meant that the two techniques have seldom interfered. This is particularly true for dwarf galaxies, where large cosmological simulations have previously lacked sufficient resolution to construct low-mass merger trees, and hydrodynamical simulations have used specially created initial conditions, with no possibility of comparison to semi-analytical models. With the Millennium-II simulation, and the re-simulations presented in Chapter 5, this is no longer the case: they allow, for the first time at this mass range, to directly compare the two methods, not only on similar mass systems, but on the exact same objects. (A comparison of ordinary galaxies in a massive galaxy cluster is discussed in Saro et al. (2010).)

6.2 Different Semi-Analytical Models

The semi-analytical model of Guo et al. (2010) has been the first to be applied to the Millennium (MS) and Millennium-II (MS-II) simulations simultaneously, and succeeded in reproducing the SDSS stellar mass function over five orders of magnitude, from 10^7 to $10^{12} M_\odot$. Guo et al. also include a comparison with the widely-adopted model of De Lucia & Blaizot (2007), which had previously been applied to the MS alone. They find that the model of De Lucia & Blaizot over-predicts the stellar masses of the lowest mass galaxies when applied to the MS-II. In Guo et al. (2010), this is resolved by increasing the supernova efficiency, while decreasing the reincorporation of ejected gas, but as the authors note, the best-fitting model is not unique at the present level of observational constraints. A comparison between the model of Guo et al. (2010) and our hydrodynamical simulations is given in Section 6.4.

Neistein & Weinmann (2010) have investigated the degeneracy of semi-analytical models, and constructed a simple model, designed to be of minimal degeneracy. Here, galaxies are represented as four-component systems, described by their mass in dark matter, cold gas, hot gas and stars. Three principal efficiency functions control the evolution of galaxies at the low mass end: the cooling efficiency f_c, the star formation efficiency f_s and the feedback efficiency f_d.

- The cooling efficiency f_c describes the transformation of hot gas m_h to cold gas m_c due to cooling processes:

$$\dot{m}_c|_{cooling} \quad \equiv \quad -\dot{m}_h|_{cooling} \quad = \quad f_c \cdot m_h \qquad (6.1)$$

  The cooling efficiency function is assumed a function of the host halo mass and cosmic time t only, and has dimensions of $Gyrs^{-1}$.

- The star formation rate $\dot{m}_\star|_{SF}$ is assumed proportional to the cold gas mass, and controlled by an efficiency parameter f_s:

$$\dot{m}_\star|_{SF} \quad \equiv \quad -\dot{m}_c|_{SF} \quad = \quad f_s \cdot m_c \qquad (6.2)$$

  .

- The re-heating of gas due to supernova feedback can promote gas from the cold to the hot phase, at a rate determined by the star formation rate, and by a feedback efficiency parameter f_d:

$$\dot{m}_h|_{FB} \quad \equiv \quad -\dot{m}_c|_{FB} \quad = \quad f_d \cdot \dot{m}_\star|_{SF} \quad = \quad f_d f_s \cdot m_c \qquad (6.3)$$

  .

With parameters of ($f_c = 6/t, \quad f_s = 3, \quad f_d = 3.5$), Neistein & Weinmann (2010) show that this general model reproduces the results of De Lucia & Blaizot (2007) when applied to the Millennium simulation. Whilst the model does not make the same number of predictions as more sophisticated models, like the one of Guo et al. (2010) which also predicts galaxy morphologies and colours, the simplicity of the Neistein & Weinmann model makes it easily adjustable to different constraints.

6.3 Common Initial Conditions

An object-by-object comparison of direct simulations and semi-analytical models requires a common set of initial conditions. These are provided by pure dark matter zoom simulations based on a larger cosmological volume, to which the semi-analytical model is applied. As described in Section 2.1, six haloes of $\sim 10^{10} \mathrm{M}_\odot$ at $z = 0$ were chosen from the MS-II for the resimulations presented in Chapter 5, which only represent a small subset of the total population of similar mass haloes was suitable for resimulation. As shown in Figure 5.2 of Section 5.3, these objects were selected, so that their mass assembly histories represented the general population of equal mass haloes, in order to avoid formation bias.

6.4 Blind Comparison

Before running the full hydrodynamical simulations of Chapter 5, but after comparing the merger histories to avoid selection effects, the predictions of galaxy formation within the selected haloes were also checked, using the semi-analytical model of Guo et al. (2010). Figure 6.4 shows the predictions of stellar mass as a function of halo mass for all haloes which met the requirements for resimulation (blue circles), together with the predictions for the total population of haloes of similar mass (red points). It can be seen that the criteria for resimulation do not introduce a bias in terms of the stellar masses predicted by the semi-analytical model. The six filled circles represent the final selection of haloes, which also constitute an unbiased sample of the total population.

It was reported in Chapter 5 that the stellar masses predicted by the hydrodynamical simulations exceeded the results obtained from abundance matching by almost two orders of magnitude. A similar discrepancy is to be expected when comparing the results of the simulations to the results for the same six haloes in a semi-analytical model, which has been tuned to globally reproduce the abundance matching result. Figure 6.2 compares the results of the two methods in terms of the stellar masses and gas masses, predicted for each object. As anticipated, the median stellar mass in the hydrodynamical simulations is $\sim 10^{7.9} \mathrm{M}_\odot$, compared
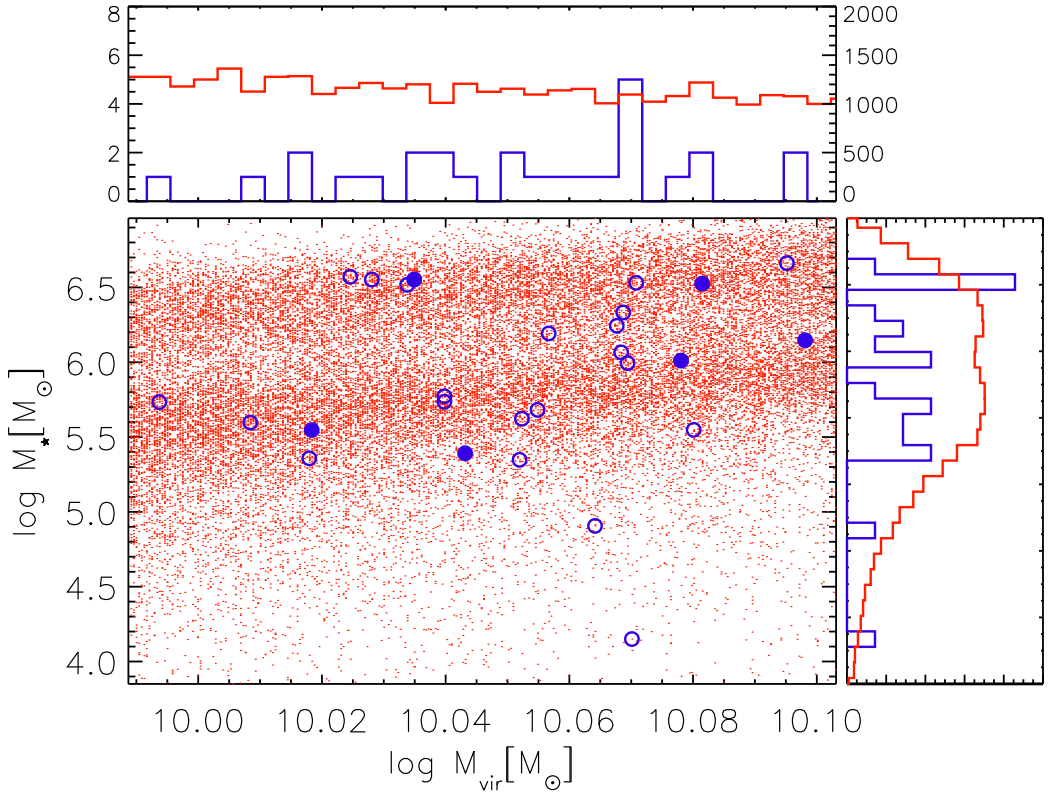
Figure 6.1: Stellar mass as a function of halo mass, as predicted by the semi-analytical model of Guo et al. (2010). The blue circles denote the haloes suitable for resimulation, from which the six haloes denoted by filled circles were selected. Overplotted in red are the predictions for the complete sample of $\sim 20,000$ haloes with masses close to $10^{10}\mathrm{M}_\odot$ in the MS-II. The top and side panels show deprojections of the distribution of the virial and stellar masses, respectively. It can be seen that the selection introduced no significant bias.
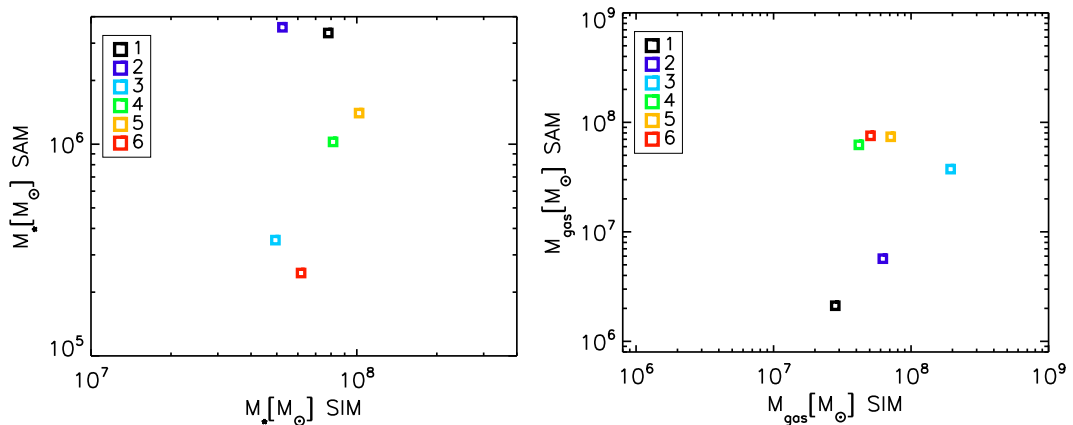
Figure 6.2: Comparison of the stellar mas (left panel) and gas mass (right panel) for the six haloes in the numerical simulation and semi-analytical model. It can be seen that the mean stellar mass is higher by almost two orders of magnitude in the simulation, while the gas masses are roughly comparable. However, there is not simply a shift in the mean; there appears to be no correlation between the objects in both methods.

to $\sim 10^6 M_\odot$ in the semi-analytical model, which is a serious concern for dwarf galaxy formation physics. At $\sim 10^{7.5} M_\odot$, the gas masses are similar in both cases, but this implies that the gas fractions, or the gas masses assigned to galaxies of the same stellar mass, also differ by more than an order of magnitude.

Also worth noting is the lack of any correlation between individual objects in the two models: the stellar masses and gas masses assigned to each galaxy appear to be random. Not only is the star formation efficiency much higher in the hydrodynamical simulations, the two methods also do not agree on which of the haloes should have a higher or lower relative star formation efficiency. While all six galaxies in the hydrodynamical simulations are star-forming at $z = 0$, the same is true for only one galaxy in the semi-analytical model.

As noted in Section 5.7, the discrepancy between the hydrodynamical results and the abundance matching result reported in Chapter 5 may have three possible explanations: an incorrectly measured stellar mass function, an underlying cosmology different from ΛCDM, or missing or misrepresented ingredients of the physical models of the simulations. By contrast, the object-by-object comparison between the simulations and the semi-analytical model does not directly depend on the observed stellar mass function. Since both methods also take the same

cosmological simulation as a starting point, the discrepancy must be entirely attributable to a different physical model (apart from resolution effects, addressed in Section 6.6 below).

6.5 Connecting Both Methods

To understand the cause of this discrepancy, we used the semi-analytical model of Neistein & Weinmann (2010), described in Section 6.2. As a starting point, we tune the model to reproduce the model of De Lucia & Blaizot (2007), which is known to give a reasonable fit to the stellar mass function.

Figure 6.3 shows a comparison of the six haloes of Chapter 5, in the hydrodynamical simulations (denoted by solid lines), and in the semi-analytical model tuned to the model of De Lucia & Blaizot (2007), applied to the respective merger trees in the MS-II (dashed lines). In each case, the same main progenitor is followed backwards in time, according to the stellar mass in the simulation. The dashed lines originate at lower redshift, because of the lower mass resolution in the MS-II compared to the re-simulations. The main difference, however, is in the evolution of the galaxies: as in the case of the Guo et al. (2010) model, the semi-analytical model produces much lower stellar masses compared to the simulations, and the evolution of the baryonic components in individual objects appears to show no correlation between the two methods.

In a second step, the cooling efficiency f_c, star formation efficiency f_s and feedback efficiency f_d in the Neistein & Weinmann model have been tuned to the hydrodynamical simulations. It was found that a common set of parameters exists, which gives a good match to each of the hydrodynamical simulations. Figure 6.4 shows a comparison of the time evolution of the six objects with the new model, similar to Figure 6.3. Now, there is a good agreement, not only in terms of the final stellar mass, but also in the star formation over time. Furthermore, the agreement is not only on the mean, but also extends to individual objects, and their respective star formation histories according to both methods. The hot and cold gas content, however, are still not well matched; the total gas masses are in better agreement compared with Figure 6.3, but in each case, the hydrodynamical simulations assign more cold, and less hot gas to the galaxies, compared to the semi-analytical model.

6.6 Extrapolation

Ideally, a semi-analytical model which is tuned to match the hydrodynamical simulations can be used to extrapolate the results from individual galaxies to the entire galaxy population of the parent simulation. This would not only give
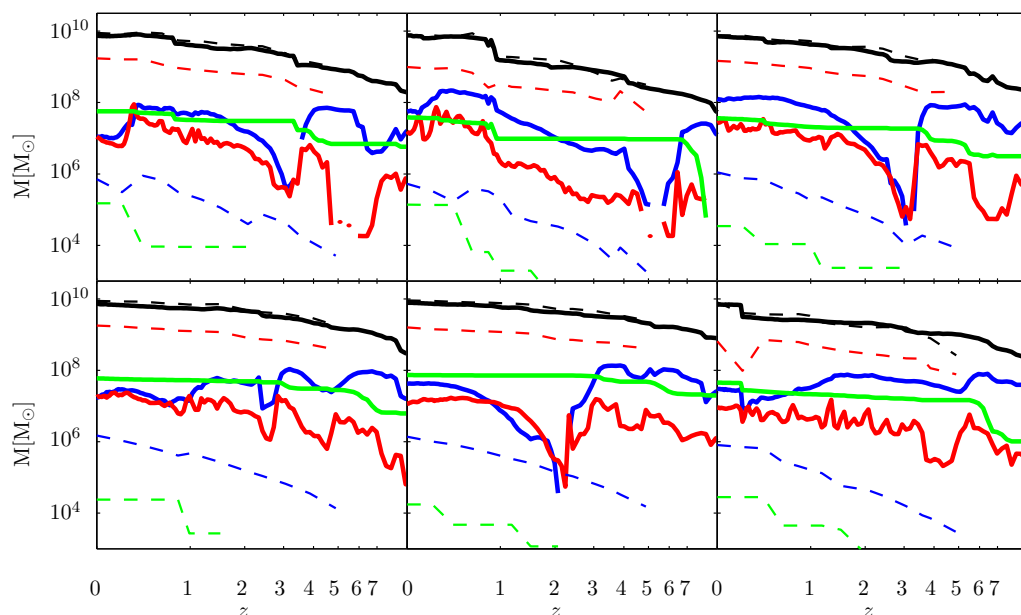
Figure 6.3: The evolution of the six objects, in hydrodynamical simulations (solid lines), and a semi-analytical model (dashed lines) tuned to reproduce the abundance matching results at $z = 0$. In each panel, the black lines denote the mass in dark matter, green lines denote the stellar mass. Blue and Red lines denote the "hot" and "cold" gas component. The results of the semi-analytical model has little resemblance with the hydrodynamical simulation. Also note that the lines for the semi-analytical models begin at lower redshift, owing to the fact that objects are defined later in the lower resolution MS-II.

a simple and direct way of calculating the stellar mass function and its scatter (which would require a high number of individual galaxy simulations), but also allow a calculation of observables such as the clustering strength, which are not accessible by *any* number of single-object simulations. With the current model, however, there are several limitations:

- The model has been tuned at one final mass only, which has removed, to a large extent, the mass-dependence of the efficiency functions. An extrapolation to different masses would entail degeneracies which the present simulations cannot constrain.

- The semi-analytical model and the hydrodynamical simulations have been applied to the same objects, but at different resolutions. Bound structures
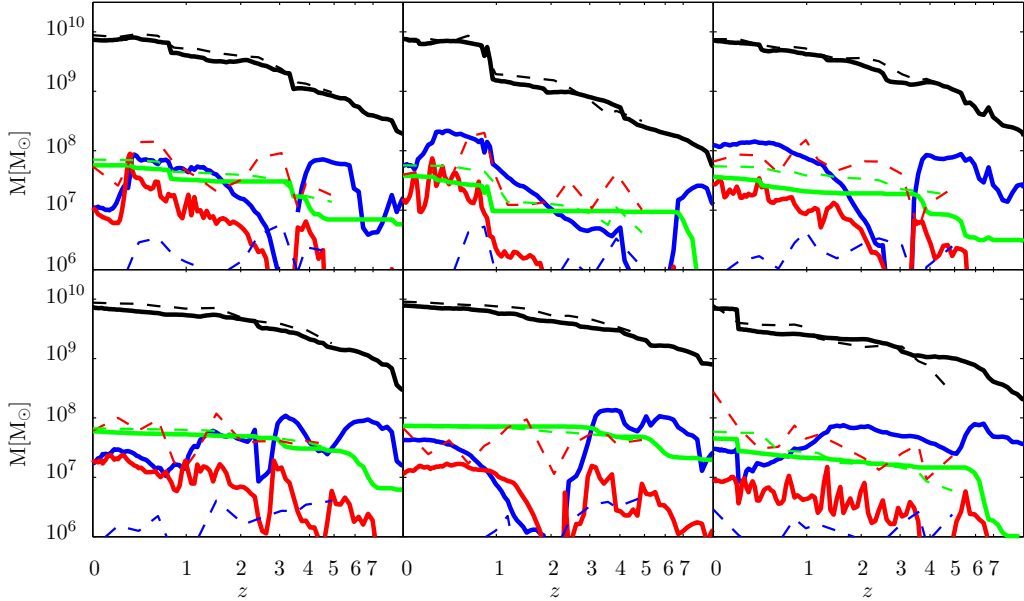
Figure 6.4: The evolution of the same six objects shown in Figure 6.3, now comparing between hydrodynamical simulations (solid lines), and the best fitting semi-analytical model (dashed lines). Note that the mass range on the Y-axis is different compared to Figure 6.3.

are identified earlier in the resimulation, and star formation begins earlier as a result. Just as the increase in resolution by a factor of 125 from the MS to the MS-II has required adjustments to the semi-analytical model (Guo et al., 2010), a similar increase in resolution may require further (minor) adjustments. The time-resolution of the resimulations is also twice as high as that of the parent simulation.

- The correspondence of quantities across the two methods is not fully established. The formalism of Neistein & Weinmann (2010) attempts to represent galaxies in simple terms, consisting only of $m_\star$, m_c and m_h, which should be less ambiguous to identify in simulations, compared to cooling radii or disk and bulge components of more sophisticated models. However, such a simplified model could be *over*-simplified. In that case, an accurate match to the simulations (which naturally take the spatial distribution into account), in terms of these simple parameters only, may not correspond to an actual correspondence of the physical models.
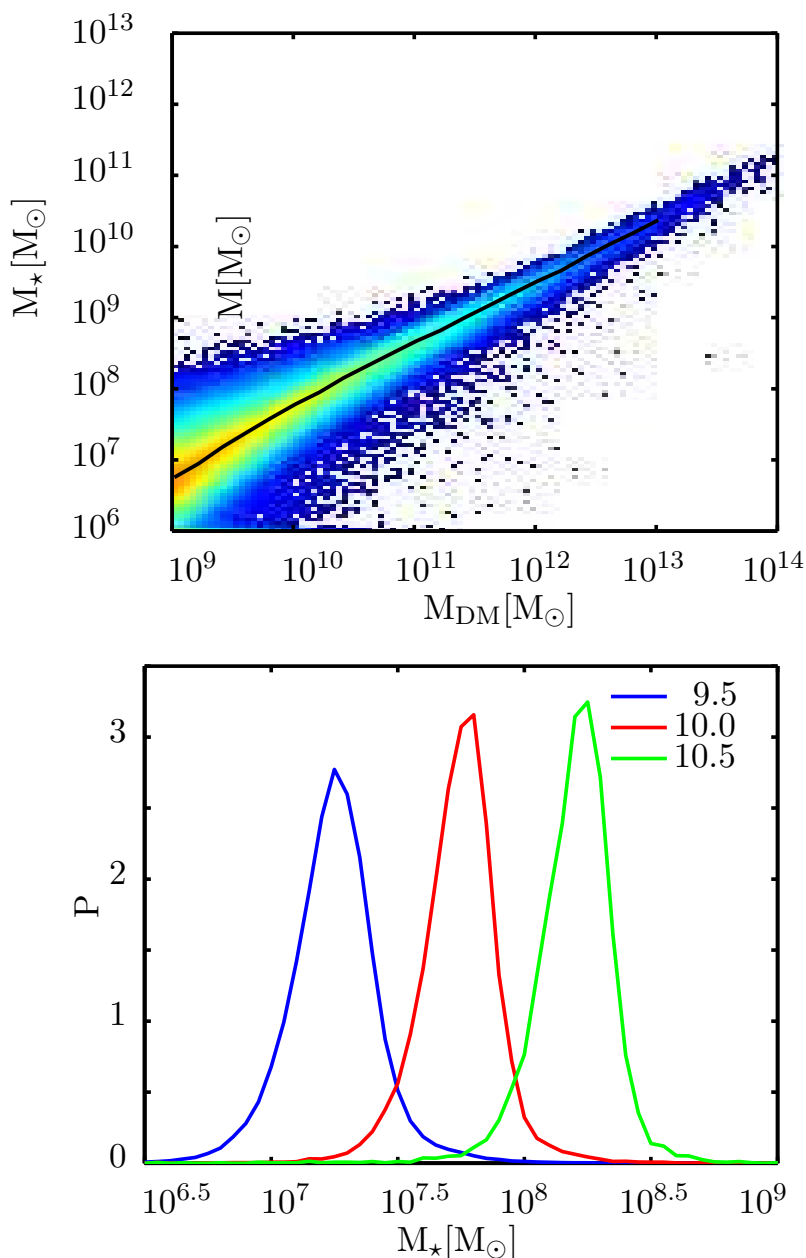
Figure 6.5: Stellar mass as a function of halo mass for central galaxies, predicted by the tuned semi-analytical model. In the top panel, the solid line denotes the median stellar mass. In the bottom panel, the three curves show the probability distribution for the stellar mass in three different bins of halo mass. The model shows an increase in scatter for lower halo mass objects. It also confirms that the stellar masses predicted for the six haloes is typical for haloes of this mass across all environments.

Keeping these restrictions in mind, as a first application, the tuned semi-analytical model has been applied to the entire MS-II merger tree. Figure 6.6 shows the relation of stellar mass-halo mass for all haloes, which the simulations would predict. The top panel shows the stellar mass-halo mass relation for central galaxies, with the black line indicating the median stellar mass at each halo mass. Clearly, the figure includes an unjustified extrapolation to higher masses, but shows the degree of variance that the model would reproduce when applied to the total population. In the bottom panel, the probability distribution of stellar mass is shown, for three different halo masses close to $10^{10} \mathrm{M}_{\odot}$. The scatter increases for lower mass haloes, as is expected when star formation depends so strongly on halo mass. For haloes of $10^{10} \mathrm{M}_{\odot}$, a stellar mass of $\sim 10^{6} \mathrm{M}_{\odot}$, the typical value required to match the measured abundance, is statistically excluded.

6.7 Outlook

A correspondence between the mechanisms of the semi-analytical model and those of the simulations, without degeneracy, would make the properties of the *galaxy population* additional observables of direct, hydrodynamical simulations. Conversely, a semi-analytical model that reproduces the stellar mass function without degeneracies, might provide a direct constraint for the simulations, not only in terms of median, or $z = 0$ properties, but also in terms of the time evolution of individual objects. To put this link on firmer footing for dwarf galaxies will be an obvious next step in my work.

Remarks

My simulations indicate that many of the properties of dwarf galaxies can be reproduced from cosmological initial conditions by known mechanisms. This suggests that, even though the models are still incomplete, they already capture the basic physical processes relevant for dwarf galaxy formation: supernova feedback, UV radiation, and interaction with the environment. However, the goal of science being to *understand*, rather than to *imitate* nature, a close reproduction of the observations is merely a necessary, but not a sufficient condition for success.

Historically, the complementary nature of theory and experiment have been central to scientific research. Their relationship constitutes the *scientific method*, summarised by Peirce in the 19th century, but in practise much longer: new theories can be deduced from observations; predictions induced from existing theories must be tested against new observation and controlled experiments.

Despite numerous achievements, it has been argued (e.g. Wolfram, 2002) that the requirement for both methods to be applicable has defined, and thus perhaps limited, the range of problems that science has been able to address. Clearly, numerical simulations allow us to study phenomena that we otherwise could not: problems which are too complicated or too complex for analytic calculations; systems which are too vast, too small, too rare or otherwise unsuitable to be observed or experimented on. Evidently, the area of galaxy formation contains phenomena that are both difficult (and perhaps impossible) to analyse analytically, as well as difficult to observe, and impossible to reproduce.

Ideally, in this situation, simulations might replace one of the two classical methods. They might be thought of as a convenient extension to theory, a different way of solving analytic equations. Or, they might be seen as controlled, numerical experiments, studying different combinations of parameters, when only a finite number of realisations can be observed in nature. But if they can take *either* role, can they also take *both*? It can be tempting to believe that a successful simulation *proves* a theory, particularly if the predictions agree with actual observations. However, we can rarely observe the mechanism itself, and many observations also rely on models, which entail additional, non-trivial assumptions (examples in my work include the masses of haloes, or the properties of stellar populations). In this case, a comparison constitutes a useful consistency check, but not a direct verification. Furthermore, the inherent complexity of simulations makes it hard to account for all degeneracies. Clearly, we should not be content with any number of agreements, as long as disagreements persist. It would be premature to consider dwarf galaxy formation "solved", when different methods, both making a number of correct predictions, arrive at contradictory conclusions about such fundamental parameters as the stellar mass. We should be prepared not only to refine, but also possibly revise our assumptions in the future. And always prepared to be surprised.

Acknowledgements

There are many people who have contributed to this work in one way or another. And there are some people, who did more than just that, and whose help, guidance, encouragement, support and sometimes critical reflection have been truly important to me. They deserve a special mention.

First of all, I would like to thank my adviser, Simon White, for giving me the opportunity to undertake this project at MPA. Simon is a very busy man, but one who always finds time for his students. His insight and unclouded advice makes this time all the more valuable. Equally, I would like to thank Cecilia Scannapieco, who has been very helpful, especially during my first two years at MPA. I would also like to thank the members of my thesis committee, Andreas Burkert, Martin Faessler and Joachim Rädler at the LMU.

Among the people directly involved in my work, Adrian Jenkins was instrumental in creating the initial conditions for the simulations. Qi Guo introduced me to the concept of abundance matching, and Mike Boylan-Kolchin helped me with my first steps using the Millennium database. Eyal Neistein taught me what I know about semi-analytical models, and throughout our many discussions, he has almost converted me from a sceptic into a believer.

At MPA, I have many colleagues to thank for their inspiration and ideas, through seminars, informal discussions, or regular meetings. Two people in particular must be mentioned here, who always found time in their busy schedules: Guinevere Kauffmann and Volker Springel, whose group meetings were often thought-provoking. Galaxies and questions, large and small, were the topic on Friday afternoons among Guinevere's ever-growing group, which no doubt lead to many collaborations between members, including my own with Qi Guo and Eyal Neistein. In turn, the GADGET meetings lead by Volker often went far beyond computing issues, and often became a place to solve problems "on the back of an envelope". For a long time, Cecilia and I were the only ones to attend both these "Real" and "Fake" galaxies meetings. I believe I benefited greatly.

I have found Munich not only a great place to do work, but also to enjoy life and make new friends. I will not attempt to draw a list, but to those who pick up a copy of my thesis and read this section: you will know who you are. I had the privilege to represent the MPA students for two years, together with Akila – we were a very good team.

There are two people who, although not directly related to my thesis, are still very much in causal contact: I would like to thank Pascale Jablonka for introducing me to the fascinating topic of dwarf galaxies when I was her student in Lausanne. I would also like to thank my physics teacher, Peter Weinhold. It is a safe guess that, had I not met him, I would have ended up on a very different path. Finally, I would like to thank my family, my parents and my sister, for all their love and support during the past three years, and long before that.

Bibliography

Aarseth S. J., 1963, MNRAS, 126, 223

Angus G. W., Famaey B., Tiret O., Combes F., Zhao H. S., 2008, MNRAS, 383, L1

Annibali F., Grutzbauch R., Rampazzo R., Bressan A., Zeilinger W. W., 2010, ArXiv e-prints

Baldry I. K., Glazebrook K., Driver S. P., 2008, MNRAS, 388, 945

Barnes J., Hut P., 1986, Nature, 324, 446

Battaglia G., Tolstoy E., Helmi A., Irwin M. J., Letarte B., Jablonka P., Hill V., Venn K. A., Shetrone M. D., Arimoto N., Primas F., Kaufer A., Francois P., Szeifert T., Abel T., Sadakane K., 2006, A&A, 459, 423

Belokurov V., Walker M. G., Evans N. W., Gilmore G., Irwin M. J., Just D., Koposov S., Mateo M., Olszewski E., Watkins L., Wyrzykowski L., 2010, ArXiv e-prints

Belokurov V. e. a., 2007, ApJ, 654, 897

Benson A. J., Bower R. G., Frenk C. S., Lacey C. G., Baugh C. M., Cole S., 2003, ApJ, 599, 38

Bernard E. J., Monelli M., Gallart C., Drozdovsky I., Stetson P. B., Aparicio A., Cassisi S., Mayer L., Cole A. A., Hidalgo S. L., Skillman E. D., Tolstoy E., 2009, ApJ, 699, 1742

Besla G., Kallivayalil N., Hernquist L., Robertson B., Cox T. J., van der Marel R. P., Alcock C., 2007, ApJ, 668, 949

Blanton M. R., Lupton R. H., Schlegel D. J., Strauss M. A., Brinkmann J., Fukugita M., Loveday J., 2005, ApJ, 631, 208

Blitz L., Robishaw T., 2000, ApJ, 541, 675

Bode P., Ostriker J. P., Turok N., 2001, ApJ, 556, 93

Bolton J., Meiksin A., White M., 2004, MNRAS, 348, L43

Bond J. R., Szalay A. S., 1983, ApJ, 274, 443

Bouchet F. R., 1996, in S. Bonometto, J. R. Primack, & A. Provenzale ed., Dark Matter in the Universe Introductory Overview of Eulerian and Lagrangian Perturbation Theories. pp 565–+

Bouchet F. R., Colombi S., Hivon E., Juszkiewicz R., 1995, A&A, 296, 575

Bower R. G., Benson A. J., Malbon R., Helly J. C., Frenk C. S., Baugh C. M., Cole S., Lacey C. G., 2006, MNRAS, 370, 645

Boylan-Kolchin M., Springel V., White S. D. M., Jenkins A., 2010, MNRAS, 406, 896

Boylan-Kolchin M., Springel V., White S. D. M., Jenkins A., Lemson G., 2009, MNRAS, 398, 1150

Bromm V., Clarke C. J., 2002, ApJ, 566, L1

Bruzual G., Charlot S., 2003, MNRAS, 344, 1000

Burkert A., Ruiz-Lapuente P., 1997, ApJ, 480, 297

Bush S. J., Cox T. J., Hernquist L., Thilker D., Younger J. D., 2008, ApJ, 683, L13

Cantalupo S., 2010, MNRAS, 403, L16

Carignan C., Beaulieu S., 1989, ApJ, 347, 760

Carrasco E. R., Mendes de Oliveira C., Infante L., 2006, AJ, 132, 1796

Castellani M., Marconi G., Buonanno R., 1996, A&A, 310, 715

Chapman S. C., Peñarrubia J., Ibata R., McConnachie A., Martin N., Irwin M., Blain A., Lewis G. F., Letarte B., Lo K., Ludlow A., O'neil K., 2007, ApJ, 662, L79

Christlein D., Gawiser E., Marchesini D., Padilla N., 2009, MNRAS, 400, 429

Ciardi B., Ferrara A., White S. D. M., 2003, MNRAS, 344, L7

Cole A. A., 2010, Publications of the Astronomical Society of Australia, 27, 234

Cole A. A., Skillman E. D., Tolstoy E., Gallagher III J. S., Aparicio A., Dolphin A. E., Gallart C., Hidalgo S. L., Saha A., Stetson P. B., Weisz D. R., 2007, ApJ, 659, L17

Cole S., 1991, ApJ, 367, 45

Cole S., Lacey C. G., Baugh C. M., Frenk C. S., 2000, MNRAS, 319, 168

Colín P., Klypin A., Valenzuela O., Gottlöber S., 2004, ApJ, 612, 50

Colless M., 1999, Royal Society of London Philosophical Transactions Series A, 357, 105

Conroy C., Wechsler R. H., 2009, ApJ, 696, 620

Croton D. J., Springel V., White S. D. M., De Lucia G., Frenk C. S., Gao L., Jenkins A., Kauffmann G., Navarro J. F., Yoshida N., 2006, MNRAS, 365, 11

Dalgarno A., McCray R. A., 1972, ARA&A, 10, 375

Dalla Vecchia C., Schaye J., 2008, MNRAS, 387, 1431

Davis M., Efstathiou G., Frenk C. S., White S. D. M., 1985, ApJ, 292, 371

Davis M., Geller M. J., 1976, ApJ, 208, 13

Davis M., Huchra J., Latham D. W., Tonry J., 1982, ApJ, 253, 423

de Blok W. J. G., McGaugh S. S., Bosma A., Rubin V. C., 2001, ApJ, 552, L23

de Blok W. J. G., Walter F., Brinks E., Trachternach C., Oh S., Kennicutt R. C., 2008, AJ, 136, 2648

De Lucia G., Blaizot J., 2007, MNRAS, 375, 2

de Rijcke S., Penny S. J., Conselice C. J., Valcke S., Held E. V., 2009, MNRAS, 393, 798

Dejonghe H., de Zeeuw T., 1988, ApJ, 333, 90

Dejonghe H., Merritt D., 1992, ApJ, 391, 531

Dekel A., Silk J., 1986, ApJ, 303, 39

Dekel A., Woo J., 2003, MNRAS, 344, 1131

Diemand J., Kuhlen M., Madau P., 2007, ApJ, 667, 859

Dolphin A. E., 2002, MNRAS, 332, 91

Eastwood J. W., Hockney R. W., Lawrence D. N., 1980, Computer Physics Communications, 19, 215

Efstathiou G., 1992, MNRAS, 256, 43P

Einasto J., Saar E., Kaasik A., Chernin A. D., 1974, Nature, 252, 111

Evans N. W., An J., Walker M. G., 2009, MNRAS, 393, L50

Evrard A. E., Summers F. J., Davis M., 1994, ApJ, 422, 11

Faber S. M., Lin D. N. C., 1983, ApJ, 266, L17

Fan X., Narayanan V. K., Strauss M. A., White R. L., Becker R. H., Pentericci L., Rix H., 2002, AJ, 123, 1247

Fellhauer M., Kroupa P., Evans N. W., 2006, MNRAS, 372, 338

Ferrara A., Tolstoy E., 2000, MNRAS, 313, 291

Ferreras I., Silk J., 2001, ApJ, 557, 165

Flynn C., Holmberg J., Portinari L., Fuchs B., Jahreiß H., 2006, MNRAS, 372, 1149

Fraternali F., Tolstoy E., Irwin M. J., Cole A. A., 2009, A&A, 499, 121

Gallart C., Martínez-Delgado D., Gómez-Flechoso M. A., Mateo M., 2001, AJ, 121, 2572

Geha M., Blanton M. R., Masjedi M., West A. A., 2006, ApJ, 653, 240

Geha M., Guhathakurta P., van der Marel R. P., 2002, AJ, 124, 3073

Gilmore G., Wilkinson M. I., Wyse R. F. G., Kleyna J. T., Koch A., Evans N. W., Grebel E. K., 2007, ApJ, 663, 948

Gnedin N. Y., Tassis K., Kravtsov A. V., 2009, ApJ, 697, 55

Gnedin O. Y., Brown W. R., Geller M. J., Kenyon S. J., 2010, ApJ, 720, L108

Governato F., Brook C., Mayer L., Brooks A., Rhee G., Wadsley J., Jonsson P., Willman B., Stinson G., Quinn T., Madau P., 2010, Nature, 463, 203

Governato F., Mayer L., Wadsley J., Gardner J. P., Willman B., Hayashi E., Quinn T., Stadel J., Lake G., 2004, ApJ, 607, 688

Governato F., Willman B., Mayer L., Brooks A., Stinson G., Valenzuela O., Wadsley J., Quinn T., 2007, MNRAS, 374, 1479

Grebel E. K., 1997, in R. E. Schielicke ed., Reviews in Modern Astronomy Vol. 10 of Reviews in Modern Astronomy, Star Formation Histories of Local Group Dwarf Galaxies. (Ludwig Biermann Award Lecture 1996). pp 29–60

Grebel E. K., Gallagher III J. S., 2004, ApJ, 610, L89

Grebel E. K., Gallagher III J. S., Harbeck D., 2003, AJ, 125, 1926

Guo Q., White S., Boylan-Kolchin M., De Lucia G., Kauffmann G., Lemson G., Li C., Springel V., Weinmann S., 2010, ArXiv e-prints

Guo Q., White S., Li C., Boylan-Kolchin M., 2010, MNRAS, 404, 1111

Haardt F., Madau P., 1996, ApJ, 461, 20

Harrison E. R., 1970, Physical Review D, 1, 2726

Hayashi E., Navarro J. F., Power C., Jenkins A., Frenk C. S., White S. D. M., Springel V., Stadel J., Quinn T. R., 2004, MNRAS, 355, 794

Helmi A., Irwin M. J., Tolstoy E., Battaglia G., Hill V., Jablonka P., Venn K., Shetrone M., Letarte B., Arimoto N., Abel T., Francois P., Kaufer A., Primas F., Sadakane K., Szeifert T., 2006, ApJ, 651, L121

Hilker M., Richtler T., 2000, A&A, 362, 895

Hockney R. W., Goel S. P., Eastwood J. W., 1973, Chemical Physics Letters, 21, 589

Hoeft M., Yepes G., Gottlöber S., 2008, in J. Davies & M. Disney ed., IAU Symposium Vol. 244 of IAU Symposium, Too Small to Form a Galaxy: How the UV Background Determines the Baryon Fraction. pp 279–283

Hoeft M., Yepes G., Gottlöber S., Springel V., 2006, MNRAS, 371, 401

Hubble E., 1929, Proceedings of the National Academy of Science, 15, 168

Hubble E. P., 1926, ApJ, 64, 321

Hunter D. A., Elmegreen B. G., 2006, ApJS, 162, 49

Jenkins A., 2010, MNRAS, pp 172–+

Johnston K. V., Zhao H., Spergel D. N., Hernquist L., 1999, ApJ, 512, L109

Katz N., 1992, ApJ, 391, 502

Katz N., Weinberg D. H., Hernquist L., 1996, ApJS, 105, 19

Katz N., White S. D. M., 1993, ApJ, 412, 455

Kauffmann G., White S. D. M., Guiderdoni B., 1993, MNRAS, 264, 201

Kauffmann G. e. a., 2003, MNRAS, 341, 33

Kennicutt Jr. R. C., 1989, ApJ, 344, 685

Kennicutt Jr. R. C., 1998, ApJ, 498, 541

Khochfar S., Silk J., Windhorst R. A., Ryan Jr. R. E., 2007, ApJ, 668, L115

Kitayama T., Tajiri Y., Umemura M., Susa H., Ikeuchi S., 2000, MNRAS, 315, L1

Klimentowski J., Łokas E. L., Kazantzidis S., Mayer L., Mamon G. A., 2009, MNRAS, 397, 2015

Klypin A., Kravtsov A. V., Valenzuela O., Prada F., 1999, ApJ, 522, 82

Koch A., Grebel E. K., Gilmore G. F., Wyse R. F. G., Kleyna J. T., Harbeck D. R., Wilkinson M. I., Wyn Evans N., 2008, AJ, 135, 1580

Koch A., Grebel E. K., Wyse R. F. G., Kleyna J. T., Wilkinson M. I., Harbeck D. R., Gilmore G. F., Evans N. W., 2006a, AJ, 131, 895

Koch A., Grebel E. K., Wyse R. F. G., Kleyna J. T., Wilkinson M. I., Harbeck D. R., Gilmore G. F., Evans N. W., 2006b, AJ, 131, 895

Koch A., Kleyna J. T., Wilkinson M. I., Grebel E. K., Gilmore G. F., Evans N. W., Wyse R. F. G., Harbeck D. R., 2007, AJ, 134, 566

Koleva M., de Rijcke S., Prugniel P., Zeilinger W. W., Michielsen D., 2009, MNRAS, 396, 2133

Komatsu E., Dunkley J., Nolta M. R., Bennett C. L., Gold B., Hinshaw G., Jarosik N., Larson D., Limon M., Page L., Spergel D. N., Halpern M., Hill R. S., Kogut A., Meyer S. S., Tucker G. S., Weiland J. L., Wollack E., Wright E. L., 2009, ApJS, 180, 330

Komatsu E. e. a., 2010, ArXiv e-prints

Koposov S., Belokurov V., Evans N. W., Hewett P. C., Irwin M. J., Gilmore G., Zucker D. B., Rix H., Fellhauer M., Bell E. F., Glushkova E. V., 2008, ApJ, 686, 279

Kormendy J., 1985, ApJ, 295, 73

Kormendy J., Fisher D. B., Cornell M. E., Bender R., 2009, ApJS, 182, 216

Koyama H., Ostriker E. C., 2009, ApJ, 693, 1316

Larson R. B., 1974, MNRAS, 169, 229

Lavery R. J., Mighell K. J., 1992, AJ, 103, 81

Lewis G. F., Ibata R. A., Chapman S. C., McConnachie A., Irwin M. J., Tolstoy E., Tanvir N. R., 2007, MNRAS, 375, 1364

Li C., White S. D. M., 2009, MNRAS, 398, 2177

Li Y., Helmi A., 2008, MNRAS, 385, 1365

Łokas E. L., 2002, MNRAS, 333, 697

Maio U., Dolag K., Ciardi B., Tornatore L., 2007, MNRAS, 379, 963

Mandelbaum R., Seljak U., Kauffmann G., Hirata C. M., Brinkmann J., 2006, MNRAS, 368, 715

Marlowe A. T., Heckman T. M., Wyse R. F. G., Schommer R., 1995, ApJ, 438, 563

Marri S., White S. D. M., 2003, MNRAS, 345, 561

Martin N. F., Ibata R. A., Irwin M. J., Chapman S., Lewis G. F., Ferguson A. M. N., Tanvir N., McConnachie A. W., 2006, MNRAS, 371, 1983

Mashchenko S., Wadsley J., Couchman H. M. P., 2008, Science, 319, 174

Mateo M., Olszewski E. W., Walker M. G., 2008, ApJ, 675, 201

Mateo M. L., 1998, ARA&A, 36, 435

Matteucci F., Recchi S., 2001, ApJ, 558, 351

Mayer L., Governato F., Colpi M., Moore B., Quinn T., Wadsley J., Stadel J., Lake G., 2001, ApJ, 547, L123

Mayer L., Mastropietro C., Wadsley J., Stadel J., Moore B., 2006, MNRAS, 369, 1021

McConnachie A. W., Arimoto N., Irwin M., Tolstoy E., 2006, MNRAS, 373, 715

McQuinn K. B. W., Skillman E. D., Cannon J. M., Dalcanton J. J., Dolphin A., Stark D., Weisz D., 2009, ApJ, 695, 561

Michielsen D., Boselli A., Conselice C. J., Toloba E., Whiley I. M., Aragón-Salamanca A., Balcells M., Cardiel N., Cenarro A. J., Gorgas J., Peletier R. F., Vazdekis A., 2008, MNRAS, 385, 1374

Misgeld I., Mieske S., Hilker M., 2008, A&A, 486, 697

Mo H., Van den Bosch F., White S. D. M., 2010, Galaxy formation and evolution. Cambridge University Press

Monaghan J. J., 1992, ARA&A, 30, 543

Monaghan J. J., 2001, Journal of Korean Astronomical Society, 34, 203

Monaghan J. J., Lattanzio J. C., 1985, A&A, 149, 135

Monelli M., Hidalgo S. L., Stetson P. B., Aparicio A., Gallart C., Dolphin A. E., Cole A. A., Weisz D. R., Skillman E. D., Bernard E. J., Mayer L., Navarro J. F., Cassisi S., Drozdovsky I., Tolstoy E., 2010, ApJ, 720, 1225

Moore B., 1994, Nature, 370, 629

Moore B., Ghigna S., Governato F., Lake G., Quinn T., Stadel J., Tozzi P., 1999, ApJ, 524, L19

Moore B., Governato F., Quinn T., Stadel J., Lake G., 1998, ApJ, 499, L5+

Moster B. P., Somerville R. S., Maulbetsch C., van den Bosch F. C., Macciò A. V., Naab T., Oser L., 2010, ApJ, 710, 903

Moutarde F., Alimi J., Bouchet F. R., Pellat R., Ramani A., 1991, ApJ, 382, 377

Murali C., 2000, ApJ, 529, L81

Nagai D., Kravtsov A. V., 2005, ApJ, 618, 557

Navarro J. F., Eke V. R., Frenk C. S., 1996, MNRAS, 283, L72

Navarro J. F., Frenk C. S., White S. D. M., 1996, ApJ, 462, 563

Navarro J. F., Steinmetz M., 2000, ApJ, 538, 477

Navarro J. F., White S. D. M., 1994, MNRAS, 267, 401

Neistein E., Weinmann S. M., 2010, MNRAS, 405, 2717

Okamoto T., Frenk C. S., 2009, MNRAS, 399, L174

Okamoto T., Frenk C. S., Jenkins A., Theuns T., 2010, MNRAS, 406, 208

Orban C., Gnedin O. Y., Weisz D. R., Skillman E. D., Dolphin A. E., Holtzman J. A., 2008, ApJ, 686, 1030

Padmanabhan N. e. a., 2007, MNRAS, 378, 852

Padmanabhan T., 2006, An Invitation to Astrophysics. World Scientific Publishing Company

Peñarrubia J., Benson A. J., Walker M. G., Gilmore G., McConnachie A. W., Mayer L., 2010, MNRAS, 406, 1290

Peebles P. J. E., 1980, The Large-Scale Structure of the Universe. Princeton Univ. Press, Princeton, NJ

Pelupessy F. I., van der Werf P. P., Icke V., 2004, A&A, 422, 55

Percival W. J. e. a., 2001, MNRAS, 327, 1297

Perlmutter S., The Supernova Cosmology Project 1999, ApJ, 517, 565

Piatek S., Pryor C., Olszewski E. W., 2008, AJ, 135, 1024

Power C., Navarro J. F., Jenkins A., Frenk C. S., White S. D. M., Springel V., Stadel J., Quinn T., 2003, MNRAS, 338, 14

Quirk W. J., 1972, ApJ, 176, L9+

Read J. I., Gilmore G., 2005, MNRAS, 356, 107

Read J. I., Pontzen A. P., Viel M., 2006, MNRAS, 371, 885

Revaz Y., Jablonka P., Sawala T., Hill V., Letarte B., Irwin M., Battaglia G., Helmi A., Shetrone M. D., Tolstoy E., Venn K. A., 2009, A&A, 501, 189

Ricotti M., Gnedin N. Y., Shull J. M., 2002, ApJ, 575, 49

Ryden B., 2002, Introduction to Cosmology. Benjamin Cummings

Sahni V., Coles P., 1995, Physics Reports, 262, 1

Salpeter E. E., 1955, ApJ, 121, 161

Sánchez-Janssen R., Méndez-Abreu J., Aguerri J. A. L., 2010, MNRAS, 406, L65

Saro A., De Lucia G., Borgani S., Dolag K., 2010, MNRAS, 406, 729

Sawala T., Guo Q., Scannapieco C., Jenkins A., White S. D. M., 2010, ArXiv e-prints

Sawala T., Scannapieco C., Maio U., White S., 2010, MNRAS, pp 3–+

Scannapieco C., Tissera P. B., White S. D. M., Springel V., 2005, MNRAS, 364, 552

Scannapieco C., Tissera P. B., White S. D. M., Springel V., 2006, MNRAS, 371, 1125

Scannapieco C., Tissera P. B., White S. D. M., Springel V., 2008, MNRAS, 389, 1137

Scannapieco C., White S. D. M., Springel V., Tissera P. B., 2009, MNRAS, 396, 696

Searle L., Zinn R., 1978, ApJ, 225, 357

Shetrone M., Venn K. A., Tolstoy E., Primas F., Hill V., Kaufer A., 2003, AJ, 125, 684

Silk J., 1985, ApJ, 297, 1

Simon J. D., Geha M., 2007, ApJ, 670, 313

Skillman E. D., Tolstoy E., Cole A. A., Dolphin A. E., Saha A., Gallagher J. S., Dohm-Palmer R. C., Mateo M., 2003, ApJ, 596, 253

Smith M. C. e. a., 2007, MNRAS, 379, 755

Smoot G. F. e. a., 1992, ApJ, 396, L1

Somerville R. S., 2002, ApJ, 572, L23

Springel V., 2005, MNRAS, 364, 1105

Springel V., Hernquist L., 2003, MNRAS, 339, 289

Springel V., Wang J., Vogelsberger M., Ludlow A., Jenkins A., Helmi A., Navarro J. F., Frenk C. S., White S. D. M., 2008, MNRAS, 391, 1685

Springel V., White S. D. M., Jenkins A., Frenk C. S., Yoshida N., Gao L., Navarro J., Thacker R., Croton D., Helly J., Peacock J. A., Cole S., Thomas P., Couchman H., Evrard A., Colberg J., Pearce F., 2005, Nature, 435, 629

Springel V., Yoshida N., White S. D. M., 2001, New Astronomy, 6, 79

Staveley-Smith L., Davies R. D., Kinman T. D., 1992, MNRAS, 258, 334

Stinson G. S., Dalcanton J. J., Quinn T., Gogarten S. M., Kaufmann T., Wadsley J., 2009, MNRAS, 395, 1455

Stinson G. S., Dalcanton J. J., Quinn T., Kaufmann T., Wadsley J., 2007, ApJ, 667, 170

Strigari L. E., Bullock J. S., Kaplinghat M., Simon J. D., Geha M., Willman B., Walker M. G., 2008, Nature, 454, 1096

Susa H., Umemura M., 2004, ApJ, 600, 1

Sutherland R. S., Dopita M. A., 1993, ApJS, 88, 253

Tafelmeyer M., Jablonka P., Hill V., Shetrone M., Tolstoy E., Irwin M. J., Battaglia G., Helmi A., Starkenburg E., Venn K. A., Abel T., Francois P., Kaufer A., North P., Primas F., Szeifert T., 2010, A&A, 524, A58+

Tajiri Y., Umemura M., 1998, ApJ, 502, 59

Tegmark M., 1996, ApJ, 464, L35+

Thacker R. J., Couchman H. M. P., 2000, ApJ, 545, 728

Thielemann F. K., 1993, Origin and Evolution of the Elements. Cambridge Univ. Press, Cambridge, UK, p. 299

Tissera P. B., White S. D. M., Pedrosa S., Scannapieco C., 2010, MNRAS, 406, 922

Tollerud E. J., Bullock J. S., Strigari L. E., Willman B., 2008, ApJ, 688, 277

Tolstoy E., Hill V., Tosi M., 2009, ARA&A, 47, 371

Tolstoy E., Venn K. A., Shetrone M., Primas F., Hill V., Kaufer A., Szeifert T., 2003, AJ, 125, 707

Tormen G., 1996, in R. Ansari, Y. Giraud-Heraud, & J. Tran Thanh Van ed., Dark Matter in Cosmology Quantam Measurements Experimental Gravitation Hydrodynamic Simulations of Galaxy Formation. pp 207–+

Tremaine S. D., 1976, ApJ, 203, 72

Trentham N., Sampson L., Banerji M., 2005, MNRAS, 357, 783

Valcke S., de Rijcke S., Dejonghe H., 2008, MNRAS, 389, 1111

Vale A., Ostriker J. P., 2006, MNRAS, 371, 1173

Van Daalen M. e. a., 2011, In preparation

van den Bergh S., 1994, ApJ, 428, 617

van den Bosch F. C., Swaters R. A., 2001, MNRAS, 325, 1017

Viel M., Becker G. D., Bolton J. S., Haehnelt M. G., Rauch M., Sargent W. L. W., 2008, Physical Review Letters, 100, 041304

Wadepuhl M., Springel V., 2010, MNRAS, pp 1538–+

Walker M. G., Mateo M., Olszewski E. W., 2009, AJ, 137, 3100

Walker M. G., Mateo M., Olszewski E. W., Gnedin O. Y., Wang X., Sen B., Woodroofe M., 2007, ApJ, 667, L53

Weinberg S., 2008, Cosmology. Oxford University Press, USA

Wetzstein M., Naab T., Burkert A., 2007, MNRAS, 375, 805

White S. D. M., 1994, ArXiv Astrophysics e-prints

White S. D. M., Frenk C. S., 1991, ApJ, 379, 52

White S. D. M., Rees M. J., 1978, MNRAS, 183, 341

Whiting A. B., Hau G. K. T., Irwin M., 1999, AJ, 118, 2767

Willman B., Dalcanton J. J., Martinez-Delgado D., West A. A., Blanton M. R., Hogg D. W., Barentine J. C., Brewington H. J., Harvanek M., Kleinman S. J., Krzesinski J., Long D., Neilsen Jr. E. H., Nitta A., Snedden S. A., 2005, ApJ, 626, L85

Wise J. H., Abel T., 2008, ApJ, 684, 1

Wolfram S., 2002, A New Kind of Science. Wolfram Media

Woo J., Courteau S., Dekel A., 2008, MNRAS, 390, 1453

Woosley S. E., Weaver T. A., 1995, ApJS, 101, 181

Xue X. X., Rix H. W., Zhao G., Re Fiorentin P., Naab T., Steinmetz M., van den Bosch F. C., Beers T. C., Lee Y. S., Bell E. F., Rockosi C., Yanny B., Newberg H., Wilhelm R., Kang X., Smith M. C., Schneider D. P., 2008, ApJ, 684, 1143

Yang X., Mo H. J., van den Bosch F. C., 2003, MNRAS, 339, 1057

Zaritsky D., Gonzalez A. H., Zabludoff A. I., 2006, ApJ, 642, L37

Zavala J., Jing Y. P., Faltenbacher A., Yepes G., Hoffman Y., Gottlöber S., Catinella B., 2009, ApJ, 700, 1779

Zel'Dovich Y. B., 1970, A&A, 5, 84

Zeldovich Y. B., 1972, MNRAS, 160, 1P